

**On-surface synthesis of two-dimensional  
graphene nanoribbon networks**

XU ZHEN

2020



## *Contents*

Chapter 1.....	1
General Introduction.....	1
1-1. Graphene and graphene nanoribbons (GNRs).....	1
1-2. Fabrication approaches of GNRs.....	6
1-3. Two-dimensional (2D) graphene nanoribbon networks (GNNs).....	13
1-4. Thermoelectric (TE) application of GNRs.....	17
1-5. Motivation and objectives.....	24
1-6. References.....	24
Chapter 2.....	33
Experimental.....	33
2-1. General information.....	33
2-1-1. Materials.....	33
2-1-2. Methods.....	33
2-1-3. Au(111) substrates.....	33
2-1-4. Two-zone chemical vapor deposition (2Z-CVD).....	34
2-2. Characterization techniques of 1D GNRs and 2D GNNs.....	34
2-2-1. Scanning tunneling microscopy (STM) measurements.....	34
2-2-2. Raman spectra.....	35
2-2-3. Scanning electron microscopy (SEM).....	35
2-2-4. Atomic force microscopy (AFM).....	35
2-3. Sample preparation and characterization of 2D GNNs properties.....	35
2-3-1. Preparation of hydrophobic quartz and surface oxidized silicon (SiO <sub>2</sub> /Si) substrates.....	35
2-3-2. GNN transfer process.....	36
2-3-3. In-plane electrical conductivity measurements.....	36

2-3-4. Cross-plane electrical conductance measurements.....	37
2-3-5. FET device fabrication and measurements.....	38
2-3-6. Thermal conductivity measurements.....	38
2-4. Calculations.....	40
2-5. Synthetic procedures.....	41
2-5-1. Synthesis of ‘Z-bar-linkage’ precursors with different branch length.....	41
2-5-2. Synthesis of precursors for armchair GNRs.....	48
2-6. References.....	50
 Chapter 3.....	 52
On-surface synthesis of graphene clusters from a Z-bar-linkage precursor with quaterphenyl branches.....	52
3-1. Introduction.....	52
3-2. Results and discussion.....	53
3-2-1. Structural studies on the products of 2Z-CVD.....	53
3-2-2. Adsorption conformations of the precursor.....	57
3-3. Conclusions.....	60
3-4. Reference.....	61
 Chapter 4.....	 64
Bottom-up on-surface synthesis of two-dimensional graphene nanoribbon networks and their thermoelectric properties.....	64
4-1. Introduction.....	64
4-2. Results and discussion.....	66
4-2-1. Fabrication of 1D GNRs and 2D GNNs.....	66
4-2-2. Thermoelectric properties of fabricated 1D GNR and 2D GNN.....	74
4-3. Conclusions.....	82
4-4. References.....	83



Chapter 5.....	86
General Conclusion.....	86
List of publications .....	89
Other publications .....	89
List of presentations.....	91
Acknowledgement .....	93



## Chapter 1

### General Introduction

#### 1-1. Graphene and graphene nanoribbons (GNRs)

Graphene is monolayer carbon atoms which are packed into 2D hexagonal honeycomb lattice with  $sp^2$  hybridization and delocalized  $\pi$  bonds. Figure 1-1 shows the honeycomb lattice of graphene.<sup>1</sup> Each unit cell contains two different carbon atoms (A and B). Graphene has been extensively studied because of its theoretically predicted intriguing mechanical and physicochemical properties, such as high specific surface area (SSA),<sup>2,3</sup> excellent mechanical and fracture strength,<sup>4,5</sup> incomparable thermal<sup>6</sup> and electrical conductivity,<sup>7,8</sup> high pliability, unparalleled impermeability,<sup>9</sup> peculiar electronic properties (for instance, quantum Hall effect),<sup>10,11</sup> and tolerance of extremely high density electric current,<sup>12</sup> since its being isolated firstly by Geim and Novoselov in 2004.<sup>13</sup> However, it suffers from the zero band gap restricting its applications in digital electronics, one of the most significant application field. As shown in Figure 1-2, the conduction band and the valence band cross at the Dirac point (K and K'), which indicates the zero band gap in the intrinsic graphene.<sup>1</sup> Various strategies have been developed to open up the band gap without significantly compromising its superior carrier mobility in graphene, such as atomic doping<sup>14,15</sup> (like hydrogenation<sup>16-18</sup>), molecular functionalization,<sup>19,20</sup> and conversion of graphene into different nanostructures (including bilayer graphene,<sup>21,22</sup> graphene nanoribbons (GNRs),<sup>23-30</sup> and graphene nanomeshes,<sup>31-33</sup> etc.). For atomic doping and molecular functionalization, some disorders may inevitably be produced, which could sacrifice its charge carriers mobility. Also, considering the electronic miniaturization tendency and integration, GNRs show more application prospect compared with bilayered or nanomeshed graphene.

GNRs as subset of graphene are of especial interest, Since GNRs are endowed with band gap based on the quantum confinement. Theoretical calculations showed that for GNRs of several nanometers, the band gap varies as a function of width  $W$  ( $\Delta E(W) \sim 1 \text{ eV} \cdot \text{nm} W^{-1}$ ).<sup>34-36</sup> Thus, a width of less than 10 nm is necessary in order to attain a band gap of more than 0.1 eV. The quantum confinement is only dependent on the geometric structures, namely the width and edge structures.<sup>36</sup> Additionally, combined with high carrier mobility and current carrying capability in graphene, GNRs attracted lots of interest as graphene nanoelectronics.

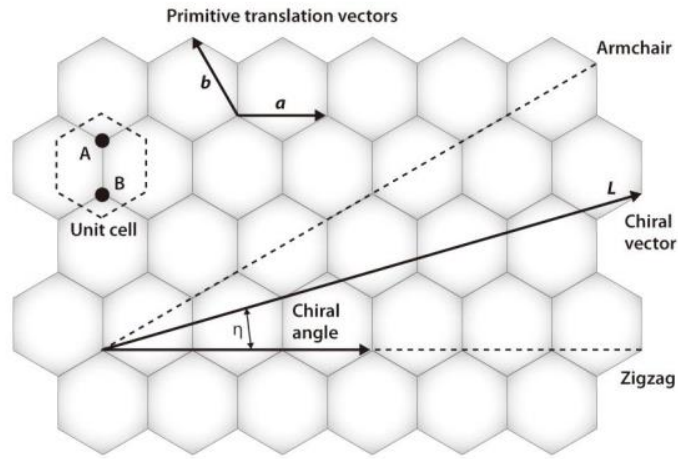


**Figure 1-1.** The honeycomb lattice model of graphene. Two carbon atoms (A and B) contained in the hexagonal unit cell.  $\eta$  denotes the chiral angle, with  $\eta = 0$  corresponding to zigzag edges and  $\eta = \pi/6$  to armchair edges.<sup>1</sup> (Ref. [1], Copyright 2009, Nature Publishing Group.)

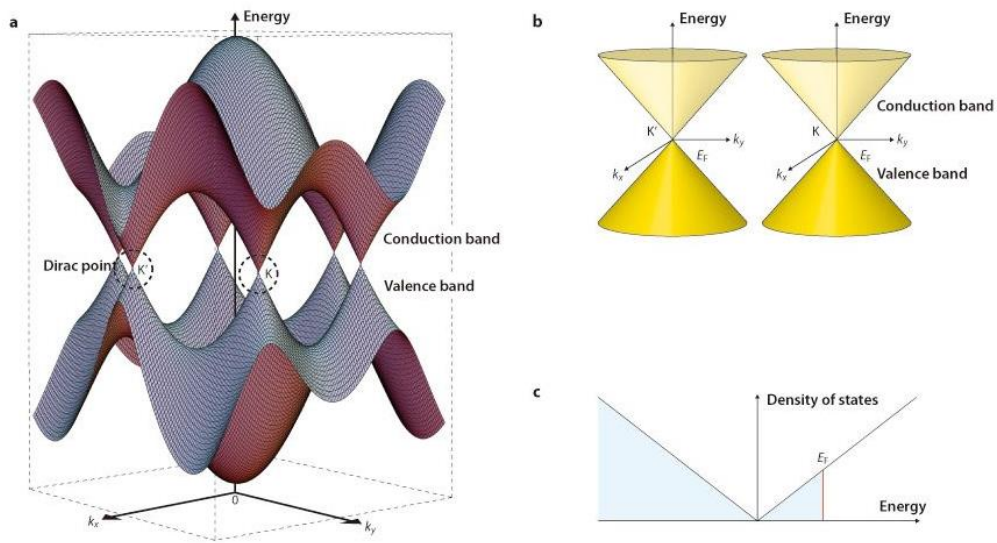


**Figure 1-2.** Energy band in graphene.<sup>1</sup> (a) band structure near the Fermi level (conduction and valence bands cross at Dirac points K and K'). (b) Conic energy bands near the K and K' points. (c) Density of states near the Fermi level (Fermi energy  $E_F$ ). (Ref. [1], Copyright 2009, Nature Publishing Group.)

Extensive theoretical investigations have been conducted for GNRs with various structures, among which zigzag and armchair oriented ones were most studied.<sup>37-45</sup> Taking zigzag and armchair edged GNRs for example, aligning the chiral vector  $\eta = 0$  corresponds to the zigzag

edged GNRs (ZGNRs) and the chiral vector  $\eta = \pi/6$  or  $\pi/2$  corresponds to the armchair edged GNRs (AGNRs) (Figure 1-1). Theoretical calculations showed large difference in the formation energy of GNRs with different edge topology.<sup>40</sup>

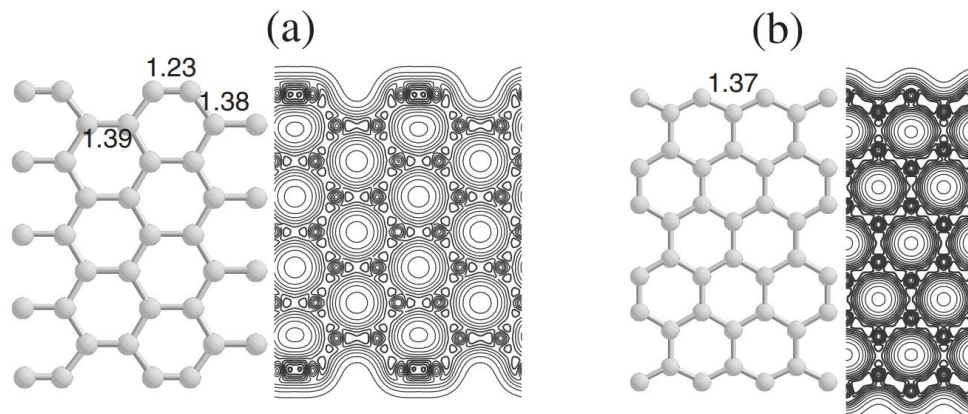


**Figure 1-3.** Optimized geometries and contour plots of total valence electrons of clean (a) armchair and (b) zigzag edged GNRs. The difference between each neighbor contour is 0.045 a.u.<sup>40</sup> (Ref. [37], Copyright 2008, American Physical Society.)

As shown in Figure 1-3 (a), lattice relaxation and strong pairing of  $sp$  hybridization on the armchair edge lead to the edge C–C bond of shorter length (1.23 Å) and higher charge density, respectively, indication of the stability and small formation energy of armchair edge.<sup>40</sup> However, there is no lattice relaxation of edge atoms for zigzag edge (Figure 1-3 (b)), and the edge C–C bond length is same as that of those atoms with threefold coordinations.<sup>40</sup> Additionally, theoretical calculations showed that ZGNRs of the ground state (including spin degree of freedom) have a band gap inversely proportional to their widths and the energy splitting at  $ka = \pi$  is ca. 0.52 eV regardless of its width when  $n \geq 8$  (Figure 1-4 (a)-(c)).<sup>44,45</sup> As for electronic properties of ZGNRs, the two edges favor opposite spin (antiferromagnetic) electronic configuration at ground state, where ferromagnetically ordered edge states occur at each edge.<sup>46-48</sup> Thus, when applying the transverse electric fields (Figure 1-4 (d)), the conduction and valence edge-state bands close their gap with one spin orientation (half-metallic behavior), however, widening their gap with the other spin orientation (insulating behavior).<sup>45</sup> The above phenomenon comes from the energy level shifts of the opposite signs (spatially separated spin ordered edge states) induced by the electric field (Figure 1-4 (e)).<sup>45</sup>

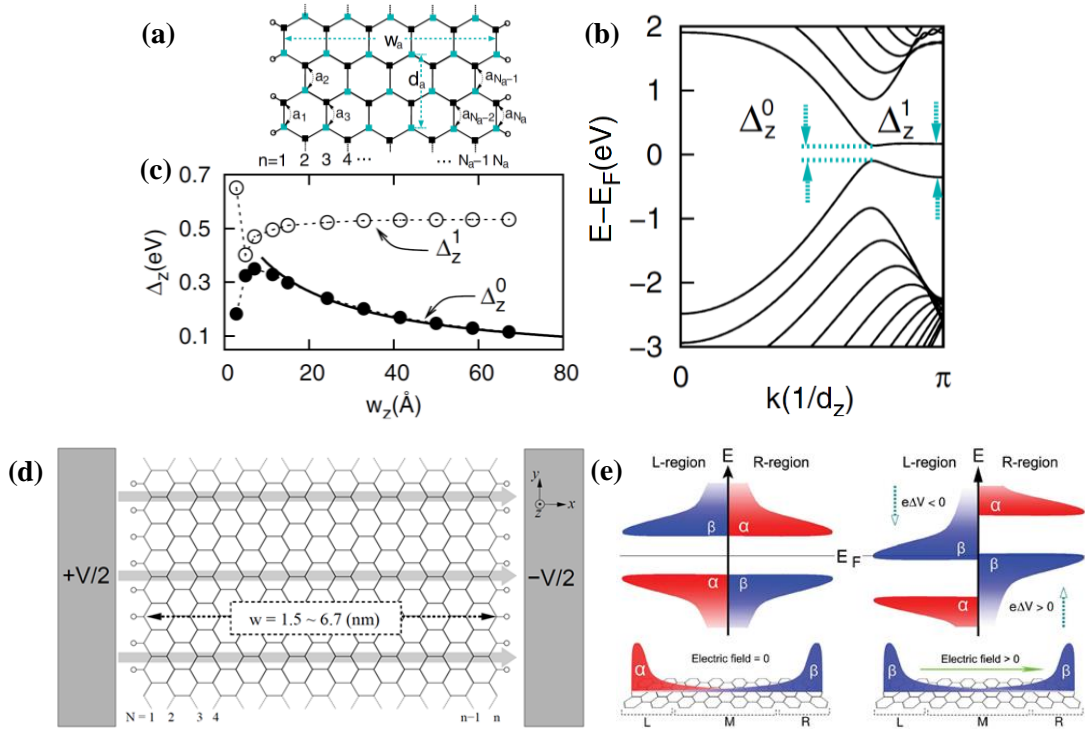


**Figure 1-4.** Electronic properties of ZGNR.<sup>44,45</sup> (a) Schematic representation of ZGNR and the definition of its width. (b) The band structure of 12-ZGNR.  $\Delta_z^0$  and  $\Delta_z^1$  denote the direct band gap and the energy splitting at  $kd_z = \pi$ , respectively. (c)  $\Delta_z^0$  and  $\Delta_z^1$  as a function of the width ( $w_z$ ) of  $N_z$ -ZGNR. (Ref. [44], Copyright 2006, American Physical Society.) (d) the electric field is applied across the ZGNR along the lateral direction with assumed infinite extension in the length; the terminal hydrogen atoms are represented by circles. (e) left: density of states for ZGNR without electric field; right: when applying the electric fields, the energies of localized edge states on both edges are shifted leading to the only one spin orientation left. (Ref. [45], Copyright 2006, Nature Publishing Group.)

As for the AGNRs, theoretical predictions of their electronic properties were conducted by both DFT and GW methods (Figure 1-5).<sup>44,49</sup> From Figure 1-5, the AGNRs showed various band gaps as a function of their widths indicating their semiconducting properties. Specifically, the band gaps decrease with the increase of the width. The theoretical predicted results based on different calculation methods showed certain differences. In Figure 1-5, DFT calculations underestimate the band gaps, and GW approximation is applied to correct the DFT calculations in order to obtain more reliable results.<sup>50</sup> According to the relationship of width and band gaps, AGNRs can be classified into three subfamilies as  $Na = 3p, 3p+1, 3p+2$  ( $p$  is an integer,  $Na$

denotes the number of dimer lines across the AGNRs width). With the same width, AGNRs of  $N_a = 3p+1$  have the largest energetic band gaps, while those of  $N_a = 3p+2$  have the smallest band gaps.

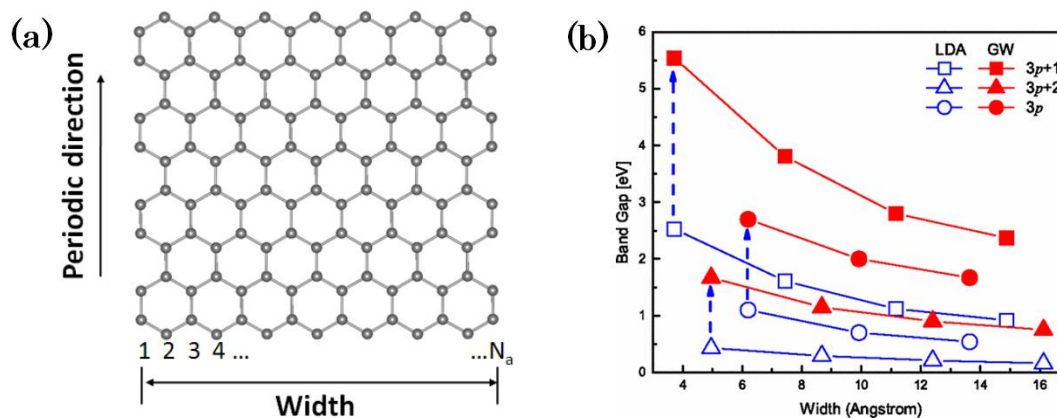


**Figure 1-5.** AGNR structure and width dependent band gaps. (a) schematic representation of AGNR and the definition of its width; (b) width dependent band gaps of AGNRs based on LDA and GW calculations. Dashed arrows denote the self-energy corrections for the narrowest AGNRs within each subfamilies.<sup>49</sup> (Ref. [49], Copyright 2007, American Physical Society.)

Recent research also showed the evolution of GNRs orbitals as well as the band gaps of 5-AGNRs as a function of length.<sup>51</sup> Chi *et al.*<sup>52</sup> and Liljeroth *et al.*<sup>51</sup> fabricated the 5-AGNRs on Au(111) (Figure 1-6 (a)), which could be assigned to  $3p+2$  subfamily and considered as narrowest armchair GNR. The study via low-temperature scanning tunnelling microscopy revealed that both the GNRs orbitals and band gaps vary as the increase of GNRs length and gradually saturate to certain values (Figure 1-6 (b), (c)). The HOMO-LUMO gap decreased initially fast as the increase of GNRs length, which is below 0.2 eV for length of ca. 4 nm (corresponding to pentamer ribbons). The saturated value turned out to be  $0.10 \pm 0.02$  eV. DFT calculations showed slightly overestimation of the HOMO-LUMO gaps due to the experimental charging of the ribbons and the strong Au(111) screening effect.

As stated above, tailoring the graphene into GNRs is capable of opening the band gaps definitely due to the quantum confinement effect. However, the GNRs electronic properties strongly depend on their chemical structures, mainly involved in the width,<sup>44,49,53-55</sup> edge structure<sup>40,56-59</sup> and length.<sup>51</sup> Therefore, with respect to various requirements, the rational structural

design and fabrication techniques would be of great challenge.

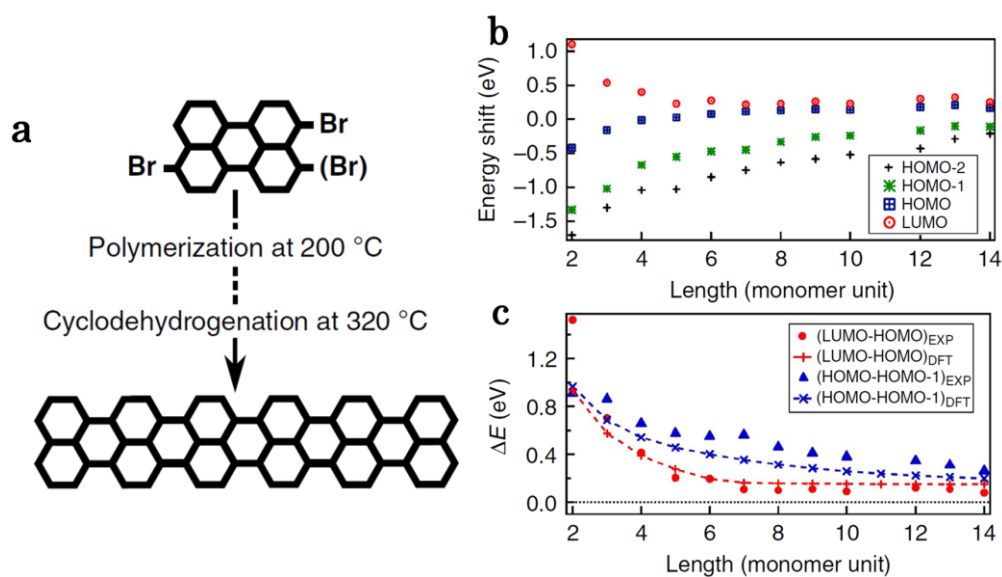


**Figure 1-6.** Fabrication process of 5A-GNRs and energy of molecular orbitals. (a) on-surface synthesis of 5-AGNRs; (b) molecular orbitals and (c) band gaps of 5-AGNRs as a function of ribbons length.<sup>51</sup> (Ref. [51], Copyright 2015, Nature Publishing Group.)

## 1-2. Fabrication approaches of GNRs

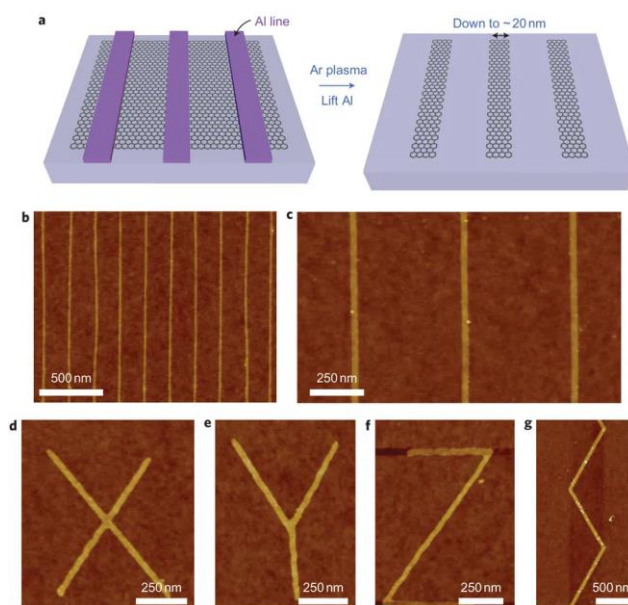


**Figure 1-7.** EBL patterned GNR arrays and junctions. a, Schematic representation of the fabrication process. b-c, AFM images of GNR arrays; d-g, AFM images of various GNR geometries.<sup>60</sup> (Ref. [62], Copyright 2010, Nature Publishing Group.)



In order to fabricate GNRs, two main strategies, that is “top-down” and “bottom-up” approaches, were developed. Top-down approaches usually refer to “cutting” or “scissoring” graphene (lithographic patterning) and unzipping carbon nanotubes (CNTs) into graphene nano strips. To begin with, for lithographic patterning, the graphene is prepared by certain techniques, such as exfoliation, chemical vapor deposition and epitaxial growth on SiC and so on. Afterwards, the graphene should be masked by resists,<sup>61,62</sup> metals<sup>60</sup> or nanowires<sup>63</sup> as ribbons pattern so that the exposed areas can be etched away leaving the ribbons structures beneath the masks. As for the “cutting” or “scissoring” tools, diverse techniques were explored, including e-beam lithography,<sup>61,62,64</sup> dip-pen lithography,<sup>65</sup> gas plasma etching,<sup>63,66</sup> catalytic particles cutting,<sup>67-69</sup> etc.

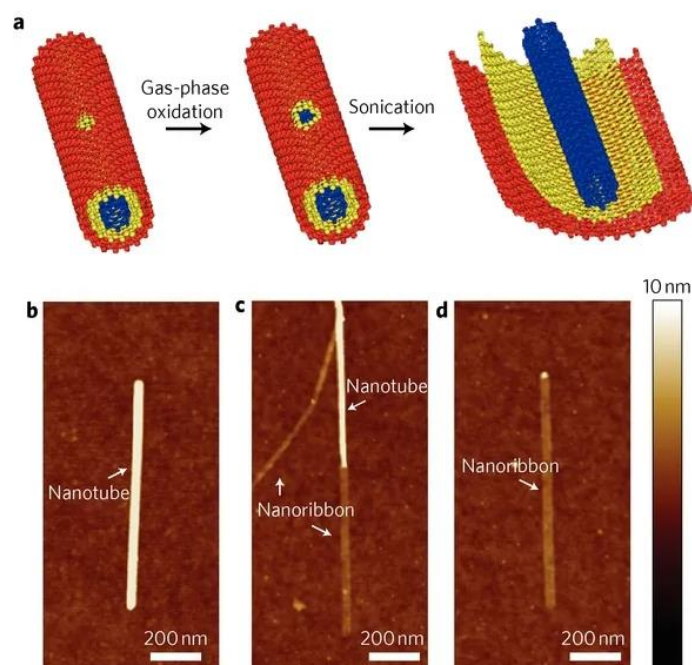


**Figure 1-8.** Unzipping of MWCNTs to GNRs. a, Schematic of the unzipping process. b–d, AFM images of pristine, partially and fully unzipped MWCNTs, respectively.<sup>70</sup> (Ref. [70], Copyright 2010, Nature Publishing Group.)

Taking the graphene etching for example (Figure 1-7 (a)), Dai *et al.*<sup>60</sup> utilized poly(methylmethacrylate) (PMMA) as the positive-tone resist of e-beam lithography (EBL) and single pixel lines were exposed via charge dosage on the PMMA layer. After wards, resist development was carried out in 1:3 methyl iso-butyl ketone:isopropanol solution at 4 °C. As a

result, 20 nm trenches were formed, followed by the coating of aluminium film via e-beam evaporation. Ar plasma was utilized to etch the exposed area of graphene without the protection of Al mask. Finally, Al mask was removed by soaking in 0.1 M KOH aqueous solution. The GNRs of width ~20 nm beneath the Al mask were achieved (Figure 1-7 (b)-(c)). By means of this approach, GNRs of various geometries were also able to be produced (Figure 1-7 (d)-(g)). However, the drawbacks of this approach are that the GNRs width is restricted by the proximity effect in EBL and lack of atomically precise.

**Table 1-1.** Summary of fabrication methods of GNRs and respective electric properties (adapted from Ref.[74, 75]<sup>71,72</sup>)

Methods	GNR width (nm)	$I_{ON}/I_{OFF}$	Mobility ( $\text{cm}^2 \text{V}^{-1} \text{s}^{-1}$ )	Conductivity	Ref.
Lithographic <sup>61</sup>	~ 20	~ $10^3$ (1.7 K)	54 (back gate)	~ 10 $\mu\text{S}$ (1.6 K, 24 nm)	60
Chemical <sup>69</sup>	~ 10				69
Sonochemical <sup>73</sup>	< 10	~ $10^7$ (300 K)	~ 200 (back gate)	~ 4 $\mu\text{S}$ (300 K, < 10 nm)	75
Unzipping of CNTs <sup>74</sup>	< 10	~ $10^3$ (50 K)	~ 1600 (back gate)	~ 0.97 mS (300 K, 10~20 nm)	76
SiC-step template <sup>75</sup>	$\leq$ 40	10 (RT); > 25 (4 K)	900~2700	1~5.5 mS (300 K, 40 nm)	77
Edge-narrowing <sup>60</sup>	sub-5	$10^4$ (RT)			62
Ni-assisted growth <sup>71</sup>	~ 23	~ $10^4$ (11 K)	~ 40 (back gate)	~ 30 $\mu\text{S}$ (11 K, 30 nm)	74
ALD-on edge <sup>76</sup>	15	~4	~400 (15 nm)		79

Another representative approach for top-down fabrication of GNRs is the unzipping

CNTs.<sup>70,77-79</sup> Dai *et al.*<sup>70</sup> successfully fabricated the GNRs from unzipping multiwalled carbon nanotubes (MWCNTs) using a two-step process (Figure 1-8 (a)). Briefly, the first step is the mild gas-phase oxidation. Pristine MWCNTs prepared from arc discharge were calcined in air at 500 °C to remove impurities and etch/oxidize MWCNTs at pre-existing defects and ends where etching pits were formed. The second step is the solution-phase sonication. The treated MWCNTs in the first step were dispersed in the 1,2-dichloroethane solution of poly(*m*-phenylenevinylene-co-2,5-dioctoxy-*p*-phenylenevinylene) with sonication and MWCNTs were initiated to unzip. By ultracentrifugation, GNRs could be obtained in the supernatant (Figure (b)-(d)). However, the width showed a broad range from 10 to 20 nm. Some other representative approaches including “top-down” methods and the respective GNRs obtained with various electric properties were listed in Table 1-1.

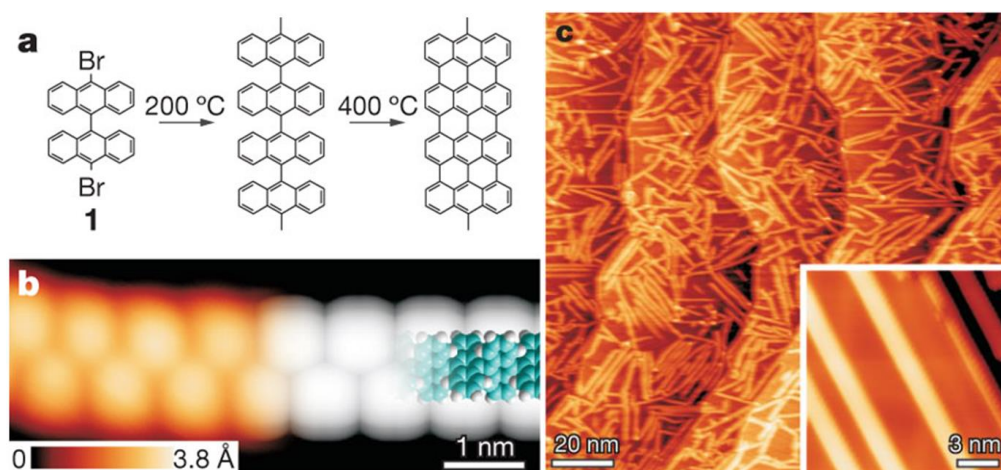


**Figure 1-9.** On-surface synthesis of GNRs from bianthryl monomer in a ultra high vacuum (UHV) environment. a, Reaction scheme from precursor 1 to 7-AGNRs. b, STM image of a polyanthrylene chain formed at 200 °C. c, Overview STM image of 7-AGNRs formed at 400 °C. The inset shows a higher-resolution STM image taken at 35K.<sup>23</sup> (Ref. [23], Copyright 2010, Nature Publishing Group.)

Although various approaches were developed (Table 1-1), the GNRs with controlled width and edge topologies of atomic precise remained a big challenge until the first example on “bottom-up” synthesis of GNRs utilizing the molecular precursor as building blocks was reported.<sup>23</sup> As shown in Figure 1-9a, the typical process involves two sequential steps, that is, polymerization of biradical precursor and metal-assisted dehydrogenation. In the first step,

thermal induced dehalogenation occurred leading to the formation of biradical intermediate of precursor (homolytic cleavage of the carbon-halogen bonds). The produced biradical species could be stabilized by the metal surface and diffuse to form linear polymer chains via radical addition reactions (Figure 1-9b). In the second step, further increasing the temperature induced the dehydrogenative C-C coupling reactions leading to the GNRs of defined structures (Figure 1-9c). The above-mentioned bottom-up strategy via coinage metal surface-assisted process showed strong versatility. A variety of GNRs with different geometries was fabricated using different halogenated precursors as building blocks,<sup>25</sup> including AGNRs,<sup>23,29,51,52,80,81</sup> ZGNRs,<sup>82</sup> cove-edged GNRs (CGNRs),<sup>83</sup> chevron-type GNRs,<sup>23</sup> heteroatoms-doped GNRs,<sup>84-88</sup> and even GNR heterojunctions.<sup>58,80,89,90</sup>

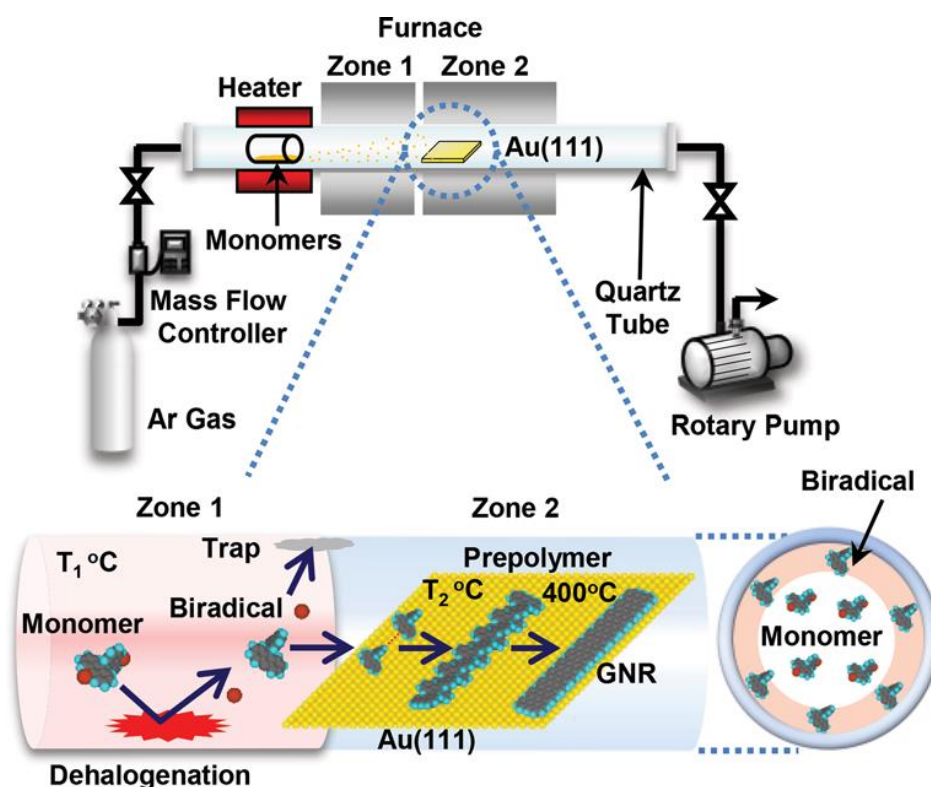


**Figure 1-10.** Experimental setup of 2Z-CVD with an illustration of the presumed GNR growth mechanism using 10,10'-dibromo-9,9'-bianthryl as a precursor.<sup>24</sup> (Ref. [24], Copyright 2014, John Wiley and Sons.)

Thus far, as for the bottom-up fabrication of GNRs, coinage metal-assisted on-surface synthesis, as a complementary approach of chemical synthesis in solution phase<sup>91-95</sup> and conversion of precursors inside CNTs,<sup>96,97</sup> is still a prevailing strategy to fabricate various types of

GNRs. Whereas, the conventional growth of GNRs usually proceeded in elaborate and costly UHV system, which required special instruments and extremely high vacuum. In order to realize large-scale production under low-vacuum conditions, Sakaguchi *et al.*<sup>24</sup> developed the two-zone chemical vapor deposition (2Z-CVD) system shown in Figure 1-10. The 2Z-CVD system is composed of a quartz tube ( $\phi$  26 mm, length 86 cm) as the reactor, a rotary pump which can evacuate the system to below  $7 \times 10^{-4}$  Torr, a two-zone electric furnace with temperature controllers, an Ar gas flow system with a mass flow controller, and a mantle heater for precursor sublimation (Figure 1-10). Ar gas was fed into the quartz tube at a flow rate of 500 sccm, leading to a vacuum of 1 Torr. The 2Z-CVD features independent temperature control over two zones, the precursor path (zone1) and the GNRs growth region (zone2). Dehalogenation of precursors was considered to occur in zone 1 via the collision of the precursors with the hot wall of the quartz tube, accompanied with the generation of high density biradical species. Afterwards, the produced biradical species polymerize on metal surface in zone 2 via radical addition reactions. Finally, metal-surface assisted dehydrogenative C-C coupling at higher temperature forms the fully aromatized GNRs. Compared with conventional UHV technique, high-throughput of self-assembled GNRs could be obtained.<sup>23,24</sup> The capability of producing high density biradical species in zone 1 is presumed to account for the densely packed and self-assembled GNRs.

Following the above strategy, GNRs with various width and edge geometry were synthesized using 2Z-CVD.<sup>24,27,28,98</sup> Recently, Sakaguchi *et al.*<sup>27</sup> reported the successful fabrication of acene-type GNRs of a width 1.45 nm (Figure 1-11) using a flexible “Z-bar-linkage” precursor. The precursor was considered firstly debrominated to form biradical species in zone 1 and adopted chiral conformations with height asymmetry on Au(111) surface in zone 2, followed by the formation of self-assembled homochiral polymers (Figure 1-11 (a) and (b)). When increasing the temperature in zone 2, the homochiral polymers underwent stepwise dehydrogenative C-C coupling until the fully aromatized acene-type GNRs were formed (Figure 1-11 (a) and (c)-(e)). Additionally, the GNRs film was isolated and characterized on the properties of field effect transistors (FETs) (channel length of 500 nm and width of 250 nm). The FETs exhibited excellent ambipolar semiconductor characteristics, a hole mobility of  $0.26 \text{ cm}^2 \text{ V}^{-1} \text{ s}^{-1}$  and an on/off ratio of 88.

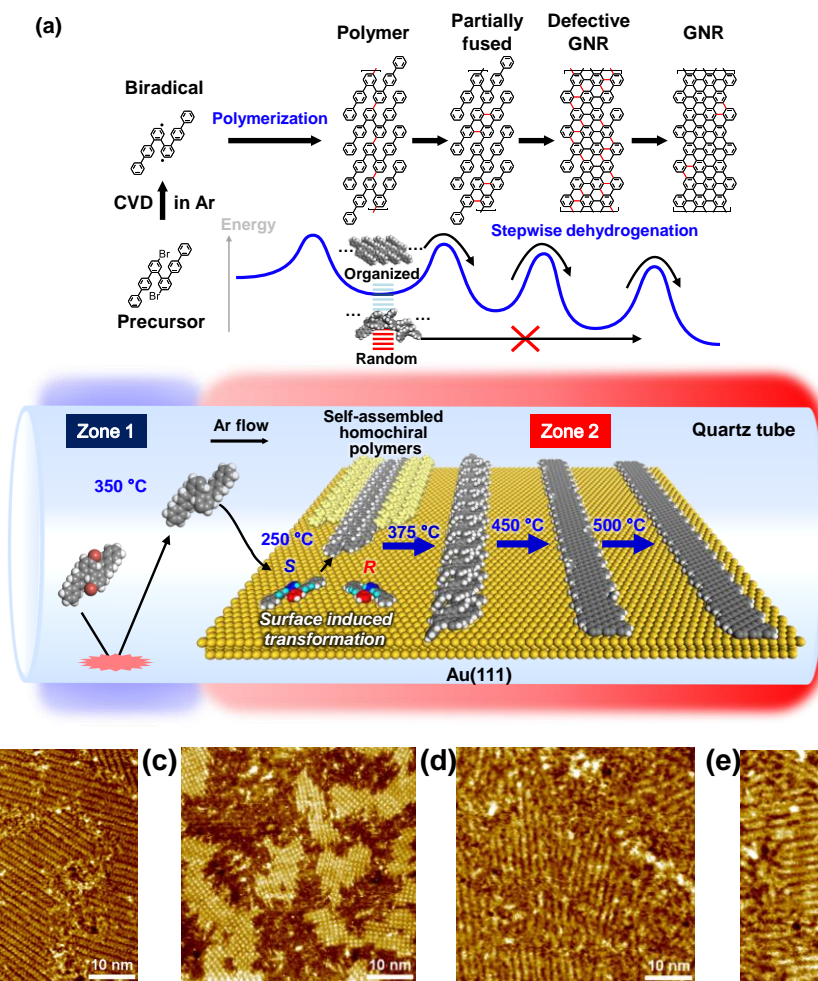


**Figure 1-11.** Selective growth of GNRs by 2Z-CVD. (a) Schematic representation of growth of acene-type GNRs from Z-bar-linkage precursor; (b)-(e) STM images of stepwise dehydrogenation from polymers to GNRs.<sup>27</sup> (Ref. [27], Copyright 2017, Nature Publishing Group.)

In addition, Müllen *et al.*<sup>99-101</sup> extended the CVD applications in the large-scale production of 9-AGNR ( $3p$ ), 7-AGNR ( $3p+1$ ), 5-AGNRs ( $3p+2$ ), and chevron-type GNRs. The CVD apparatus was equipped with a heating belt and a one-zone horizontal tube furnace instead of two zones in the reported 2Z-CVD system. Additionally, the mixed Ar (500 sccm) and  $H_2$  (100 sccm) gas flow was applied with a pressure of  $\sim 1.5$  mbar, where the  $H_2$  acted as  $O_2$  scavenger. This CVD apparatus is also capable of producing the self-assembled GNRs identical to 2Z-CVD (Figure 1-12). The attained chevron-type GNRs film could be isolated for the FETs device integration and showed a current on/off ratio up to 6000 in FET device.<sup>99</sup> The 9-AGNRs showed an optical band gap of  $\sim 1.0$  eV (with extended absorption into the infrared range) and intrinsic charge carrier mobility of  $\sim 350 \text{ cm}^2 \text{ V}^{-1} \text{ s}^{-1}$ .<sup>101</sup>



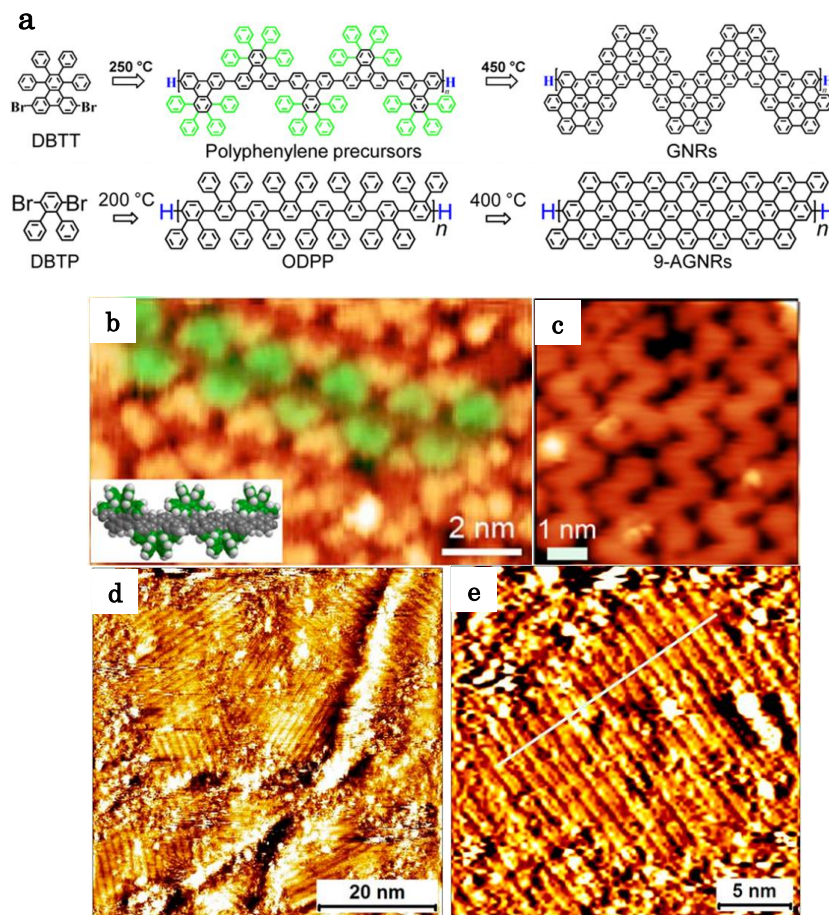


**Figure 1-12.** CVD synthesis of chevron-type GNRs and 9-AGNRs. (a) Reaction scheme from precursor to GNR. 5 K UHV STM topography of the polyphenylene precursors (b) and chevron-type GNRs (c).<sup>99</sup> (Ref. [99], Copyright 2016, The American Chemical Society). STM images of 9-AGNRs in large-scale (d) and small-scale (e), respectively.<sup>101</sup> (Ref. [100], Copyright 2017, The American Chemical Society.)

### 1-3. Two-dimensional (2D) graphene nanoribbon networks (GNNs)

Generally, the GNRs with defined width and edge structure are supposed to endow the specified electronic properties. The research up to date revealed a versatile way towards this structure controllable synthesis of GNRs, termed as bottom-up approaches. It usually refers to coinage metal-assisted on-surface synthesis and chemical synthesis in solution phase. The bottom-up synthesized GNR usually worked as the physically staggered GNRs film when integrated in the device.<sup>27,99,102</sup> Actually, the GNRs do not perform as well as that of theoretically

predicted,<sup>103,104</sup> partially due to the limited chain length and the interchain unconnection. Therefore, if GNRs were connected via conjugated covalent bonds into GNR networks, they may combine the semiconducting property of GNRs and superior property of graphene. This would provide a novel carbon-based material with enhanced electronic properties and applications.

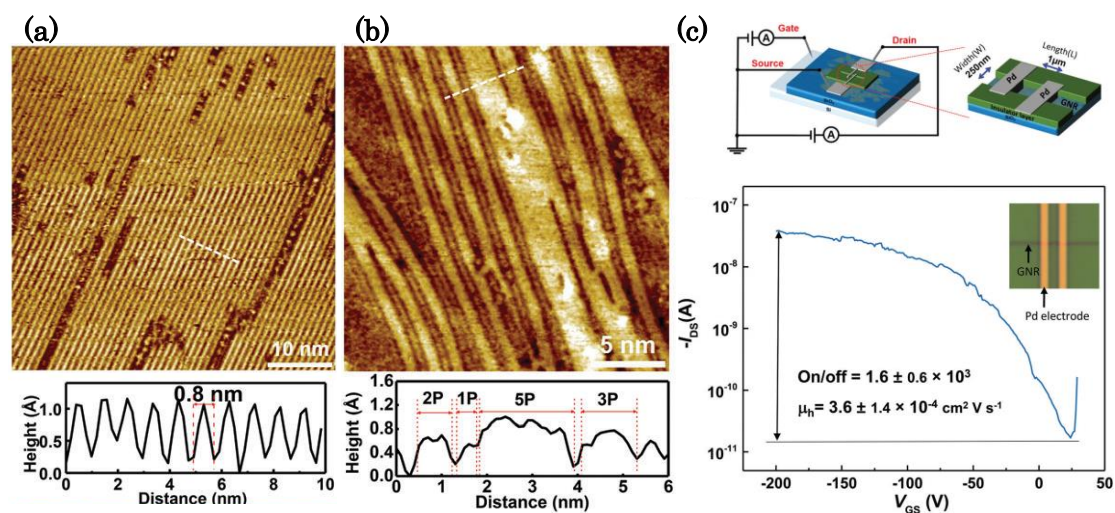


**Figure 1-13.** GNRs produced from fusion of poly(*p*-phenylene) (PPP) by 2Z-CVD.<sup>28</sup> (a) large-scale STM image of densely packed PPP chains. (b) small-scale STM image of fused PPP chains. (c) FET characteristics of GNRs. (Ref. [28], Copyright 2017, The Royal Society of Chemistry.)

Due to the solubility problem and edge termination with functional group, it is hardly to prepare the GNNs via chemical synthesis in solution phase. However, it is available by coinage metal-assisted on-surface synthesis, thanks to its capability in fabrication of proximal GNRs. Some preliminary research revealed that the GNRs with close proximity could fuse mutually in different manner at relatively higher temperature in UHV.<sup>30,54,105-107</sup> Nevertheless, the random alignment or large GNRs spacing resulted in the low fusion efficiency. Sakaguchi *et al.*<sup>28</sup> reported the highly efficient fusion of densely packed poly(*p*-phenylene) (PPP) chains into GNRs with interribbon connection via 2Z-CVD (Figure 1-13 (a) and (b)). The FET characterization showed a high on/off ratio of  $(1.6 \pm 0.6) \times 10^3$ , with a hole mobility of  $(3.6 \pm 1.4) \times 10^{-4} \text{ cm}^2 \text{ V}^{-1} \text{ s}^{-1}$  (Figure 1-13 (c)). Similarly, Müllen *et al.*<sup>100</sup> firstly prepared the self-assembled 5-AGNRs with close proximity via CVD, followed by annealing at higher temperature to obtain the fused GNRs. Whereas, either of the above two cases showed the fusion of AGNRs affording wider AGNRs, with limited linkage



between GNRs. It proved that the this kind of armchair-edged GNRs are not able to assemble more sophisticated structures, like nanopores.

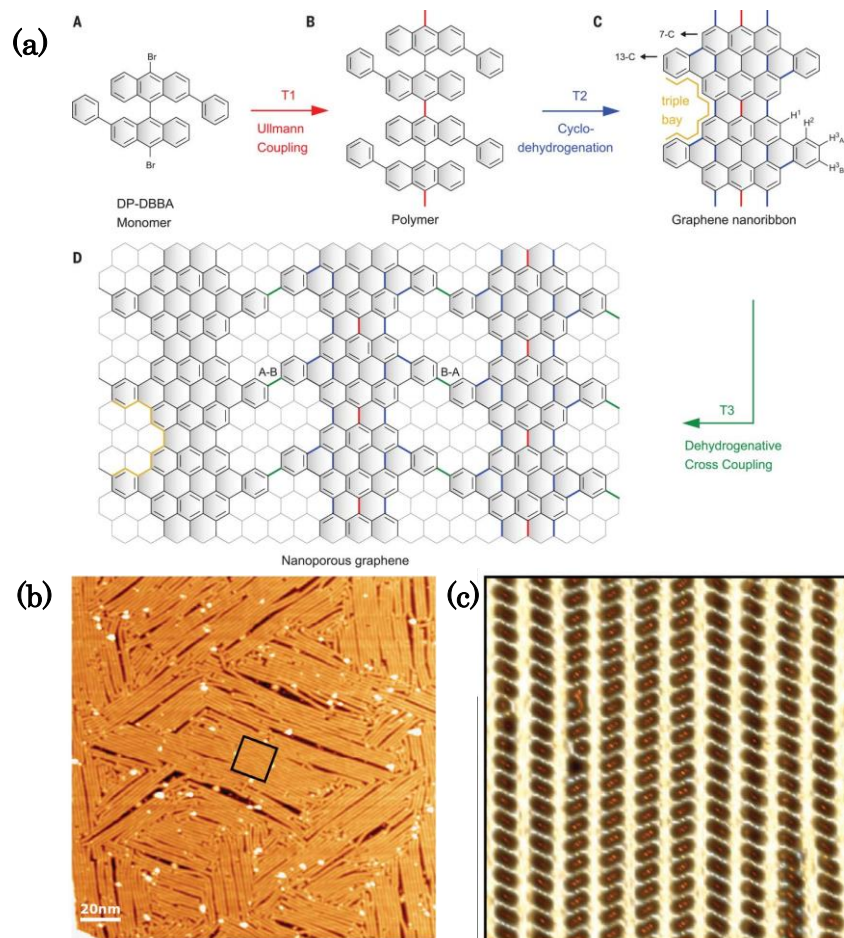


**Figure 1-14.** Fabrication of nanoporous graphene (NPG).<sup>108</sup> (a) Reaction scheme of hierarchical path from DP-DBBA precursor to NPG. (b) Constant-current STM image of NPG. (c) Laplacian-filtered topographic close-up image of NPG marked in (b). (Ref. [108], Copyright 2018, The American Association for the Advancement of Science.)

Other than the above-mentioned wider GNRs (integer width of original GNR), dehydrogenative C-C coupling between carefully designed GNR edges could also lead to nanoporous structure. Recently, Moreno *et al.*<sup>108</sup> reported the fabrication of 2D nanoporous graphene in UHV. As shown in Figure 1-14 (a), this approach involves the polymerization via Ullmann coupling, cyclo-dehydrogenation of polymers, and dehydrogenative cross-coupling between the GNRs. The crucial point is the self-assembled GNRs with triple bay regions at the edge periphery. When depositing the precursor DP-DBBA at 200 °C, the Au(111) surface could be

saturated with polymeric chains, subsequently converted into parallelly aligned 7-13-AGNR in long-range order. Afterwards, selective C-C bond formation of C-H<sup>3</sup> between the adjacent GNRs led to the NPG as large as 50 nm × 70 nm (pore size of 0.4 nm × 0.9 nm, pore density of 480 × 10<sup>3</sup> μm<sup>-2</sup>) (Figure 1-14 (b) and (c)). STS spectra of 7-13-AGNR showed a band gap of 1.0 eV (Figure 1-15 (a)). After interribbon fusion, the longitudinal bands remain unperturbed. However, owing to a bonding band formation, the interaction of two multibay states within a nanopore displayed an energy shift  $\Delta_{\text{bond}}$  of 0.30 eV (Figure 1-15 (b)). FET characterization of the prepared NPG showed a hole transport and high on/off ratio of ~10<sup>4</sup>.

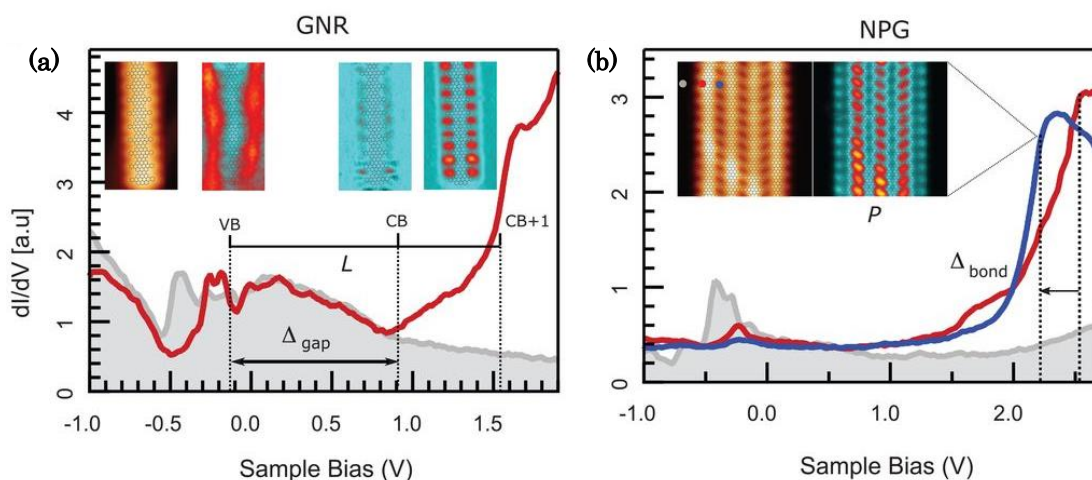


**Figure 1-15.** STS spectra of 7-13-AGNR and NPG.<sup>108</sup> (a) Acquired at the multibay edge of 7-13-AGNR. (b) Acquired at the multibay and a pore region of NPG. (Ref. [108], Copyright 2018, The American Association for the Advancement of Science.)

Another research also succeeded in the fabrication of graphene nanopores via lateral fusion of phenyl-functionalized chevron-type GNRs in UHV conditions (Figure 1-16).<sup>109</sup> Due to the  $\pi$ - $\pi$  interactions between peripheral phenyls, polymers could be formed in self-assembled manner (Figure 1-16 (a)), and then converted into mGNRs at higher temperature (Figure 1-16 (b)). Subsequently, two different lateral fusion modes between adjacent mGNRs led to the formation of different nanopore structures (Figure 1-16 (c)-(f)). However, more efforts need to be taken to fabricate 2D graphene nanostructures in long-range order for the practical applications in devices. The nanoporous graphene combines both semiconducting and nanosieving functionalities. Thus, the progress in the atomically precise fabrication would be expected to facilitate the experimental investigation of their practical applications, since the graphene nanopore structure attracted much

attention in many aspects, such as DNA sensing,<sup>110,111</sup> molecular sieving,<sup>112-116</sup> ionic sieves,<sup>117-119</sup> and water desalination,<sup>120</sup> etc.

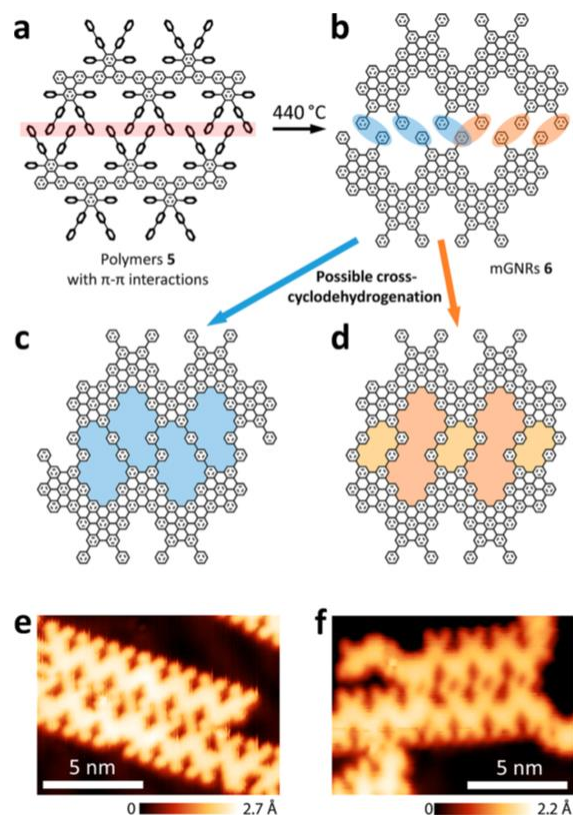


**Figure 1-16.** Lateral fusion of mGNRs.<sup>109</sup> (a) schematics of assembled polymers with  $\pi$ - $\pi$  interactions. (b) mGNRs with close proximity. (c,d) two variants of mGNRs lateral fusion. (e,f) STM images of two variants of mGNRs lateral fusion shown in (c,d), respectively. (Ref. [109], Copyright 2018, The American Chemical Society.)

#### 1-4. Thermoelectric (TE) application of GNRs

Thermoelectrics attracts more and more attention, which is dedicated to transforming the waste heat to electrical energy and thus alleviating energy crisis in the future. The principle of TE conversion is based on the Seebeck effect of materials that the temperature difference between two terminals can induce a potential difference, hence current generated in a closed electric circuit. Actually, high TE conversion efficiency of materials is necessary for the practical application considering the mechanical cycles and engineer challenges.<sup>121,122</sup> Generally, the TE conversion efficiency could be evaluated by a dimensionless factor, namely the figure of merit  $ZT$ ,<sup>122</sup>

$$ZT = S^2 \sigma T / \kappa = S^2 \sigma T / (\kappa_e + \kappa_l), \quad (1-1)$$

where  $S$  is the Seebeck coefficient,  $\sigma$  is the electrical conductivity,  $T$  is the absolute temperature,  $\kappa$  is the thermal conductivity,  $\kappa_e$  and  $\kappa_l$  are the electric and lattice thermal conductivity, respectively. The higher  $ZT$  represents a higher efficiency.<sup>123</sup> Thus, an excellent TE material should have high power factor ( $S^2\sigma$ ) and low thermal conductivity ( $\kappa$ ). The parameters in equation (1-1) are given by<sup>122,124</sup>

$$S = \frac{8\pi^2 k_B^2}{3eh^2} m^* T \left(\frac{\pi}{3n}\right)^{2/3} \quad (1-2)$$

$$\sigma = ne\mu \quad (1-3)$$

$$\kappa_e = L\sigma T \quad (1-4)$$

$$k_l = \frac{1}{3}(c_v v_s \lambda_{ph}), \quad (1-5)$$

where  $k_B$  is the Boltzmann constant,  $e$  is the carrier charge,  $h$  is the Planck's constant,  $m^*$  is the effective mass of charge carrier,  $n$  is the carrier concentration,  $\mu$  is the carrier mobility,  $L$  is the Lorenz number,  $c_v$  is the heat capacity,  $v_s$  is the sound velocity,  $\lambda_{ph}$  is the phonon mean free path (MFP, 1/3 changed to 1/2 for 2D graphene). In order to understand the mutual correlation more intuitively, the TE parameters variations as a function of charge carrier concentration ( $n$ ) are shown in Figure 1-17. Insulators are endowed with highest Seebeck coefficient and metals have highest electrical conductivity. However, the combined effect defined as power factor ( $S^2\sigma$ ) shows the highest value for semiconductors where the moderate thermal conductivity ( $\kappa$ ) also leads to the highest  $ZT$ .

Graphene exhibits many excellent properties, for example, superior mechanical strength and electrical conductivity, as detailed in chapter 1-1, which attracted much interest for the TE application. Nevertheless, high thermal conductivity of up to 5,000 W m/K<sup>6</sup> and poor Seebeck coefficient of only 30-60  $\mu$ V/K<sup>125</sup> limite its application. Several strategies,<sup>124</sup> such as

nanostructuring, doping, structural defects and boundary effects, aiming at simultaneous reduction of  $\kappa_1$  and increase of Seebeck coefficient were put forward. Additionally, integration of graphene into polymer matrix could harness the superior electrical conductivity of graphene and low thermal conductivity of polymer to enhance the TE property.<sup>126,127</sup> As for nanostructuring, tailoring the graphene into GNRs enables the opening of band gap, which is supposed to improve the power factor ( $S^2\sigma$ ) according to Figure 1-17. Meanwhile, the thermal conductivity in semiconductors is dominated by phonons contribution  $\kappa_1$ , with  $\kappa_e$  from electrons contribution being negligible.<sup>124</sup> When the dimension of structures is close to phonon de Broglie's wavelength,  $\kappa_1$  could be reduced via phonons scattering during the heat transport.<sup>125</sup>

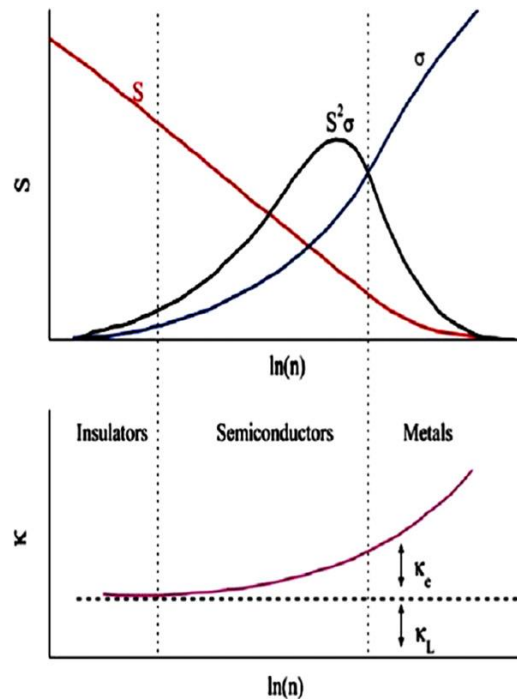


**Figure 1-17.** TE parameters as a function of charge carrier concentration  $n$  for a bulk material.<sup>122</sup>

(Ref. [122], Copyright 2012, Elsevier B.V.)

Although GNR is promising for TE application, numerous theoretical investigations manifested that many factors affect its performance, such as GNR width, edge geometry, defects, surface roughness, etc.<sup>128-135</sup> Zheng *et al.*<sup>129</sup> calculated the electronic and TE properties of AGNR and ZGNR of various widths using nonequilibrium Green function method and molecular dynamics simulations (Table 1-2). The results showed that AGNRs exhibit much better TE performance than ZGNRs, and  $ZT$  value increases as the decrease of ribbon width.

**Table 1-2.** Calculated electronic and TE properties of AGNR and ZGNR at optimized chemical potential  $\mu$ .<sup>129</sup>

Structure	Width (Å)	Gap (eV)	$\mu$ (eV)	$S$ ( $\mu$ V/K)	$G$ ( $\mu$ S)	$\lambda_e$ (nW/K)	$\lambda_p$ (nW/K)	$ZT$
3-AGNR	4.19	1.59	$\pm 0.73$	324	4.74	0.011	0.014	6.0
4-AGNR	5.42	2.32	$\pm 1.08$	351	4.01	0.012	0.015	5.4
5-AGNR	6.65	0.27	$\pm 0.09$	274	8.21	0.023	0.028	3.7
6-AGNR	7.88	0.99	$\pm 0.43$	275	8.20	0.019	0.034	3.5
3-ZGNR	6.97	0.37	$- 0.13$	235	22.07	0.039	0.18	1.7
4-ZGNR	9.10	0.39	$- 0.13$	240	22.72	0.045	0.19	1.7
5-ZGNR	11.23	0.47	$- 0.12$	243	22.92	0.050	0.26	1.3
6-ZGNR	13.36	0.44	$- 0.11$	213	31.71	0.053	0.32	1.1

Note:  $S$ , thermal power;  $G$ , electrical conductance;  $\lambda_e$ , electronic thermal conductance;  $\lambda_p$ , phonon derived thermal conductance;  $ZT$ , at room temperature.

Also,  $ZT$  can be improved by optimizing the doping level. Edge and lattice vacancy defects of AGNRs were found to increase the thermopower and decrease the thermal conductance, whereas the decrease of electronic conductance dominates the total effect resulting in the decrease of  $ZT$ .<sup>130</sup> However, edge disorder of ZGNRs is predicted to significantly reduce the phonon thermal transport with weakly detrimental to electronic conduction.<sup>131</sup> Liang *et al.*<sup>132,133</sup> theoretically investigated the TE properties of graphene nanowiggles (GNWs) and their straight AGNR counterpart (Figure 1-18). The calculations revealed that the wiggle-like edges in GNWs reduce the thermal conductance (Figure 1-18 (b)) and retain the excellent electronic conduction as well as higher thermal power (Figure 1-18 (c) and (d)), which leads to a significant enhancement of  $ZT$  compared to its straight GNR counterpart (Figure 1-18 (e)).<sup>132</sup> Further enhancement of TE properties was predicted to be achieved by a structural dislocation of GNWs.<sup>133</sup> Similarly, Huang *et al.*<sup>136</sup> calculated the TE properties of various hybridized kinked GNRs as shown in Figure 1-19. Introducing the kinked structure can significantly reduce the phonon derived thermal conductance

and improve the  $ZT$  value via structural optimization.<sup>136</sup>

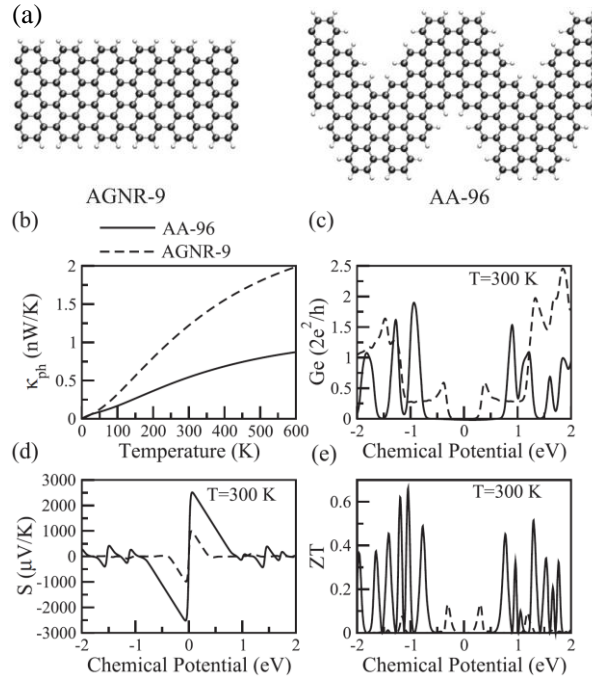


**Figure 1-18.** Theoretical calculated TE properties of 9-AGNR (left) and GNWs (right) counterpart.<sup>132</sup> (a) schematic representation of chemical structure. (b) thermal conductance ( $\kappa_{ph}$ ) from phonon contribution. (c) electrical conductance ( $G_e$ ). (d) thermal power ( $S$ ). (e) thermoelectric figure of merit ( $ZT$ ). (Ref. [132], Copyright 2012, American Physical Society.)

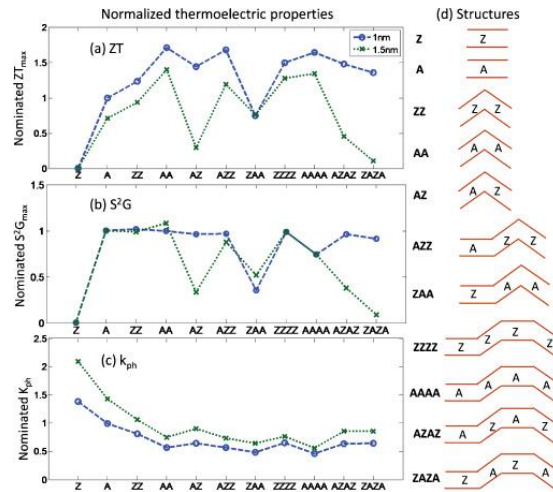


**Figure 1-19.** Normalized peak values of TE properties for various hybridized kinked GNRs (Z and A denote ZGNR and AGNR, respectively. Length, 1.0 nm; Width, 1.0 nm (circles) and 1.5 nm (cross markers)).<sup>136</sup> (Ref. [136], Copyright 2011, American Physical Society.)



Besides the wiggled or kinked structures, nanopores could also dramatically improve the TE properties of GNRs.<sup>137,138</sup> The thermal conductivity of GNRs reduced by introducing the pores while high  $ZT$  value could be obtained by tuning the pore dimensions to minimize the degradation of electrical properties.<sup>138</sup> However, most of investigations of GNRs for TE application are based on theoretical predictions. The experimental study is rarely reported.

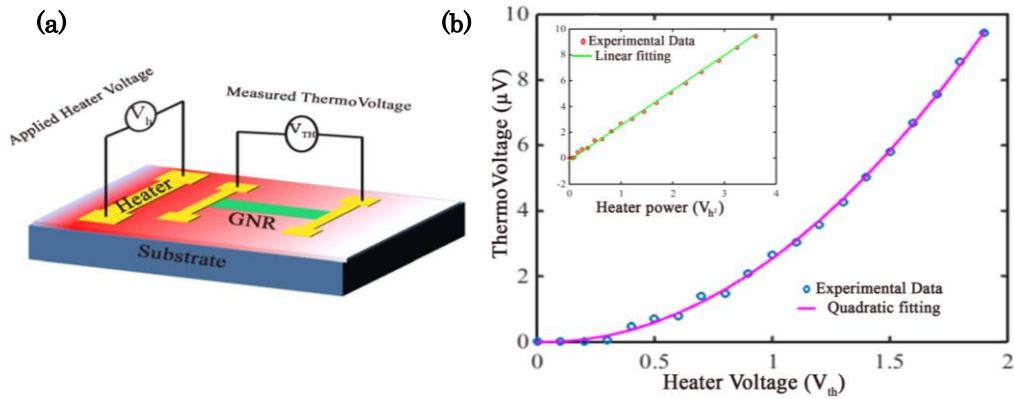


**Figure 1-20.** TE measurement of GNRs.<sup>139</sup> (a) Schematic diagram of the experimental setup. (b) Thermovoltage as a function of heater voltage for a single GNR device. (Ref. [139], Copyright 2016, AIP Publishing LLC.)

**Table 1-3.** Experimentally measured TE properties of bulk graphene and GNRs.<sup>139</sup>

	$G$ ( $\mu\text{S}$ ) <sup>a</sup>	$L$ ( $\mu\text{m}$ )	$S$ ( $\mu\text{V/K}$ ) <sup>a</sup>	$S^2G$ ( $\text{fW/K}^2$ )
Bulk	15	3.7	10	1.5
50 nm GNR	2	2.5	30	1.80
35 nm array	11	3.7	8	0.704
50 nm array	15	3.7	3	0.135

<sup>a</sup>Rounded to nearest integers.

In recent years, the TE properties of GNR and graphene nanomesh fabricated via top-down approaches were examined experimentally.<sup>139,140</sup> GNRs were patterned from CVD grown graphene using electron beam lithography (EBL), which were then integrated into the two-terminal devices for TE measurements (Figure 1-20 (a)).<sup>139</sup> The results revealed a quadratic relationship of thermovoltage with heater voltage (Figure 1-20 (b)). Both thermal power ( $S$ ) and power factor ( $S^2G$ ) were improved when patterning the bulk graphene into 50 nm wide GNR



(Table 1-3). However, the characterized TE properties of GNR are still far from satisfactory.

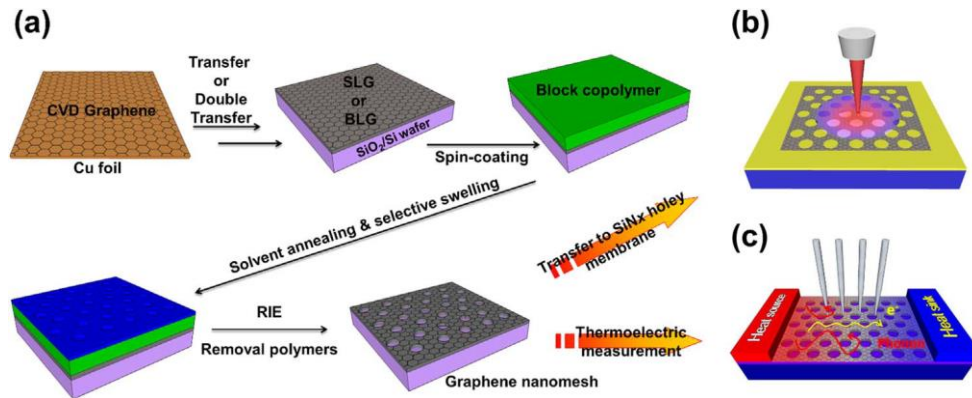


**Figure 1-21.** Fabrication and TE measurement of graphene nanomesh (GNM).<sup>140</sup> Schematic diagrams of (a) top-down fabrication process of GNM, (b) thermal conductivity measurement of GNM by optothermal Raman technique, (c) TE measurement and transport behavior of electrons and phonons with edge scattering. (Ref. [140], Copyright 2017, Elsevier B.V.)

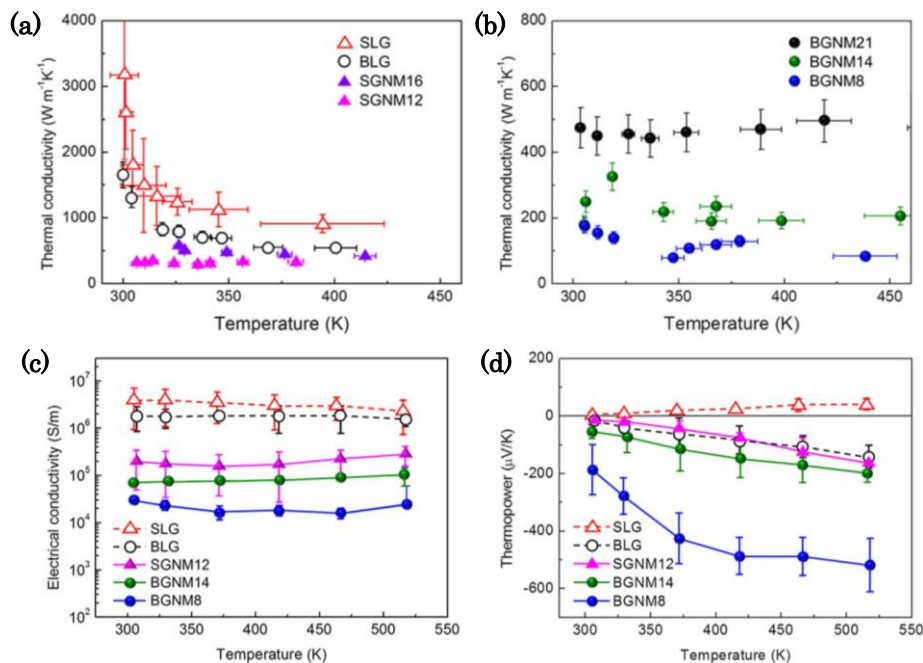


**Figure 1-22.** TE properties of graphene and GNMs.<sup>140</sup> (SLG: single layer graphene, BLG: bilayer graphene, SGNM: single layer graphene nanomesh, BGNM: bilayer graphene nanomesh, the number denotes neck width.) (Ref. [140], Copyright 2017, Elsevier B.V.)

Son *et al.*<sup>140</sup> experimentally measured the TE properties of graphene nanomesh (GNM). They

fabricated the GNMs of various neck widths based on block copolymer self-assembly and reactive ion etching (RIE) in a top-down process as shown in Figure 1-21. GNM showed a dramatically reduced thermal conductivity compared to graphene because of the extrinsic phonon scattering from the mesh-edges and phonon confinement (Figure 1-22 (a) and (b)). Also, the thermal conductivity of GNMs reduces as the decrease of neck width and reaches as low as  $\sim 78 \text{ W m}^{-1} \text{ K}^{-1}$  for BGNM8 (Figure 1-22 (a) and (b)). As expected, electrical conductivity decreased and thermopower increased up to  $-520 \mu\text{V K}^{-1}$  for BGNM8 when patterning the graphene into GNMs (Figure 1-22 (c) and (d)). In order to find TE materials of high efficiency (high  $ZT$  value), much efforts should be made to design and fabricate the suitable structures in the future.

### 1-5. Motivation and objectives

In previous study, by using 2Z-CVD, we succeeded in the fabrication of different types of self-assembled GNRs. The GNRs are densely packed and show close proximity, which enable the fusion reaction between GNRs to obtain the two-dimensional (2D) fully conjugated carbon nanostructures. The 2D GNRs structures were expected to show more superior properties over 1D GNRs.

In this study, the author focused on the fabrication of two-dimensional graphene-based materials by means of fusion of either nanographene molecules or graphene nanoribbons which act as building blocks, followed by the experimental characterization of their thermal and electrical properties. The feasibility was examined using 2Z-CVD and the products were imaged by room temperature scanning tunneling microscopy (STM). In chapter 3, the objective is to fabricate the 2D conjugated polymers via on-surface synthesis using nanographene molecules as building blocks. In chapter 4, the objective is to fabricate 2D graphene nanoribbon networks (GNNs) using the self-assembled GNRs as building blocks and characterize their thermal and electrical properties.

### 1-6. References

1. T. Ando, *NPG Asia Mater.*, **2009**, 1 (1), 17-21.

2. H. K. Chae, D. Y. Siberio-Perez, J. Kim, Y. Go, M. Eddaoudi, A. J. Matzger, M. O'Keeffe, and O. M. Yaghi, *Nature*, **2004**, 427 (6974), 523-527.
3. C. N. R. Rao, A. K. Sood, K. S. Subrahmanyam, and A. Govindaraj, *Angew. Chem. Int. Ed.*, **2009**, 48 (42), 7752-7777.
4. F. Liu, P. Ming, and J. Li, *Phys. Rev. B*, **2007**, 76 (6), 064120.
5. C. Lee, X. Wei, J. W. Kysar, and J. Hone, *Science*, **2008**, 321 (5887), 385-388.
6. A. A. Balandin, *Nat. Mater.*, **2011**, 10 (8), 569-581.
7. S. Morozov, K. Novoselov, M. Katsnelson, F. Schedin, D. Elias, J. A. Jaszczak, and A. Geim, *Phys. Rev. Lett.*, **2008**, 100 (1), 016602.
8. A. S. Mayorov, R. V. Gorbachev, S. V. Morozov, L. Britnell, R. Jalil, L. A. Ponomarenko, P. Blake, K. S. Novoselov, K. Watanabe, and T. Taniguchi, *Nano Lett.*, **2011**, 11 (6), 2396-2399.
9. J. S. Bunch, S. S. Verbridge, J. S. Alden, A. M. Van Der Zande, J. M. Parpia, H. G. Craighead, and P. L. McEuen, *Nano Lett.*, **2008**, 8 (8), 2458-2462.
10. A. Giesbers, G. Rietveld, E. Houtzager, U. Zeitler, R. Yang, K. Novoselov, A. Geim, and J. Maan, *Appl. Phys. Lett.*, **2008**, 93 (22), 222109.
11. A. Tzalenchuk, S. Lara-Avila, A. Kalaboukhov, S. Paolillo, M. Syväjärvi, R. Yakimova, O. Kazakova, T. Janssen, V. Fal'ko, and S. Kubatkin, *Nat. Nanotechnol.*, **2010**, 5 (3), 186-189.
12. J. Moser, A. Barreiro, and A. Bachtold, *Appl. Phys. Lett.*, **2007**, 91 (16), 163513.
13. K. S. Novoselov, A. K. Geim, S. V. Morozov, D. Jiang, Y. Zhang, S. V. Dubonos, I. V. Grigorieva, and A. A. Firsov, *Science*, **2004**, 306 (5696), 666-669.
14. S.-H. Cheng, K. Zou, F. Okino, H. R. Gutierrez, A. Gupta, N. Shen, P. Eklund, J. O. Sofo, and J. Zhu, *Phys. Rev. B*, **2010**, 81 (20), 205435.
15. D. C. Elias, R. R. Nair, T. Mohiuddin, S. Morozov, P. Blake, M. Halsall, A. C. Ferrari, D. Boukhvalov, M. Katsnelson, and A. Geim, *Science*, **2009**, 323 (5914), 610-613.
16. A. Castellanos - Gomez, M. Wojtaszek, N. Tombros, and B. J. van Wees, *Small*, **2012**, 8 (10), 1607-1613.
17. Z. Luo, J. Shang, S. Lim, D. Li, Q. Xiong, Z. Shen, J. Lin, and T. Yu, *Appl. Phys. Lett.*, **2010**, 97 (23), 233111.
18. B. R. Matis, J. S. Burgess, F. A. Bulat, A. L. Friedman, B. H. Houston, and J. W. Baldwin, *ACS Nano*, **2012**, 6 (1), 17-22.

19. E. Bekyarova, M. E. Itkis, P. Ramesh, C. Berger, M. Sprinkle, W. A. de Heer, and R. C. Haddon, *J. Am. Chem. Soc.*, **2009**, 131 (4), 1336-1337.
20. W. Zhang, C.-T. Lin, K.-K. Liu, T. Tite, C.-Y. Su, C.-H. Chang, Y.-H. Lee, C.-W. Chu, K.-H. Wei, and J.-L. Kuo, *ACS Nano*, **2011**, 5 (9), 7517-7524.
21. Y. Zhang, T.-T. Tang, C. Girit, Z. Hao, M. C. Martin, A. Zettl, M. F. Crommie, Y. R. Shen, and F. Wang, *Nature*, **2009**, 459 (7248), 820-823.
22. T. Ohta, A. Bostwick, T. Seyller, K. Horn, and E. Rotenberg, *Science*, **2006**, 313 (5789), 951-954.
23. J. Cai, P. Ruffieux, R. Jaafar, M. Bieri, T. Braun, S. Blankenburg, M. Muoth, A. P. Seitsonen, M. Saleh, and X. Feng, *Nature*, **2010**, 466 (7305), 470-473.
24. H. Sakaguchi, Y. Kawagoe, Y. Hirano, T. Iruka, M. Yano, and T. Nakae, *Adv. Mater.*, **2014**, 26 (24), 4134-4138.
25. L. Talirz, P. Ruffieux, and R. Fasel, *Adv. Mater.*, **2016**, 28 (29), 6222-6231.
26. J. P. Llinas, A. Fairbrother, G. B. Barin, W. Shi, K. Lee, S. Wu, B. Y. Choi, R. Braganza, J. Lear, and N. Kau, *Nat. Commun.*, **2017**, 8 (1), 633.
27. H. Sakaguchi, S. Song, T. Kojima, and T. Nakae, *Nat. Chem.*, **2017**, 9 (1), 57-63.
28. S. Song, T. Kojima, T. Nakae, and H. Sakaguchi, *Chem. Commun.*, **2017**, 53 (52), 7034-7036.
29. L. Talirz, H. Sode, T. Dumsclaff, S. Wang, J. R. Sanchez-Valencia, J. Liu, P. Shinde, C. A. Pignedoli, L. Liang, and V. Meunier, *ACS Nano*, **2017**, 11 (2), 1380-1388.
30. N. Merino-Déz, A. Garcia-Lekue, E. Carbonell-Sanromà, J. Li, M. Corso, L. Colazzo, F. Sedona, D. Sánchez-Portal, J. I. Pascual, and D. G. de Oteyza, *ACS Nano*, **2017**, 11 (11), 11661-11668.
31. J. Bai, X. Zhong, S. Jiang, Y. Huang, and X. Duan, *Nat. Nanotechnol.*, **2010**, 5 (3), 190-194.
32. X. Liang, Y.-S. Jung, S. Wu, A. Ismach, D. L. Olynick, S. Cabrini, and J. Bokor, *Nano Lett.*, **2010**, 10 (7), 2454-2460.
33. N. S. Safron, A. S. Brewer, and M. S. Arnold, *Small*, **2011**, 7 (4), 492-498.
34. K. Nakada, M. Fujita, G. Dresselhaus, and M. S. Dresselhaus, *Phys. Rev. B*, **1996**, 54 (24), 17954.
35. K. Wakabayashi, M. Fujita, H. Ajiki, and M. Sgrist, *Phys. Rev. B*, **1999**, 59 (12), 8271.
36. A. Celis, M. Nair, A. Taleb-Ibrahimi, E. Conrad, C. Berger, W. De Heer, and A. Tejada, *J. Phys.*

- D: Appl. Phys.*, **2016**, 49 (14), 143001.
37. B. Huang, F. Liu, J. Wu, B.-L. Gu, and W. Duan, *Phys. Rev. B*, **2008**, 77 (15), 153411.
38. P. Koskinen, S. Malola, and H. Häkkinen, *Phys. Rev. Lett.*, **2008**, 101 (11), 115502.
39. O. V. Yazyev and M. Katsnelson, *Phys. Rev. Lett.*, **2008**, 100 (4), 047209.
40. S. Okada, *Phys. Rev. B*, **2008**, 77 (4), 041408.
41. L. Pisani, J. Chan, B. Montanari, and N. Harrison, *Phys. Rev. B*, **2007**, 75 (6), 064418.
42. A. Yamashiro, Y. Shimoi, K. Harigaya, and K. Wakabayashi, *Phys. Rev. B*, **2003**, 68 (19), 193410.
43. E.-J. Kan, Z. Li, J. Yang, and J. Hou, *Appl. Phys. Lett.*, **2007**, 91 (24), 243116.
44. Y.-W. Son, M. L. Cohen, and S. G. Louie, *Phys. Rev. Lett.*, **2006**, 97 (21), 216803.
45. Y.-W. Son, M. L. Cohen, and S. G. Louie, *Nature*, **2006**, 444 (7117), 347-349.
46. M. Fujita, K. Wakabayashi, K. Nakada, and K. Kusakabe, *J. Phys. Soc. Jpn.*, **1996**, 65 (7), 1920-1923.
47. S. Okada and A. Oshiyama, *Phys. Rev. Lett.*, **2001**, 87 (14), 146803.
48. H. Lee, Y.-W. Son, N. Park, S. Han, and J. Yu, *Phys. Rev. B*, **2005**, 72 (17), 174431.
49. L. Yang, C.-H. Park, Y.-W. Son, M. L. Cohen, and S. G. Louie, *Phys. Rev. Lett.*, **2007**, 99 (18), 186801.
50. E. Kan, Z. Li, and J. Yang, *Physics and Applications of Graphene-theory*, **2011**, 331-348.
51. A. Kimouche, M. M. Ervasti, R. Drost, S. Halonen, A. Harju, P. M. Joensuu, J. Sainio, and P. Liljeroth, *Nat. Commun.*, **2015**, 6, 10177.
52. H. Zhang, H. Lin, K. Sun, L. Chen, Y. Zagranyarski, N. Aghdassi, S. Duhm, Q. Li, D. Zhong, and Y. Li, *J. Am. Chem. Soc.*, **2015**, 137 (12), 4022-4025.
53. M. Ezawa, *Phys. Rev. B*, **2006**, 73 (4), 045432.
54. H. Huang, D. Wei, J. Sun, S. L. Wong, Y. P. Feng, A. C. Neto, and A. T. S. Wee, *Sci. Rep.*, **2012**, 2, 983.
55. D. Prezzi, D. Varsano, A. Ruini, A. Marini, and E. Molinari, *Phys. Rev. B*, **2008**, 77 (4), 041404.
56. T. Wassmann, A. P. Seitsonen, A. M. Saitta, M. Lazzeri, and F. Mauri, *Phys. Rev. Lett.*, **2008**, 101 (9), 096402.
57. P. Wagner, C. P. Ewels, J.-J. Adjizian, L. Magaud, P. Pochet, S. Roche, A. Lopez-Bezanilla, V.

- V. Ivanovskaya, A. Yaya, and M. Rayson, *J. Phys. Chem. C*, **2013**, 117 (50), 26790-26796.
58. G. D. Nguyen, H.-Z. Tsai, A. A. Omrani, T. Marangoni, M. Wu, D. J. Rizzo, G. F. Rodgers, R. R. Cloke, R. A. Durr, and Y. Sakai, *Nat. Nanotechnol.*, **2017**, 12 (11), 1077-1082.
59. E. Carbonell-Sanromà, J. Hieulle, M. Vilas-Varela, P. Brandimarte, M. Iraola, A. Barragán, J. Li, M. Abadía, M. Corso, D. Sánchez-Portal, D. Peñã, and J. I. Pascual, *ACS Nano*, **2017**, 11 (7), 7355-7361.
60. X. Wang and H. Dai, *Nat. Chem.*, **2010**, 2 (8), 661-665.
61. M. Y. Han, B. Özyilmaz, Y. Zhang, and P. Kim, *Phys. Rev. Lett.*, **2007**, 98 (20), 206805.
62. Z. Chen, Y.-M. Lin, M. J. Rooks, and P. Avouris, *Physica E*, **2007**, 40 (2), 228-232.
63. J. Bai, X. Duan, and Y. Huang, *Nano Lett.*, **2009**, 9 (5), 2083-2087.
64. G. Liu, Y. Wu, Y.-M. Lin, D. B. Farmer, J. A. Ott, J. Bruley, A. Grill, P. Avouris, D. Pfeiffer, and A. A. Balandin, *ACS Nano*, **2012**, 6 (8), 6786-6792.
65. Y.-S. Shin, J. Y. Son, M.-H. Jo, Y.-H. Shin, and H. M. Jang, *J. Am. Chem. Soc.*, **2011**, 133 (15), 5623-5625.
66. L. Jiao, L. Xie, and H. Dai, *Nano Res.*, **2012**, 5 (4), 292-296.
67. L. C. Campos, V. R. Manfrinato, J. D. Sanchez-Yamagishi, J. Kong, and P. Jarillo-Herrero, *Nano Lett.*, **2009**, 9 (7), 2600-2604.
68. L. Ci, Z. Xu, L. Wang, W. Gao, F. Ding, K. F. Kelly, B. I. Yakobson, and P. M. Ajayan, *Nano Res.*, **2008**, 1 (2), 116-122.
69. S. S. Datta, D. R. Strachan, S. M. Khamis, and A. C. Johnson, *Nano Lett.*, **2008**, 8 (7), 1912-1915.
70. L. Jiao, X. Wang, G. Diankov, H. Wang, and H. Dai, *Nat. Nanotechnol.*, **2010**, 5 (5), 321-325.
71. T. Kato and R. Hatakeyama, *Nat. Nanotechnol.*, **2012**, 7 (10), 651-656.
72. W. Xu and T.-W. Lee, *Mater. Horizons*, **2016**, 3 (3), 186-207.
73. X. Li, X. Wang, L. Zhang, S. Lee, and H. Dai, *Science*, **2008**, 319 (5867), 1229-1232.
74. X. Wang, Y. Ouyang, L. Jiao, H. Wang, L. Xie, J. Wu, J. Guo, and H. Dai, *Nat. Nanotechnol.*, **2011**, 6 (9), 563-567.
75. M. Sprinkle, M. Ruan, Y. Hu, J. Hankinson, M. Rubio-Roy, B. Zhang, X. Wu, C. Berger, and W. A. De Heer, *Nat. Nanotechnol.*, **2010**, 5 (10), 727-731.
76. G. Xie, Z. Shi, R. Yang, D. Liu, W. Yang, M. Cheng, D. Wang, D. Shi, and G. Zhang, *Nano*

- Lett.*, **2012**, 12 (9), 4642-4646.
77. L. Jiao, L. Zhang, X. Wang, G. Diankov, and H. Dai, *Nature*, **2009**, 458 (7240), 877-880.
78. D. V. Kosynkin, A. L. Higginbotham, A. Sinitskii, J. R. Lomeda, A. Dimiev, B. K. Price, and J. M. Tour, *Nature*, **2009**, 458 (7240), 872-876.
79. C. Tao, L. Jiao, O. V. Yazyev, Y.-C. Chen, J. Feng, X. Zhang, R. B. Capaz, J. M. Tour, A. Zettl, and S. G. Louie, *Nat. Phys.*, **2011**, 7 (8), 616-620.
80. Y.-C. Chen, T. Cao, C. Chen, Z. Pedramrazi, D. Haberer, D. G. De Oteyza, F. R. Fischer, S. G. Louie, and M. F. Crommie, *Nat. Nanotechnol.*, **2015**, 10 (2), 156-160.
81. Y.-C. Chen, D. G. De Oteyza, Z. Pedramrazi, C. Chen, F. R. Fischer, and M. F. Crommie, *ACS Nano*, **2013**, 7 (7), 6123-6128.
82. P. Ruffieux, S. Wang, B. Yang, C. Sánchez-Sánchez, J. Liu, T. Dienel, L. Talirz, P. Shinde, C. A. Pignedoli, and D. Passerone, *Nature*, **2016**, 531 (7595), 489-492.
83. J. Liu, B.-W. Li, Y.-Z. Tan, A. Giannakopoulos, C. Sanchez-Sanchez, D. Beljonne, P. Ruffieux, R. Fasel, X. Feng, and K. Müllen, *J. Am. Chem. Soc.*, **2015**, 137 (18), 6097-6103.
84. C. Bronner, S. Stremlau, M. Gille, F. Brauße, A. Haase, S. Hecht, and P. Tegeder, *Angew. Chem. Int. Ed.*, **2013**, 52 (16), 4422-4425.
85. G. D. Nguyen, F. M. Toma, T. Cao, Z. Pedramrazi, C. Chen, D. J. Rizzo, T. Joshi, C. Bronner, Y.-C. Chen, and M. Favaro, *J. Phys. Chem. C*, **2016**, 120 (5), 2684-2687.
86. S. Kawai, S. Saito, S. Osumi, S. Yamaguchi, A. S. Foster, P. Spijker, and E. Meyer, *Nat. Commun.*, **2015**, 6, 1-6.
87. R. R. Cloke, T. Marangoni, G. D. Nguyen, T. Joshi, D. J. Rizzo, C. Bronner, T. Cao, S. G. Louie, M. F. Crommie, and F. R. Fischer, *J. Am. Chem. Soc.*, **2015**, 137 (28), 8872-8875.
88. S. Kawai, S. Nakatsuka, T. Hatakeyama, R. Pawlak, T. Meier, J. Tracey, E. Meyer, and A. S. Foster, *Sci. Adv.*, **2018**, 4 (4), eaar7181.
89. S. Blankenburg, J. Cai, P. Ruffieux, R. Jaafar, D. Passerone, X. Feng, K. Müllen, R. Fasel, and C. A. Pignedoli, *ACS Nano*, **2012**, 6 (3), 2020-2025.
90. J. Cai, C. A. Pignedoli, L. Talirz, P. Ruffieux, H. Söde, L. Liang, V. Meunier, R. Berger, R. Li, and X. Feng, *Nat. Nanotechnol.*, **2014**, 9 (11), 896-900.
91. A. Narita, X. Feng, Y. Hernandez, S. A. Jensen, M. Bonn, H. Yang, I. A. Verzhbitskiy, C. Casiraghi, M. R. Hansen, and A. H. Koch, *Nat. Chem.*, **2014**, 6 (2), 126-132.

92. T. H. Vo, M. Shekhirev, D. A. Kunkel, M. D. Morton, E. Berglund, L. Kong, P. M. Wilson, P. A. Dowben, A. Enders, and A. Sinitskii, *Nat. Commun.*, **2014**, 5 (1), 1-8.
93. W. Yang, A. Lucotti, M. Tommasini, and W. A. Chalifoux, *J. Am. Chem. Soc.*, **2016**, 138 (29), 9137-9144.
94. G. Li, K.-Y. Yoon, X. Zhong, J. Wang, R. Zhang, J. R. Guest, J. Wen, X.-Y. Zhu, and G. Dong, *Nat. Commun.*, **2018**, 9 (1), 1-9.
95. Y. Yano, N. Mitoma, K. Matsushima, F. Wang, K. Matsui, A. Takakura, Y. Miyauchi, H. Ito, and K. Itami, *Nature*, **2019**, 571 (7765), 387-392.
96. A. Chuvilin, E. Bichoutskaia, M. Gimenez-Lopez, T. Chamberlain, G. Rance, N. Kuganathan, J. Biskupek, U. Kaiser, and A. Khlobystov, *Nat. Mater.*, **2011**, 10 (9), 687-692.
97. A. V. Talyzin, I. V. Anoshkin, A. V. Krasheninnikov, R. M. Nieminen, A. G. Nasibulin, H. Jiang, and E. I. Kauppinen, *Nano Lett.*, **2011**, 11 (10), 4352-4356.
98. S. Song, G. Huang, T. Kojima, T. Nakae, H. Uno, and H. Sakaguchi, *Chem. Lett.*, **2017**, 46 (10), 1525-1527.
99. Z. Chen, W. Zhang, C.-A. Palma, A. Lodi Rizzini, B. Liu, A. Abbas, N. Richter, L. Martini, X.-Y. Wang, and N. Cavani, *J. Am. Chem. Soc.*, **2016**, 138 (47), 15488-15496.
100. Z. Chen, H. I. Wang, N. Bilbao, J. Teyssandier, T. Prechtel, N. Cavani, A. Tries, R. Biagi, V. De Renzi, and X. Feng, *J. Am. Chem. Soc.*, **2017**, 139 (28), 9483-9486.
101. Z. Chen, H. I. Wang, J. Teyssandier, K. S. Mali, T. Dumschlaff, I. Ivanov, W. Zhang, P. Ruffieux, R. Fasel, and H. J. Räder, *J. Am. Chem. Soc.*, **2017**, 139 (10), 3635-3638.
102. P. B. Bennett, Z. Pedramrazi, A. Madani, Y.-C. Chen, D. G. de Oteyza, C. Chen, F. R. Fischer, M. F. Crommie, and J. Bokor, *Appl. Phys. Lett.*, **2013**, 103 (25), 253114.
103. N. Harada, S. Sato, and N. Yokoyama, *Jpn. J. Appl. Phys.*, **2013**, 52 (9R), 094301.
104. J.-H. Hur and D.-K. Kim, *Nanotechnology*, **2018**, 29 (18), 185202.
105. T. Dienel, S. Kawai, H. Söde, X. Feng, K. Müllen, P. Ruffieux, R. Fasel, and O. Gröning, *Nano Lett.*, **2015**, 15 (8), 5185-5190.
106. A. Basagni, F. Sedona, C. A. Pignedoli, M. Cattelan, L. Nicolas, M. Casarin, and M. Sambì, *J. Am. Chem. Soc.*, **2015**, 137 (5), 1802-1808.
107. P. Han, K. Akagi, F. Federici Canova, R. Shimizu, H. Oguchi, S. Shiraki, P. S. Weiss, N. Asao, and T. Hitosugi, *ACS Nano*, **2015**, 9 (12), 12035-12044.



108. C. Moreno, M. Vilas-Varela, B. Kretz, A. Garcia-Lekue, M. V. Costache, M. Paradinas, M. Panighel, G. Ceballos, S. O. Valenzuela, and D. Pe ña, *Science*, **2018**, 360 (6385), 199-203.
109. M. Shekhirev, P. Zahl, and A. Sinitskii, *ACS Nano*, **2018**, 12 (8), 8662-8669.
110. S. Garaj, W. Hubbard, A. Reina, J. Kong, D. Branton, and J. Golovchenko, *Nature*, **2010**, 467 (7312), 190-193.
111. L. Liang, P. Cui, Q. Wang, T. Wu, H. Ågren, and Y. Tu, *RSC Adv.*, **2013**, 3 (7), 2445-2453.
112. Y. Li and C. Wu, *Carbon*, **2018**, 134, 145-152.
113. H. Du, J. Li, J. Zhang, G. Su, X. Li, and Y. Zhao, *J. Phys. Chem. C*, **2011**, 115 (47), 23261-23266.
114. D. Li, W. Hu, J. Zhang, H. Shi, Q. Chen, T. Sun, L. Liang, and Q. Wang, *J. Phys. Chem. C*, **2015**, 119 (45), 25559-25565.
115. S. P. Koenig, L. Wang, J. Pellegrino, and J. S. Bunch, *Nat. Nanotechnol.*, **2012**, 7 (11), 728-732.
116. D.-e. Jiang, V. R. Cooper, and S. Dai, *Nano Lett.*, **2009**, 9 (12), 4019-4024.
117. K. Sint, B. Wang, and P. Kr á, *J. Am. Chem. Soc.*, **2008**, 130 (49), 16448-16449.
118. Y. Kang, Z. Zhang, H. Shi, J. Zhang, L. Liang, Q. Wang, H. Ågren, and Y. Tu, *Nanoscale*, **2014**, 6 (18), 10666-10672.
119. A. Smolyanitsky, E. Paulechka, and K. Kroenlein, *ACS Nano*, **2018**, 12 (7), 6677-6684.
120. D. Cohen-Tanugi and J. C. Grossman, *Nano Lett.*, **2012**, 12 (7), 3602-3608.
121. L. E. Bell, *Science*, **2008**, 321 (5895), 1457-1461.
122. Z.-G. Chen, G. Han, L. Yang, L. Cheng, and J. Zou, *Prog. Nat. Sci.*, **2012**, 22 (6), 535-549.
123. C. B. Vining, *Nat. Mater.*, **2009**, 8 (2), 83-85.
124. T. A. Amollo, G. T. Mola, M. Kirui, and V. O. Nyamori, *Crit. Rev. Solid State Mater. Sci.*, **2018**, 43 (2), 133-157.
125. Z.-Y. Juang, C.-C. Tseng, C.-H. Chen, and L.-J. Li, *AAPPS Bull.*, **2013**, 23 (4), 14-18.
126. K. Zhang, Y. Zhang, and S. Wang, *Sci. Rep.*, **2013**, 3, 3448.
127. G. H. Kim, D. H. Hwang, and S. I. Woo, *Phys. Chem. Chem. Phys.*, **2012**, 14 (10), 3530-3536.
128. F. Mazzamuto, V. H. Nguyen, Y. Apertet, C. Ca ãr, C. Chassat, J. Saint-Martin, and P. Dollfus, *Phys. Rev. B*, **2011**, 83 (23), 235426.

129. H. Zheng, H. Liu, X. Tan, H. Lv, L. Pan, J. Shi, and X. Tang, *Appl. Phys. Lett.*, **2012**, 100 (9), 093104.
130. Y. Ouyang and J. Guo, *Appl. Phys. Lett.*, **2009**, 94 (26), 263107.
131. H. Sevinçli and G. Cuniberti, *Phys. Rev. B*, **2010**, 81 (11), 113401.
132. L. Liang, E. Cruz-Silva, E. C. Girescu, and V. Meunier, *Phys. Rev. B*, **2012**, 86 (11), 115438.
133. L. Liang and V. Meunier, *Appl. Phys. Lett.*, **2013**, 102 (14), 143101.
134. Z.-X. Xie, L.-M. Tang, C.-N. Pan, K.-M. Li, K.-Q. Chen, and W. Duan, *Appl. Phys. Lett.*, **2012**, 100 (7), 073105.
135. H. Xiao, W. Cao, T. Ouyang, X. Xu, Y. Ding, and J. Zhong, *Appl. Phys. Lett.*, **2018**, 112 (23), 233107.
136. W. Huang, J.-S. Wang, and G. Liang, *Phys. Rev. B*, **2011**, 84 (4), 045410.
137. H. Sadeghi, S. Sangtarash, and C. J. Lambert, *Beilstein J. Nanotechnol.*, **2015**, 6 (1), 1176-1182.
138. M. S. Hossain, F. Al-Dirini, F. M. Hossain, and E. Skafidas, *Sci. Rep.*, **2015**, 5, 11297.
139. M. S. Hossain, D. H. Huynh, P. D. Nguyen, L. Jiang, T. C. Nguyen, F. Al-Dirini, F. M. Hossain, and E. Skafidas, *J. Appl. Phys.*, **2016**, 119 (12), 125106.
140. J. Oh, H. Yoo, J. Choi, J. Y. Kim, D. S. Lee, M. J. Kim, J.-C. Lee, W. N. Kim, J. C. Grossman, and J. H. Park, *Nano Energy*, **2017**, 35, 26-35.

## Chapter 2

### Experimental

#### 2-1. General information

##### 2-1-1. Materials

The commercially available reagents, catalyst and solvents were purchased from Sigma-aldrich Co., Ltd, TCI Co., Ltd, Nacalai Co., Ltd, and other commercial suppliers, and used as received, unless otherwise stated.

##### 2-1-2. Methods

All manipulations were performed under N<sub>2</sub> atmosphere using standard Schlenk techniques. NMR spectra were recorded with JEOL JNM-ECP300 or JEOL JNM-ECA600 (300 MHz or 600 MHz for <sup>1</sup>H, 150 MHz for <sup>13</sup>C) instruments. NMR spectra were reported in parts per million from internal tetramethylsilane ( $\delta$  0.00 ppm for chloroform-d) or residual solvent ( $\delta$  7.26 ppm for chloroform-d) for <sup>1</sup>H NMR, and from the solvent carbon ( $\delta$  77.00 ppm for chloroform-d) for <sup>13</sup>C NMR. Thin-layer chromatography (TLC) and column chromatography were performed on Art. 5554 (Merck KGaA) and Silica Gel 60N (Kanto Chemical Co.), respectively. Gel permeation chromatography (GPC) was performed on a LC-Forte system (YMC Co. Ltd.) with JAIGEL 1HR and 2HR polystyrene columns (eluent: CHCl<sub>3</sub>, flow: 10 mL/min). Elemental analyses was carried out at the Microanalytical Laboratory of the Institute for Chemical Research, Kyoto University.

##### 2-1-3. Au(111) substrates

Substrates consisting of Au(111) on mica and glass were prepared by using an electron-beam vacuum deposition system. Evaporated Au atoms were deposited onto a mica or glass substrate that was pre-heated to 350 °C under a vacuum of  $2 \times 10^{-8}$  Torr. Deposition was performed at a rate of  $0.5 \text{ \AA s}^{-1}$ , with a final thickness of 30 nm.

#### **2-1-4. Two-zone chemical vapor deposition (2Z-CVD)**

The 2Z-CVD system is composed of a quartz tube ( $\phi$  26 mm, length 86 cm) as the reactor, a rotary pump which can evacuate the system to below  $7 \times 10^{-4}$  Torr, a two-zone electric furnace with temperature controllers, an Ar gas flow system with a mass flow controller, and a mantle heater for precursor sublimation. Ar gas was fed into the quartz tube at a flow rate of 500 sccm, resulting in a vacuum of 1 Torr. Before the CVD process, the quartz tube was annealed at 1000 °C for 20 min to remove impurities that can deactivate precursor radicals. The precursor (for DBOP, 20  $\mu$ g, prepared by casting 200  $\mu$ L of precursor solution, 0.1 mg mL<sup>-1</sup> in toluene; for GNNs synthesis, 40  $\mu$ g, prepared by casting 40  $\mu$ L of precursor solution, 1.0 mg mL<sup>-1</sup> in toluene) in a quartz boat was placed in the quartz tube at the position of the mantle heater before zone 1. An Au(111)-deposited mica or glass substrate was placed in zone 2 of the quartz tube. For DBOP, the CVD process was conducted in two sequential steps: firstly, zone 1 (the path of the precursors) and zone 2 were heated to 350 and 250 °C, respectively, and the precursors were sublimated using the mantle heater by heating to 350 °C for 15 min. Finally, to anneal the sample, the temperature of zone 2 was increased stepwise to the final temperature. GNNs synthesis was performed in two stages. In the first stage, GNRs were fabricated on Au(111). The precursors were sublimated using the mantle heater. The path of the precursors through the quartz tube of zone 1 was heated to 350 °C, and zone 2 was set at 250 °C. The pre-polymers were grown on Au(111) by the radical polymerization of the precursors. The temperature of zone 2 was increased to the given temperature for converting the pre-polymers into GNRs via dehydrogenation reactions. In the second stage, GNRs were transformed into the GNN by interchain reactions at 600 °C.

#### **2-2. Characterization techniques of 1D GNRs and 2D GNNs**

##### **2-2-1. Scanning tunneling microscopy (STM) measurements**

STM measurements were performed with a constant current mode using a commercial instrument (PicoSPM; Keysight Technologies Inc., formerly Molecular Imaging) under an Ar atmosphere at room temperature.<sup>1</sup> All STM images were acquired at a tip bias of 0.2 V with a

constant current of 5–20 pA. An electrochemically etched Pt–Ir (80 : 20) wire was used as the STM tip. Scanning tunneling spectroscopy was used to measure the  $dI/dV$  curves. The band gap was defined from the distance between the extrapolated intercepts of the  $dI/dV$  curve with a horizontal line positioned at the  $dI/dV$  curve minimum.<sup>2</sup>

### **2-2-2. Raman spectra**

Raman spectroscopy measurement was performed using a laser Raman microscope (LV-RAM500/532; Lambda Vision Inc.) with a 532 nm laser. A 0.75/50× microscope objective was used. The diameter of the laser spot is considered in the order of 1 μm. A laser power of 70 mW was used, with an exposure time of 10 seconds and a 10 times averaging. The spectra showed a good reproducibility.

### **2-2-3. Scanning electron microscopy (SEM)**

SEM measurement was carried out by a JEOL JSM-7001 at an acceleration voltage of 15 keV.

### **2-2-4. Atomic force microscopy (AFM)**

AFM images of GNN films for the analysis of the thickness and roughness were acquired by using a Pacific nanotechnology Nano-R2.

## **2-3. Sample preparation and characterization of 2D GNNs properties**

### **2-3-1. Preparation of hydrophobic quartz and surface oxidized silicon (SiO<sub>2</sub>/Si) substrates**

Quartz plates and silicon substrates with a 300 nm thick surface oxide layer (SiO<sub>2</sub>/Si) were treated to create a hydrophobic surface to enhance the transfer yield. Substrates were immersed in a mixture of an ammonia solution (1.0 mL, 28 w/w% in water), hydrogen peroxide (1.0 mL, 30

w/w% in water), and deionized water (5 mL) at 80 °C for 20 min, rinsed with deionized water, and then dried at 150 °C for 20 min. The substrates were then transferred to a glove box, immersed in a toluene solution of chlorotrimethylsilane (80 µL TMSCl dissolved in 4.0 mL toluene) at 60 °C for 2 hours, then rinsed with toluene (4 mL × 3 times), and dried on a hot plate at 150 °C for 10 min.

### **2-3-2. GNN transfer process**

The GNN produced by 2Z-CVD was transferred from Au(111) to hydrophobic quartz (10 mm × 10 mm). The GNN/Au(111)/glass substrate was immersed in water to separate the GNN/Au(111) film from the glass. The GNN/Au(111) film was then transferred onto the surface of an aqueous gold-etchant solution (10 mL) in a well that contains KI (1.8 g) and I<sub>2</sub> (120 mg). A transfer well size of 11 mm × 22 mm was chosen based on the substrate size to ensure complete transfer. Two minutes later, after most of the gold film disappeared, the insulating substrate was attached to the floating GNN film. After 6 min (to allow complete etching of gold), the insulating substrate with the transferred GNN was withdrawn from the etchant solution; rinsed in deionized water and dried on a hot plate at 60 °C. Repeating this protocol gave multilayered GNN on the desired substrate. The transferred GNN on the substrate was treated in a UHV annealing chamber at 200 °C at < 10<sup>-6</sup> Pa for 30 min to allow effective contact between GNN layers and the substrate.

### **2-3-3. In-plane electrical conductivity measurements**

A five-layered GNN film on quartz substrate was produced by a repetitive deposition onto a hydrophobic quartz plate, as mentioned above. An Au electrode pattern (100 nm thick, 200 µm × 200 µm pad, 50 µm gap) was deposited onto the transferred GNN film through a mask (VECO 100 mesh Cu grid) by a vacuum deposition instrument.

The electrical conductivities ( $\sigma$ ) were measured by four probe and two probe methods using a Keithley 4200-SCS semiconductor characterization system at room temperature under vacuum condition (< 10<sup>-3</sup> Pa). In case of four probe method, a current source was supplied through the two outmost probes, while the voltage drop was sensed between the two inner probes. Using Ohm's

law the resistance  $R$  can be calculated by

$$R = \frac{V}{I}, \quad (2-1)$$

where  $R$  is electrical resistance,  $V$  is voltage, and  $I$  is current. Electrical conductivities of GNNs were then calculated using the following equation:

$$\sigma = \frac{1}{R} \frac{l}{wt}, \quad (2-2)$$

where the  $w$  is the electrode width,  $l$  is the electrode gap, and  $t$  is the film thickness.

#### 2-3-4. Cross-plane electrical conductance measurements

GNN produced by 2Z-CVD (40  $\mu\text{g}$  of 5-CGNR-1-1, 600  $^{\circ}\text{C}$ ) was transferred onto the hydrophobic quartz substrate with pre-deposited back-contacts (Ti 3 nm + Au 50 nm, 100  $\mu\text{m}$  Cu slot grid mesh). In order to assist the GNN adhesion to the electrodes, the substrate was treated by submersion into an octadecanethiol solution (50 mM in ethanol) for 10 seconds, followed by an ethanol wash. After transfer and UHV annealing, Au top-contacts (100 nm, 100  $\mu\text{m}$  Cu slot grid mesh) were deposited at a 90-degree angle to the bottom-contacts. Conductance measurements were performed under vacuum ( $10^{-2}$  torr) inside a four-terminal probe station using a semiconductor characterization system (4200-SCS; Keithley Instruments Inc.) at room temperature. Three different film thicknesses were used to remove any effects of additional resistance in the system. In order to calculate the conductance, a linear current sweep was used to determine the resistance  $R$  from a linear fit of Ohm's law ( $V = RI$ ). The conductivity  $\sigma$  was calculated as the inverse of the resistivity  $\rho$ , which was determined by a linear fit of the equation

$$\rho = R \frac{A}{t} = R_{\text{AN}} \frac{1}{t} \rightarrow R_{\text{AN}} = \rho t, \quad (2-3)$$

where  $A$  is the electrode area,  $t$  is the GNN film thickness and  $R_{\text{AN}}$  is the area-normalized

resistance. As both the resistance and film thickness have non-zero uncertainties, orthogonal distance regression was used to perform the linear fit.

### 2-3-5. FET device fabrication and measurements

GNN FET devices were fabricated by a one-time transfer of GNNs on Au(111)/quartz onto  $n^{++}$  doped silicon substrates (300 nm thick  $\text{SiO}_2$  gate insulator). After UHV annealing, palladium electrodes (10.0 nm thick) were patterned by using a mask (115  $\mu\text{m} \times 115 \mu\text{m}$ , 9  $\mu\text{m}$  gap, VECO 200 mesh Cu grid). An electrochemically sharpened Pt-Ir (80:20) needle was used to scratch the GNN-film around the electrodes to create isolated channels.

Transport characteristic measurements were performed under vacuum ( $10^{-2}$  torr) inside a three-terminal probe station using a semiconductor characterization system (4200-SCS; Keithley Instruments Inc.) at room temperature. The carrier mobilities were calculated using the transconductance measurement equation.<sup>3</sup>

$$\mu = \left(\frac{L}{W}\right) \frac{1}{C} \frac{1}{V_{DS}} \left(\frac{\partial I_{DS}}{\partial V_{GS}}\right), \quad (2-4)$$

where  $L$  and  $W$  stand for the length (9  $\mu\text{m}$ ) and width (115  $\mu\text{m}$ ) of the channel,  $C$  stands for the  $\text{SiO}_2$  dielectric capacitance (11.6 nF  $\text{cm}^{-1}$ ) and  $V_{DS}$ ,  $I_{DS}$  and  $V_{GS}$  stand for the drain-source voltage, drain-source current and gate-source voltage, respectively.

### 2-3-6. Thermal conductivity measurements

20, 40, and 100-layered GNN films on  $\text{SiO}_2/\text{Si}$  were produced by repetitive deposition, as mentioned above. To avoid undesirable leak current related to the Si substrate, square edges of transferred GNN were scratched off using a needle.

Cross-plane thermal conductivities of GNN film samples, consisting of the structure GNN film/300 nm-thick  $\text{SiO}_2$  film/Si substrate (4 mm  $\times$  7 mm in size and 0.55 mm in thickness), were evaluated by the  $2\omega$  method. Prior to the measurements, Au films (2 mm  $\times$  4 mm in size and 100



nm in thickness) were deposited onto the GNN film surface, after which Ag paste was glued onto both ends of the Au films to ensure electrical contact with the electrodes. During the measurement, periodic Joule heat was generated in the Au films by acoustic resistive heating (angular frequency  $\omega = 2\pi f$ ,  $f = 1000\text{--}5000$  Hz) and the temperature modulation by the thermal dissipation to Si substrates was monitored as thermo-reflectance (TR) signals of the continuous wave laser light (635 nm in wavelength;  $\approx 0.1$  mm in beam diameter).<sup>4</sup>

In this study, the thermal diffusion length  $L$  ( $\approx 0.1$  mm in Si in the given  $f$  range<sup>1</sup>) is an order of magnitude smaller than the width of the Au film (2 mm), which ensures that the heat dissipation from the Au film to the Si substrate is one-dimensional (1D). Also, the  $L$  is significantly larger than the total thickness of the films, but smaller than Si substrate thickness, which ensures that the acoustic 1D temperature wave reaches the Si substrate within a period but is not reflected at the backside of the Si substrate. In this case, the in-phase amplitude of the TR signal from any of our samples responds linearly to  $(2\omega)^{-0.5}$ , with a slope  $m$  and an offset  $n$ . Here we model the sample structure by a three-layer system, (Layer 1: Au film, Layer 2: GNN film, and Layer 3: Si substrate) with their two interfaces; the SiO<sub>2</sub> film as a part of the interface between GNN films and Si substrates. The thermal resistance between the Au film and Si substrate  $R$  is calculated by solving the 1D heat equation of the three-layer system which is expressed by the following equations.

$$R = R_2 + R_{\text{int}} = \frac{d_2}{\kappa_2} + R_{\text{int}} = \frac{c_1 d_1 + c_2 d_2}{c_3 \kappa_3} - \frac{d_1}{2\kappa_1} + \frac{n}{m} \frac{1}{\sqrt{2c_3 \kappa_3}} \quad (2-5)$$

$$R_{\text{int}} = R_{12} + R_{23}$$

Here,  $R_i$  is the thermal resistance of film  $i$  [ $\text{m}^2 \text{K W}^{-1}$ ],  $R_{ij}$  is the thermal resistance at the interface between  $i$  and  $j$  [ $\text{m}^2 \text{K W}^{-1}$ ],  $d_i$  is the film thickness of film  $i$  [m],  $\kappa_i$  is the thermal conductivity of film  $i$  [ $\text{W m}^{-1} \text{K}^{-1}$ ], and  $c_i$  is the heat capacity per volume of film  $i$  [ $\text{J m}^{-3} \text{K}^{-1}$ ]. The indices ( $i, j$ ) of each parameters refer to the layer numbers, respectively. The following parameters were used for our analysis:  $c_1 = 2.47 \times 10^6$  [ $\text{J m}^{-3} \text{K}^{-1}$ ],  $\kappa_1 = 178$  [ $\text{W m}^{-1} \text{K}^{-1}$ ], and  $d_1 = 1.00 \times 10^{-7}$  [m] for Au film;  $c_2 = 1.60 \times 10^6$  [ $\text{J m}^{-3} \text{K}^{-1}$ ] for GNN film;  $c_3 = 1.66 \times 10^6$  [ $\text{J m}^{-3} \text{K}^{-1}$ ] and  $\kappa_3 = 148$  [ $\text{W m}^{-1} \text{K}^{-1}$ ] for Si substrate. Since equation (2-5) is a linear function of the GNN film thickness  $d_2$ , the thermal conductivity of the GNN film  $\kappa_2$ , and the sum of interface thermal resistances  $R_{\text{int}}$ , it can be

used to evaluate the thermal resistance  $R$  with respect to the GNN film thickness  $d_2$ .

## 2-4. Calculations

Calculations were performed using the Materials Studio software suite (BIOVIA Inc.). Geometry optimization of biradical form of precursor DBOP was performed as follows:

Adsorption conformations of precursor DBOP biradicals on Au(111) calculated by quantum mechanics/molecular mechanics (QM/MM) approach were performed according to our previous publication.<sup>5</sup> Quantum mechanics/molecular mechanics (QM/MM) with the QMERA module were used to calculate the optimized geometries of the biradical forms of  $R_{uu}$ ,  $R_{ud}$  and  $R_{dd}$  adsorbed on Au(111). The input structures were generated by the modification of optimized structures of DBSP.<sup>5</sup> The QM/MM calculations can treat organic molecule radicals on metal surface with electronic interaction at the QM level, the exterior metal surface treated at the MM level. The unit cell was expanded by the insertion of MM level metal surface in order to avoid intermolecular interactions. In this work, the precursor biradicals on Au(111) showed the lowest  $C_1$  symmetry; thus, a small periodic unit cell with high symmetry cannot be constructed. Optimized conformations and the corresponding formation energies can be obtained by employing the QM/MM approach.

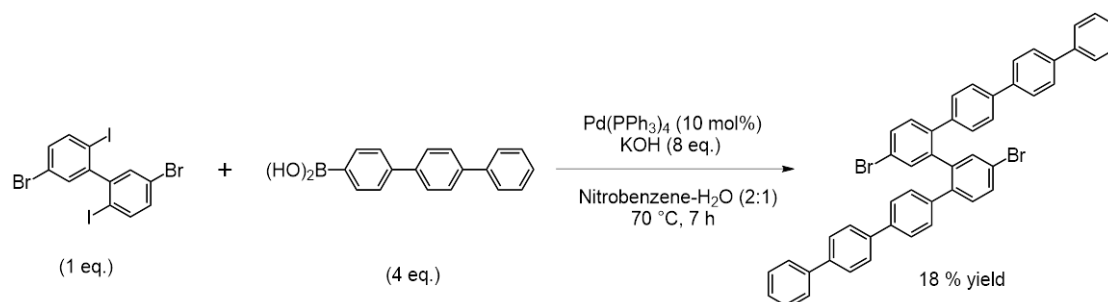
A unit cell ( $46.14 \times 39.96 \times 51.19 \text{ \AA}$ ) with three-layered Au(111) was used to minimize intermolecular interactions. Input geometries of the conformers  $R_{uu}$ ,  $R_{ud}$  and  $R_{dd}$  and the underneath two Au layers (154 atoms) were treated at the QM level. At the same time, the other Au atoms (614 atoms) were treated at the MM level. The QMERA module was used to perform QM/MM calculations on the periodic system. Spin-unrestricted DFT calculations were carried out with the DMol<sup>3</sup> program<sup>6,7</sup> using the generalized gradient approximation (GGA) of the Perdew-Burke-Ernzerhof (PBE) functional as the electron exchange and correlation functional<sup>8</sup> in combination with the DND basis set (ver. 4.4) and effective core potential for Au. For the MM region, the GULP program was employed with the ReaxFF 6.0 force field. QM/MM interactions were handled by mechanical embedding. In the QMERA implementation, the QM and MM interfaces were handled by ChemShell.<sup>9</sup>

## 2-5. Synthetic procedures

5,5'-Dibromo-2,2'-diiodo-1,1'-biphenyl<sup>10</sup> and [1,1':4,1''-terphenyl]-4-ylboronic acid<sup>11</sup> was prepared according to the literature. A mixture of 3,9- and 3,10-dibromperylene (DBP),<sup>12</sup> 10,10'-dibromo-9,9'-bianthryl (DBBA),<sup>12</sup> and 4-bromo-1-iodo-2-nitrobenzene **1**<sup>13</sup> were reported in the literature.

### 2-5-1. Synthesis of 'Z-bar-linkage' precursors with different branch length.

#### 4'''',5''''-dibromo-1,1':4',1'':4'',1''':2''',1''':2''''',1''''':4''''',1''''':4''''''',1''''''':-octiphenyl (DBOP): (1)



Firstly, [1,1':4,1''-terphenyl]-4-ylboronic acid (194.5 mg, 0.7095 mmol, 4 equiv.) and KOH (79.6 mg, 1.4187 mmol, 8 equiv.) were added into a solution of 5,5'-dibromo-2,2'-diiodo-1,1'-biphenyl (100 mg, 0.1774 mmol, 1 equiv.) in nitrobenzene (10 mL) and H<sub>2</sub>O (5 mL). Secondly, Pd(PPh<sub>3</sub>)<sub>4</sub> (20.49 mg, 0.01774 mmol, 0.1 equiv.) was added into the solution after degassing. Thirdly, the mixture was heated to 70 °C for 7 h under N<sub>2</sub> atmosphere. After cooling to room temperature, the reaction mixture was diluted with chloroform, and the organic layer was collected, washed with brine (50 mL), dried with Na<sub>2</sub>SO<sub>4</sub>, and concentrated in vacuo. Then, the catalyst was removed by passing through a short silica gel pad. Finally, the resulting solid was purified by GPC and recrystallized using toluene affording the title compound (24.5 mg, 18%) as a white powder. <sup>1</sup>H NMR (600 MHz, 20 °C, CDCl<sub>3</sub>) δ 7.71 (d, *J* = 1.98 Hz, 2H), 7.67 (d, *J* = 8.28, 4H), 7.63 (d, *J* = 6.78 Hz, 8H), 7.52 (dd, *J* = 2.04, 7.8 Hz, 2H), 7.46 (t, *J* = 7.56 Hz, 4H), 7.36 (t, *J* = 7.02 Hz, 2H), 7.28 (d, *J* = 8.16 Hz, 4H), 7.05 (d, *J* = 8.22 Hz, 2H), 6.56 (d, *J*

= 8.16 Hz, 4H);  $^{13}\text{C}$  NMR (150 MHz, 20 °C,  $\text{CDCl}_3$ )  $\delta$  140.71, 140.65, 140.35, 139.63, 139.60, 138.73, 138.51, 134.13, 131.58, 131.30, 129.41, 128.92, 127.65, 127.49, 127.34, 127.12, 126.31, 121.46. Figure 2-1 shows NMR spectra.

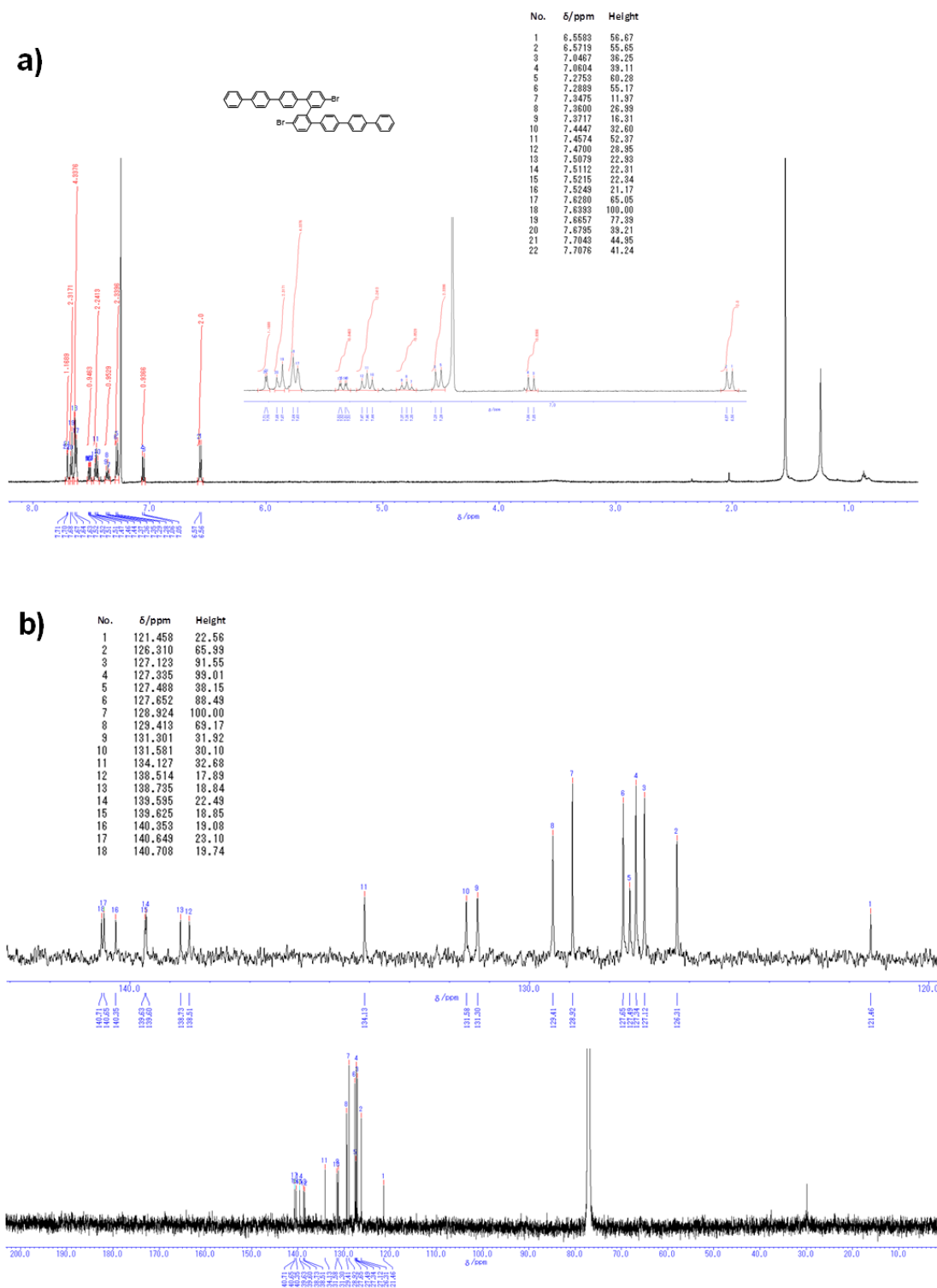
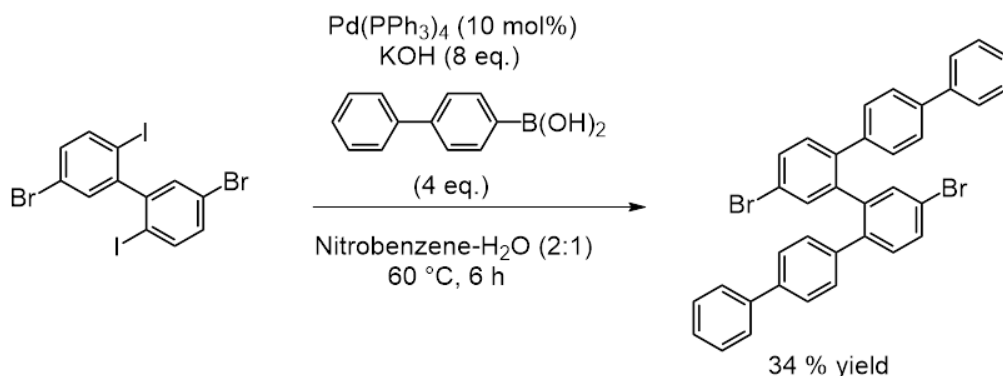


**Figure 2-1.** NMR spectra of DBOP in  $\text{CDCl}_3$ . a,  $^1\text{H}$  NMR; b,  $^{13}\text{C}$  NMR.

**4'',5'''-dibromo-1,1':4',1'':2'',1''':2''',1''':4''',1''''-sexiphenyl (DBSP): (2)**



First, [1,1'-biphenyl]-4-ylboronic acid (280 mg, 1.41 mmol, 4 equiv) and KOH (160 mg, 2.85 mmol, 8 equiv) were added to a solution of 5,5'-dibromo-2,2'-diiodo-1,1'-biphenyl (200 mg, 0.35 mmol, 1 equiv) in nitrobenzene (20 mL) and H<sub>2</sub>O (10 mL). Freeze-pump-thaw degassing was repeated for three times in order to remove the oxygen in the mixture. Second, Pd(PPh<sub>3</sub>)<sub>4</sub> (41.0 mg, 35 μmol, 0.1 equiv) was added to the solution after degassing. Third, the mixture was heated to 60 °C for 6 h under N<sub>2</sub> atmosphere. The reaction was monitored by thin-layer chromatography (TLC). After the completion of the reaction, the biphasic mixture was diluted with chloroform. Then, the organic layer was collected, washed with brine (100 mL), passed through a short silica gel pad, and then concentrated in vacuo. Finally, the mixture was purified by GPC and recrystallized using hexane. The title compound was obtained in 37.0 mg (34% yield). <sup>1</sup>H NMR (600 MHz, 20 °C, CDCl<sub>3</sub>) δ 7.54 (d, *J* = 6.82 Hz, 4H), 7.50 (d, *J* = 8.24 Hz, 2H), 7.43 (dd, *J* = 7.38, 7.38 Hz, 4H), 7.34 (t, *J* = 6.91 Hz, 2H), 7.21 (d, *J* = 8.06 Hz, 4H), 7.03 (d, *J* = 8.11 Hz, 2H), 6.54 (d, *J* = 8.03 Hz, 4H); <sup>13</sup>C NMR (125 MHz, 20 °C, CDCl<sub>3</sub>) δ 140.65, 140.53, 139.52, 139.17, 138.29, 134.00, 131.45, 131.15, 129.22, 128.79, 127.32, 126.90, 126.32, 121.30. Figure 2-2 shows NMR spectra. The insets in the Figure 2-2 (a) and (b) show the magnified aromatic region in the NMR spectra.

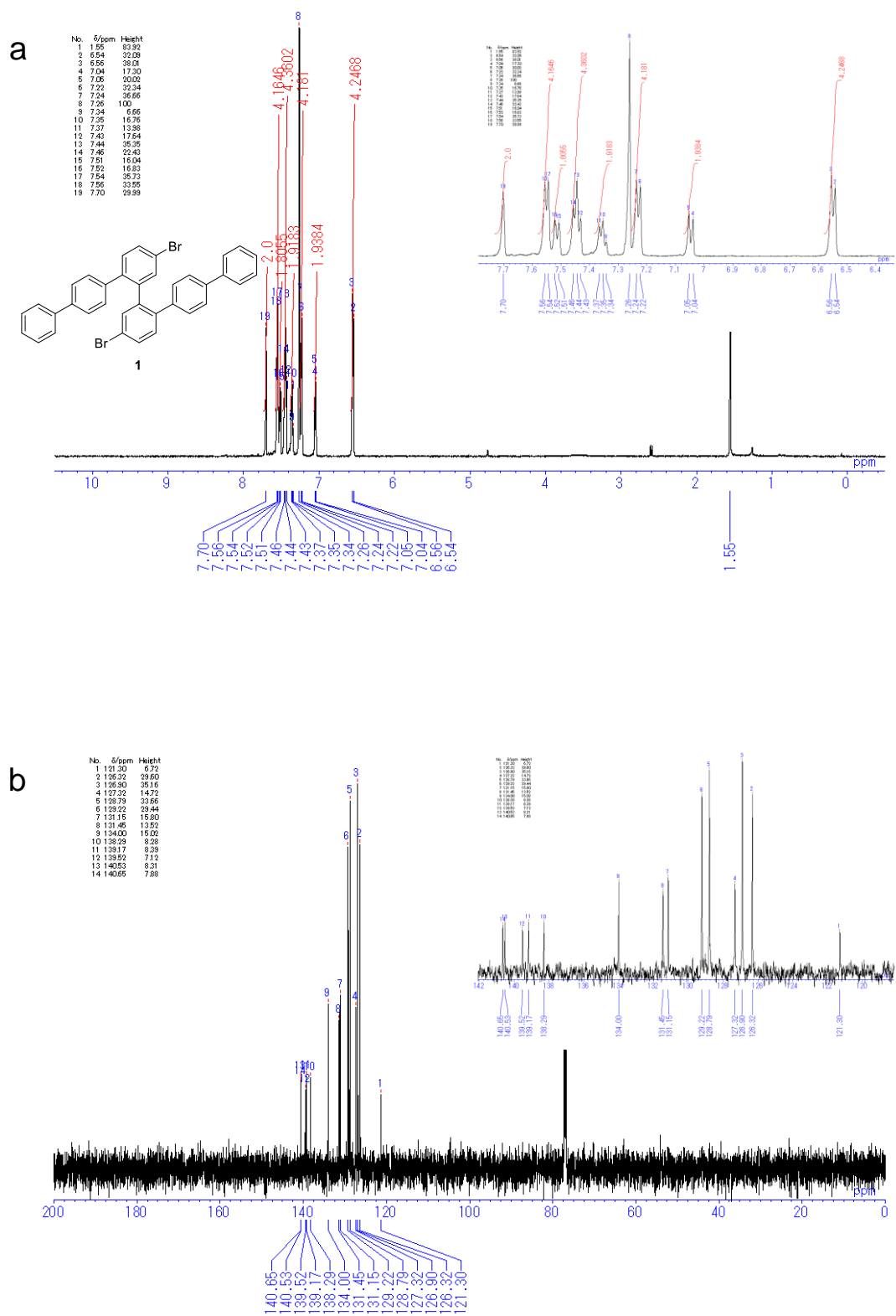
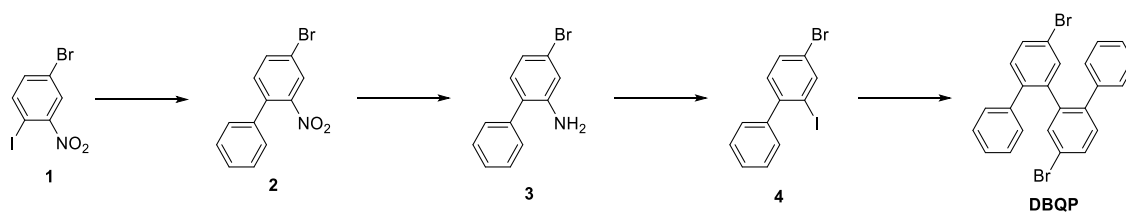


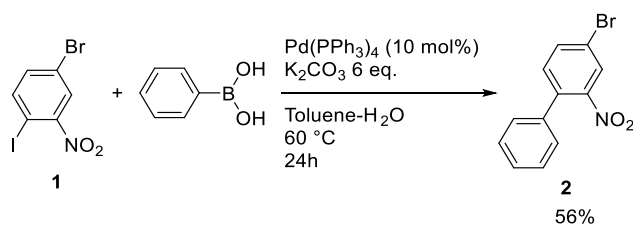
**Figure 2-2.** NMR spectra of DBSP in  $\text{CDCl}_3$ . a,  $^1\text{H}$  NMR; b,  $^{13}\text{C}$  NMR.

### 4',5''-dibromo-1,1':2',1'':2'',1'''-quaterphenyl (DBQP): (3)



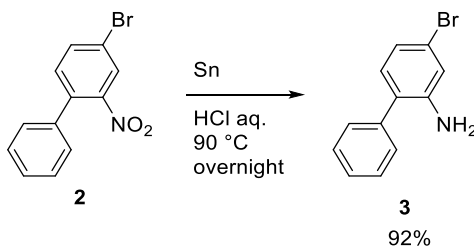
Scheme 2-1. Synthetic route of 4',5''-dibromo-1,1':2',1'':2'',1'''-quaterphenyl (DBQP) (3).

### Preparation of 4-bromo-2-nitro-1,1'-biphenyl 2



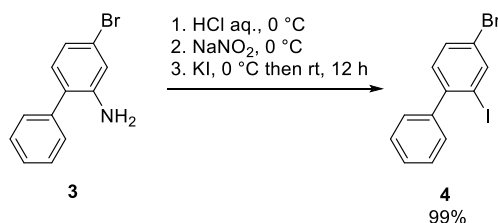
Phenylboronic acid (1.86 g, 15.24 mmol, 2 equiv) and  $K_2CO_3$  (6.32 g, 45.7 mmol, 6 equiv) were added to a solution of 4-bromo-1-iodo-2-nitrobenzene (**1**, 2.5 g, 7.62 mmol, 1 equiv) in toluene (7.5 mL) and  $H_2O$  (3.75 mL).  $Pd(PPh_3)_4$  (0.88 g, 0.76 mmol, 0.1 equiv) was added to the solution after degassing. The mixture was heated to 60 °C for 24 hours under  $N_2$  atmosphere. The product was extracted with toluene and dried over  $Na_2SO_4$ . After concentration in vacuo, silica gel flash chromatography (eluent, 100:1 hexane / ethyl acetate) gave the titled compound (1.2 g, 56% yield).  $^1H$  NMR (300 MHz, 20 °C,  $CDCl_3$ )  $\delta$  8.00 (d, 1H,  $J = 2.04$  Hz), 7.76 (d, 1H,  $J = 10.17$  Hz), 7.43-7.41 (m, 3H), 7.34-7.27 (m, 3H).

### Preparation of 4-bromo-2-phenylaniline 3



To solution of 4-bromo-2-nitro-1,1'-biphenyl (**2**, 1 g, 3.60 mmol) in 13.6 mL of ethanol was added concentrated HCl (6.8 mL). Tin powder (0.8542 g, 7.20 mmol) was then added, and the reaction mixture was heated at 90 °C overnight. After cooling, the mixture was poured into ice water (32 mL) and then made alkaline with aqueous NaOH solution (pH 14.0). The precipitate was collected by filtration and dried under vacuum. Alumina flash short chromatography (hexane:DCM = 1:1 + trimethylamine 1%) gave the titled compound (0.82 g, 92% yield). <sup>1</sup>H NMR (300 MHz, 20 °C, CDCl<sub>3</sub>) δ 7.47-7.32 (m, 2H), 7.03-6.97 (m, 1H), 7.40-7.43 (m, 3H), 4.48 (br, 2H).

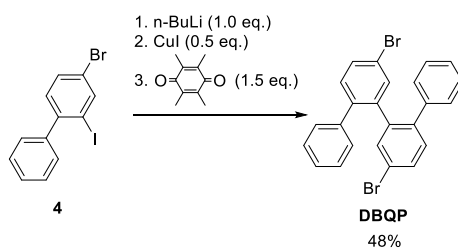
#### Preparation of 4-bromo-2-iodo-1,1'-biphenyl **4**



To a suspension of **3** (0.5 g, 2.0 mmol) in concentrated HCl (0.4 mL) cooled at 0 °C was added carefully an aqueous solution of sodium nitrite (0.167 g, 2.4 mmol) in 5 min. The brown mixture was then stirred at 0 °C for 45 min and added carefully to an aqueous solution for potassium iodide (0.67 g, 4.0 mmol) in 5 min. The final solution was stirred at room temperature for 12 h and then quenched with saturated sodium sulfite. The product was extracted with diethyl ether and washed with 1M HCl aq., brine, and water, then dried with sodium sulfate. Bulb-to-bulb distillation gave the titled compound (0.71 g, 99% yield). <sup>1</sup>H NMR (300 MHz, 20 °C, CDCl<sub>3</sub>) δ 8.09 (d, 1H, *J* = 1.98 Hz), 7.51 (dd, 1H, *J* = 8.1, 1.95 Hz), 7.43-7.40 (m, 3H), 7.31-7.28 (m, 2H), 7.16 (d, 1H, *J* = 8.13 Hz).

#### Preparation of 4',5''-dibromo-1,1':2',1'':2'',1'''-quaterphenyl (DBQP)





To a solution of 4-bromo-2-iodo-1,1'-biphenyl (**4**, 0.42 g, 1.17 mmol) in THF (11 mL) was added *n*-BuLi (0.75 mL, 1.17 mmol, 1.6 M in hexane) at  $-78\text{ }^{\circ}\text{C}$ . The mixture was stirred for 30 min under the same temperature, and CuI (0.11 g, 0.58 mmol) was added under nitrogen flow, and duroquinone (0.29 g, 1.74 mmol) was added after another 40 min. The mixture was stirred for 3 h at room temperature. The mixture was diluted with  $\text{CH}_2\text{Cl}_2$  and water. The water layer was extracted by  $\text{CH}_2\text{Cl}_2$ . The crude material was obtained by concentration of combined organic layer, and purified by flash silica chromatography (hexane:ethyl acetate = 100:1). The titled compound was obtained (0.24 g, 48% yield).  $^1\text{H}$  NMR (300 MHz,  $20\text{ }^{\circ}\text{C}$ ,  $\text{CDCl}_3$ )  $\delta$  7.62 (d, 2H,  $J = 2.13$  Hz), 7.49 (dd, 2H,  $J = 8.22, 2.13$  Hz), 7.12-7.07 (m, 2H), 7.00-6.95 (m, 6H), 6.45-6.48 (m, 4H);  $^{13}\text{C}$  NMR (75 MHz,  $\text{CDCl}_3$ )  $\delta$  140.53 (2C), 140.02 (2C), 139.32 (2C), 133.93 (2C), 131.59 (2C), 131.02 (2C), 128.89 (4C), 127.65 (4C), 126.42 (2C), 121.07 (2C); Anal. calcd for  $\text{C}_{24}\text{H}_{16}\text{Br}_2$ : C, 62.10; H, 3.47; N, 0.00. Found C, 61.88; H, 3.61; N, 0.00. Figure 2-3 and Figure 2-4 show the NMR spectra.

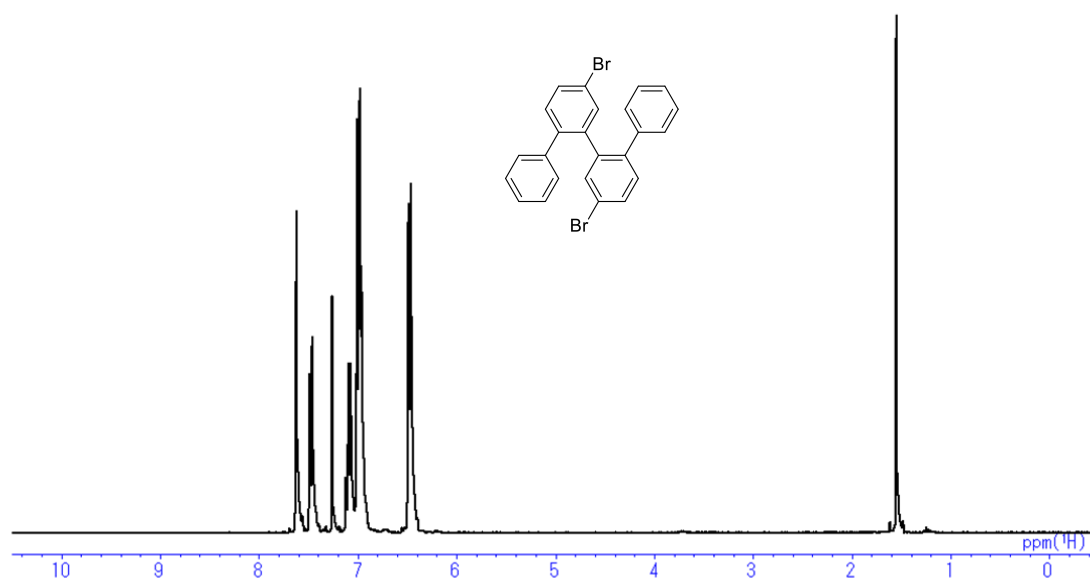


**Figure 2-3.**  $^1\text{H}$  NMR (300 MHz) spectra of DBQP in  $\text{CDCl}_3$ .

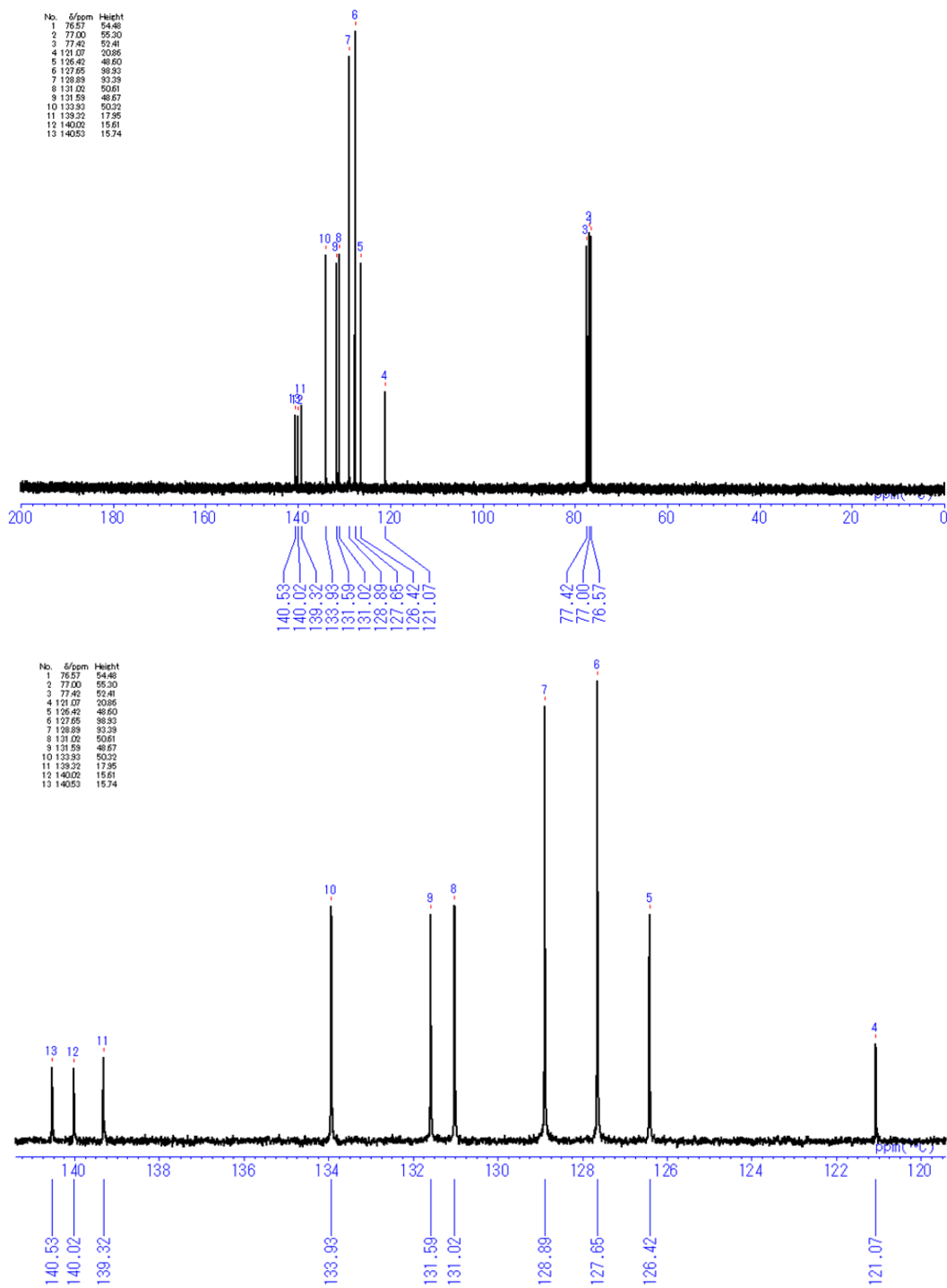
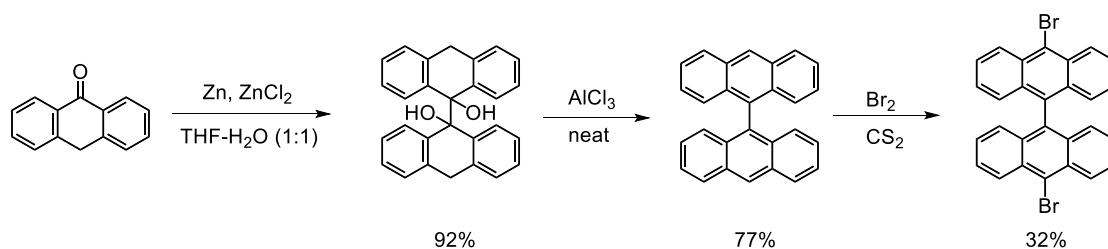


**Figure 2-4.**  $^{13}\text{C}$  NMR (75 MHz) spectra of DBQP in  $\text{CDCl}_3$ .

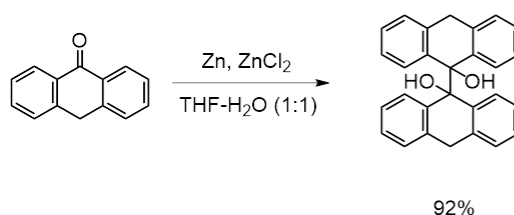
### 2-5-2. Synthesis of precursors for armchair GNRs.

#### 10,10'-dibromo-9,9'-bianthracene (DBBA): (4)



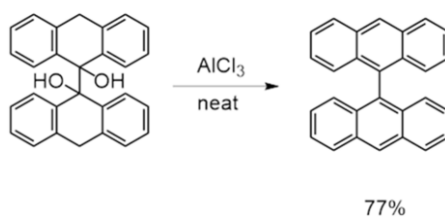
**Scheme 2-2.** Synthetic route of 10,10'-dibromo-9,9'-bianthracene (DBBA) (4).

### Preparation of 9,9'-10,10'-tetrahydro-[9,9'-bianthracene]-9,9'-diol



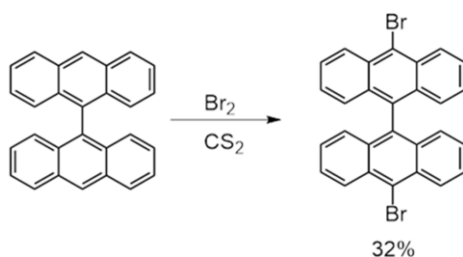
THF (6.0 mL) and deionized water (6.0 mL) were added to a mixture of anthrone (1.00 g, 5.15 mmol), ZnCl<sub>2</sub> (1.1 g, 8.07 mmol) and Zn powder (5.0 g, 76.5 mmol) with flushed nitrogen. The reaction mixture was stirred at room temperature. After 3 hour, the diluted HCl aqueous solution (3.0 M, 5 mL) was added and stirred overnight. The crude material was passed through a short silica gel pad (hexane:dichloromethane; 1:1 as eluent). A white solid was obtained (924 mg, 2.37 mmol, 92% yield) and directly used in the next step without further purification.

### Preparation of 9,9'-bianthracene



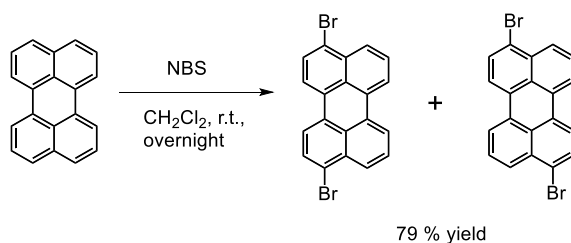
9,9'-10,10'-tetrahydro-[9,9'-bianthracene]-9,9'-diol (514 mg, 1.32 mmol) and AlCl<sub>3</sub> (6.0 g, 45.0 mmol) were agitated in a nitrogen-filled glove bag. The mixture was added to diluted H<sub>2</sub>SO<sub>4</sub> aqueous solution (1.0 M, 50 mL). The organic layer was extracted using dichloromethane. Crude material was purified by precipitation from carbon disulfide and methanol (357.8 mg, 1.01 mmol, 77% yield). <sup>1</sup>H NMR spectra of the products were identical to those reported in the literature.<sup>14</sup>

### Synthesis of 10,10'-dibromo-9,9'-bianthracene



A carbon disulfide solution (7.5 mL) of bromine (0.1 mL, 1.9 mmol) was added dropwise to the same solution (17.5 mL) of 9,9'-bianthracene (300 mg, 0.848 mmol). The mixture was stirred overnight at room temperature. The residual bromine was decomposed by washing aqueous solution of sodium sulfite. Crude material was purified using silica gel column chromatography (hexane:dichloromethane 1:1 as eluent) and precipitation from carbon disulfide and methanol (140.0 mg, 0.276 mmol, 32% yield).  $^1\text{H}$  NMR spectra of the products were identical to those reported in the literature.<sup>15</sup>

#### Dibromoperylene (3,9- and 3,10-mixture) (DBP): (5)



Dichloromethane solution (50 mL) of *N*-bromosuccinimide (0.14 g, 0.79 mmol) was added dropwise to the dichloromethane solution (50.0 mL) of perylene (100 mg, 0.396 mmol) in a nitrogen atmosphere. The resulting reaction mixture was stirred overnight at room temperature. The reaction mixture was washed with diluted HCl aqueous solution (1 M). Recrystallization from toluene gave analytically pure product (128.0 mg, 0.312 mmol, 79% yield).  $^1\text{H}$  NMR spectra of the product were identical to those reported in the literature.<sup>16</sup> The shares of 3,9- and 3,10-isomers were determined to be 47% and 53%, respectively, from  $^1\text{H}$  NMR data.

## 2-6. References

1. H. Sakaguchi, H. Matsumura, H. Gong, and A. M. Abouelwafa, *Science*, **2005**, 310 (5750), 1002-1006.
2. Q. Li, G. Cao, S. Okamoto, J. Yi, W. Lin, B. C. Sales, J. Yan, R. Arita, J. Kuneš, and A. V. Kozhevnikov, *Sci. Rep.*, **2013**, 3, 3073.
3. S. J. Kang, C. Kocabas, T. Ozel, M. Shim, N. Pimparkar, M. A. Alam, S. V. Rotkin, and J. A. Rogers, *Nat. Nanotechnol.*, **2007**, 2 (4), 230-236.
4. Y. Nakamura, M. Isogawa, T. Ueda, S. Yamasaka, H. Matsui, J. Kikkawa, S. Ikeuchi, T. Oyake, T. Hori, and J. Shiomi, *Nano Energy*, **2015**, 12, 845-851.
5. H. Sakaguchi, S. Song, T. Kojima, and T. Nakae, *Nat. Chem.*, **2017**, 9 (1), 57-63.
6. B. Delley, *J. Chem. Phys.*, **1990**, 92 (1), 508-517.
7. B. Delley, *J. Chem. Phys.*, **2000**, 113 (18), 7756-7764.
8. J. P. Perdew, K. Burke, and M. Ernzerhof, *Phys. Rev. Lett.*, **1996**, 77 (18), 3865.
9. P. Sherwood, A. H. de Vries, M. F. Guest, G. Schreckenbach, C. R. A. Catlow, S. A. French, A. A. Sokol, S. T. Bromley, W. Thiel, and A. J. Turner, *Theochem-J. Mol. Struct.*, **2003**, 632 (1), 1-28.
10. K. L. Chan, S. E. Watkins, C. S. Mak, M. J. McKiernan, C. R. Towns, S. I. Pascu, and A. B. Holmes, *Chem. Commun.*, **2005** (46), 5766-5768.
11. I. Yamaguchi, K. Goto, and M. Sato, *Macromolecules*, **2009**, 42 (20), 7836-7845.
12. H. Sakaguchi, Y. Kawagoe, Y. Hirano, T. Iruka, M. Yano, and T. Nakae, *Adv. Mater.*, **2014**, 26 (24), 4134-4138.
13. A. K. Flatt, Y. Yao, F. Maya, and J. M. Tour, *J. Org. Chem.*, **2004**, 69 (5), 1752-1755.
14. B. Han, P. Ma, X. Cong, H. Chen, and X. Zeng, *J. Am. Chem. Soc.*, **2019**, 141 (22), 9018-9026.
15. J. Cai, P. Ruffieux, R. Jaafar, M. Bieri, T. Braun, S. Blankenburg, M. Muoth, A. P. Seitsonen, M. Saleh, and X. Feng, *Nature*, **2010**, 466 (7305), 470-473.
16. P. Schlichting, U. Rohr, and K. Müllen, *Liebigs Ann.-Recl.*, **1997**, 1997 (2), 395-407.

## Chapter 3

### On-surface synthesis of graphene clusters from a Z-bar-linkage precursor with quaterphenyl branches

#### 3-1. Introduction

Graphene nanoribbons (GNRs), narrow strips of graphene, are made of an  $sp^2$ -hybridized carbon atom backbone and can display various edge structures.<sup>1</sup> GNRs show adjustable electronic and optical properties which can be tuned by tailoring the width<sup>2-5</sup> and edge structures,<sup>6-10</sup> or by doping with heteroatoms.<sup>11-15</sup> These properties make GNRs promising as functional components in electronic and optoelectronic devices.<sup>16-19</sup> As a result, bottom-up fabrication of GNRs has focused on achieving precise control over the width, edge structures, and chemical composition. In this respect, metal-surface-assisted synthesis has proven to be an effective approach to fabricate atomically well-defined GNRs.<sup>20-26</sup>

Although extensive studies have been carried out on the surface-assisted synthesis of GNRs, steering the on-surface reactions toward desired products is still a subject that needs to be addressed. The reaction pathways and underlying mechanisms for the growth of GNRs rely on the combination of the selected precursor and substrate.<sup>27-33</sup> However, the geometric effects of the precursor on the GNR structure are not well understood. Recently, we reported a novel conformation-controlled catalysis involved in the growth of acene-type GNRs on Au(111) via two-zone chemical vapor deposition (2Z-CVD).<sup>24</sup> The biradical form of the terphenyl-branched 'Z-bar-linkage' precursor adopts a chiral conformation with height asymmetry when deposited onto the Au(111) surface. The chiral conformations of the precursors form homochiral polymers that can be converted into densely packed acene-type GNRs via efficient dehydrogenation reactions.<sup>24</sup> However, the effects of the branch length of the Z-bar-linkage precursor on the conformations on Au(111) have remained unknown.

Here, the length of the Z-bar-linkage precursor branch is changed by replacing the terphenyl with quaterphenyl (4''',5''''-dibromo-1,1':4',1'':4'',1''':2'',1''''; 2''''',1''''':4''''',1''''':4''''',1''''''-octiphenyl, DBOP) in order to examine the adsorption conformations on Au(111), which influence the final products of the on-surface synthesis using 2Z-CVD. We found that the quaterphenyl-branched

precursors favor height-symmetric conformations on Au(111), preventing polymerization and leading to intramolecular-fused debrominated precursors. Subsequent annealing led to the formation of graphene clusters via intermolecular dehydrogenation instead of acene-type GNRs.

## 3-2. Results and discussion

### 3-2-1. Structural studies on the products of 2Z-CVD

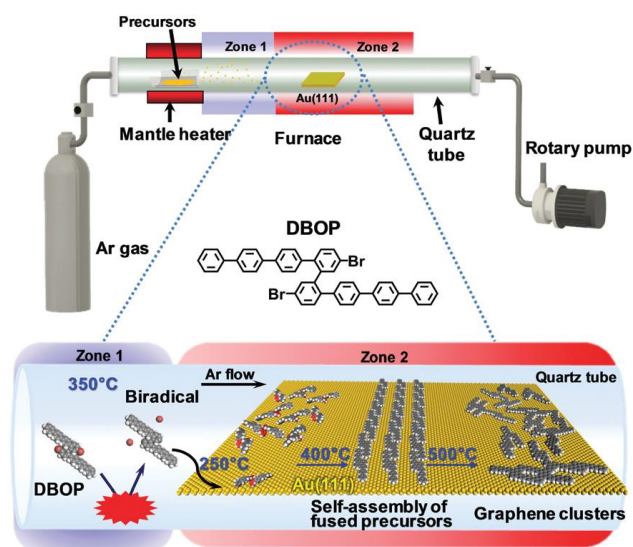


**Figure 3-1.** Schematic illustration depicting the growth of graphene clusters from DBOP by 2Z-CVD. The red benzene rings of the precursors in the space-filling models point toward the Au(111) surface.

The previously developed 2Z-CVD was employed for the on-surface synthesis.<sup>22</sup> As depicted in Figure 3-1, the system was evacuated using a rotary pump under argon (Ar) flow. 2Z-CVD is advantageous because it permits independent temperature control of two separate zones 1 and 2, and does not require ultra-high vacuum conditions. The generation of a high density of radicals has been hypothesized to occur in zone 1 by the collision of precursors with the hot wall. The polymerization of the precursor biradicals supplied to the Au(111) substrate has been assumed to occur in zone 2, and when annealed at higher temperature affords GNRs via dehydrogenation. This technique has successfully been used to fabricate a series of armchair-edged GNRs in high yield.<sup>22</sup> In this study, the DBOP precursor was synthesized. DBOP was sublimated at 350 °C so

that it could be supplied to the Au(111) substrate in zone 2, which was held at 250 °C, by passing through zone 1 (350 °C). The sample was subsequently annealed stepwise to higher temperatures of 400, 450, and 500 °C.

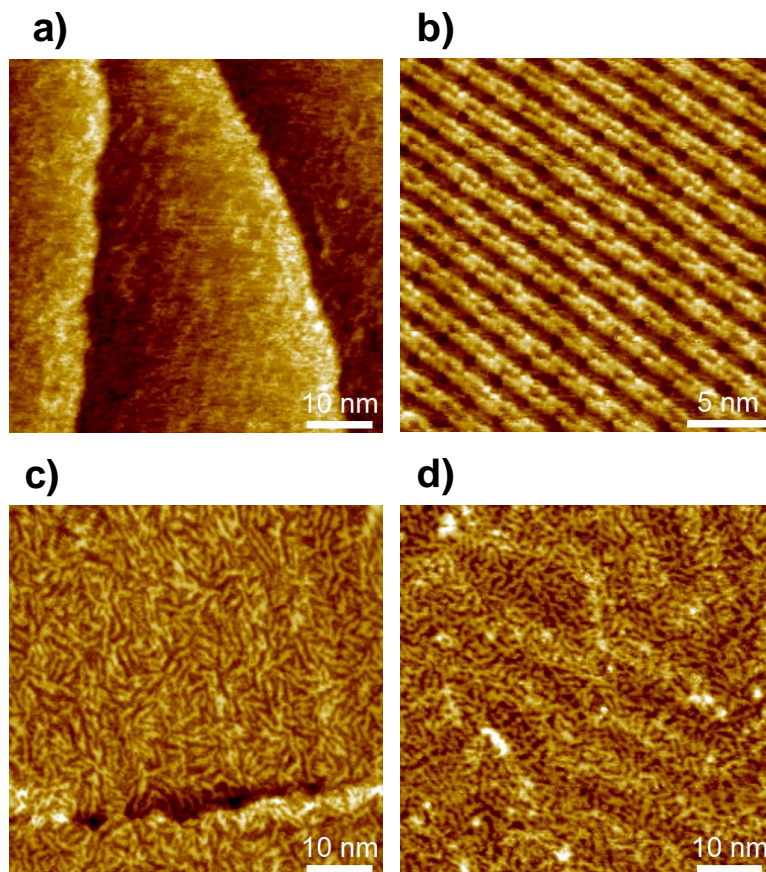
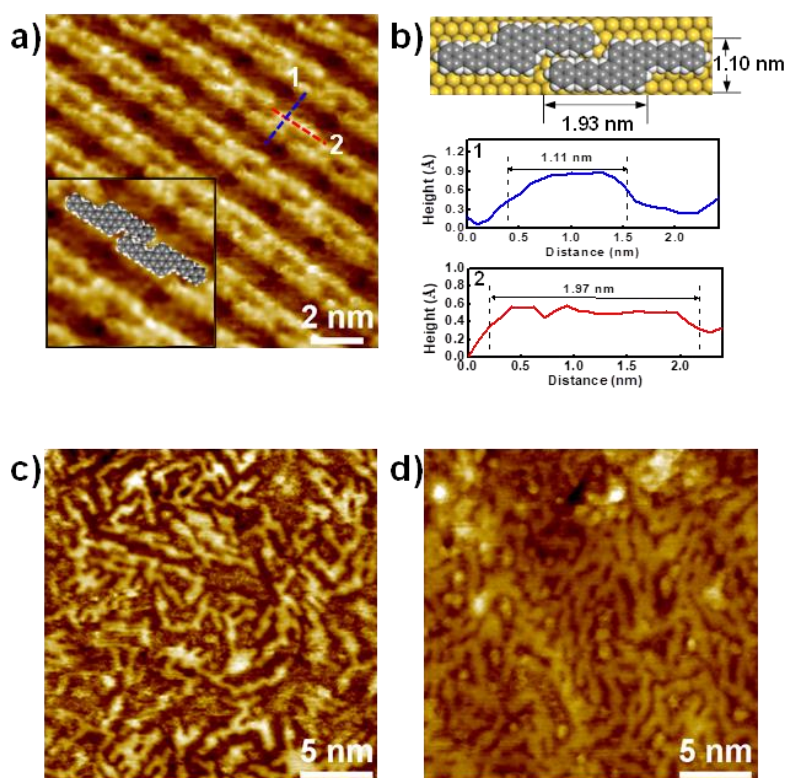


**Figure 3-2.** Large scale STM images of 2Z-CVD grown samples from 20  $\mu\text{g}$  of the precursor DBOP at 250 °C (a), 400 °C (b), 450 °C (c), and 500 °C (d).

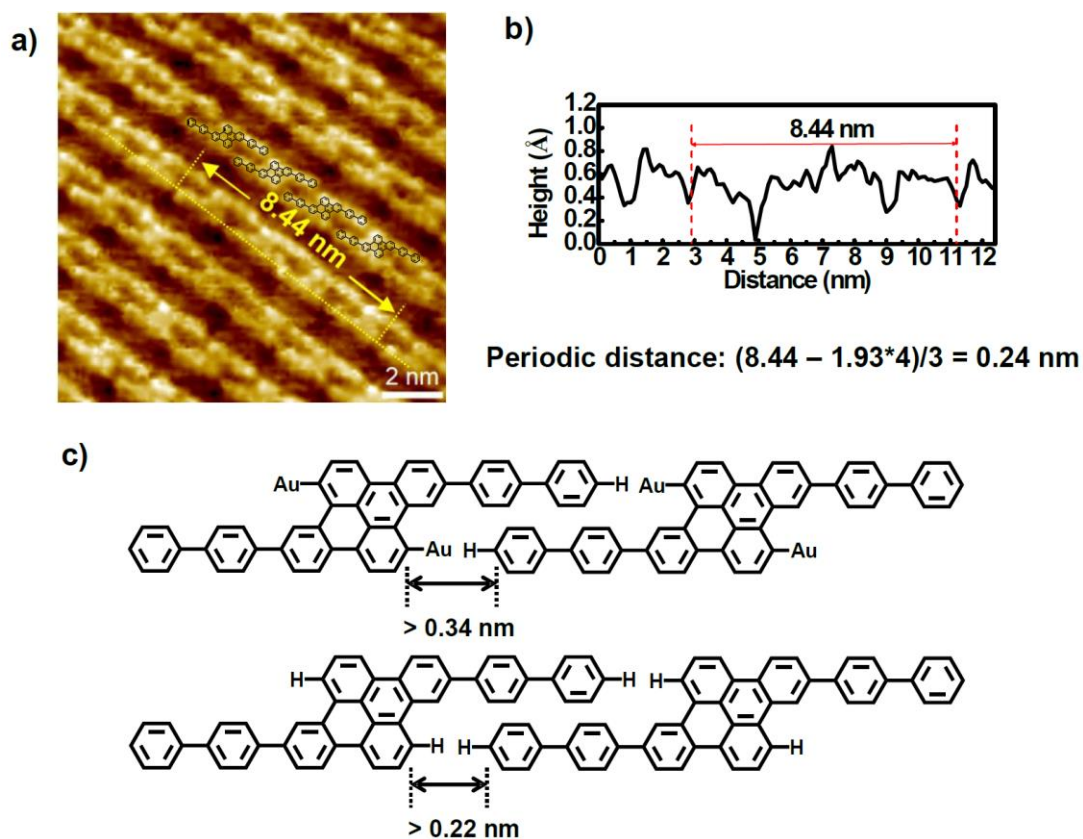
STM characterization of the samples was performed at room temperature under an Ar atmosphere. As shown in Figure 3-2a, disordered structures were observed at 250 °C. Upon annealing at 400 °C, well-ordered linear arrays of ‘S-shaped’ units were formed (Figure 3-2b and Figure 3-3a). Cross-sectional analysis of the individual S-shaped units revealed a central width of 1.11 nm and an arm length of 1.97 nm, which are in good agreement with the model (1.10 nm and 1.93 nm, respectively), assuming an intramolecular-fused, debrominated precursormolecule (Figure 3-3b). The periodic distance between two adjacent quaterphenyl branches along the chain direction is 0.24 nm (Figure 3-4), smaller than the theoretically predicted spacing (0.34 nm) with C–Au bond formation (Figure 3-4), assuming a C–Au bond length of 0.24 nm.<sup>34</sup> This result



indicates no C–Au bond formation between debrominated DBOP molecules. This result also suggests that intramolecular dehydrogenation took place and flattened the conformation to an S-shape (Figure 3-2b and Figure 3-3a). The S-shaped molecules were self-assembled to form linear array structures. Further annealing the sample at 450 °C led to branched chain structures, suggesting that intermolecular dehydrogenation occurred with multiple cross-coupling modes between individual S-shaped molecules (Figure 3-2c and Figure 3-3c). The above reactions, intramolecular fusion and the following intermolecular C–C bond formation, provide a promising way to fabricate new low-dimensional carbon architectures without using halogen atoms by activating C–H bonds. Similar intermolecular C–C coupling was also observed for the quaterphenyl molecule on Cu(110) by activating meta C–H bonds of the terminal benzene.<sup>35,36</sup> Further annealing at 500 °C enhanced the interchain-connected carbon nanostructures (Figure 3-2d and Figure 3-3d).

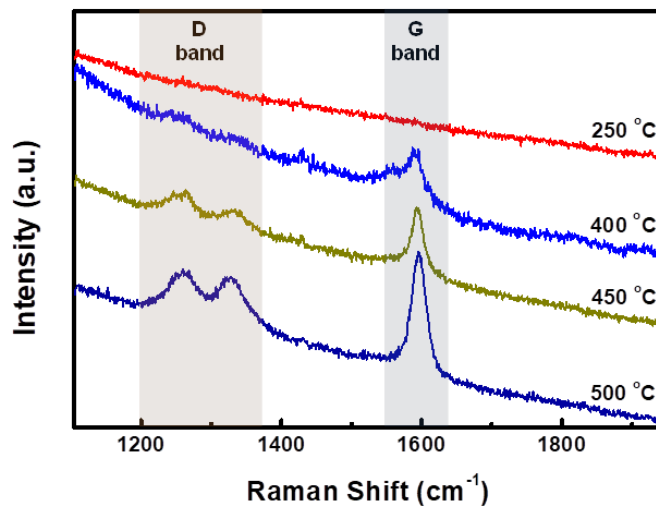


**Figure 3-3.** (a, c, d) STM images of samples annealed at 400 °C (a, the inset shows a magnified image with an overlaid model), 450 °C (c) and 500 °C (d). All samples were first grown by 2Z-CVD with a supply of 20 μg of DBOP precursor. (b) Space-filling model and cross-sectional analysis along the dotted lines in (a).



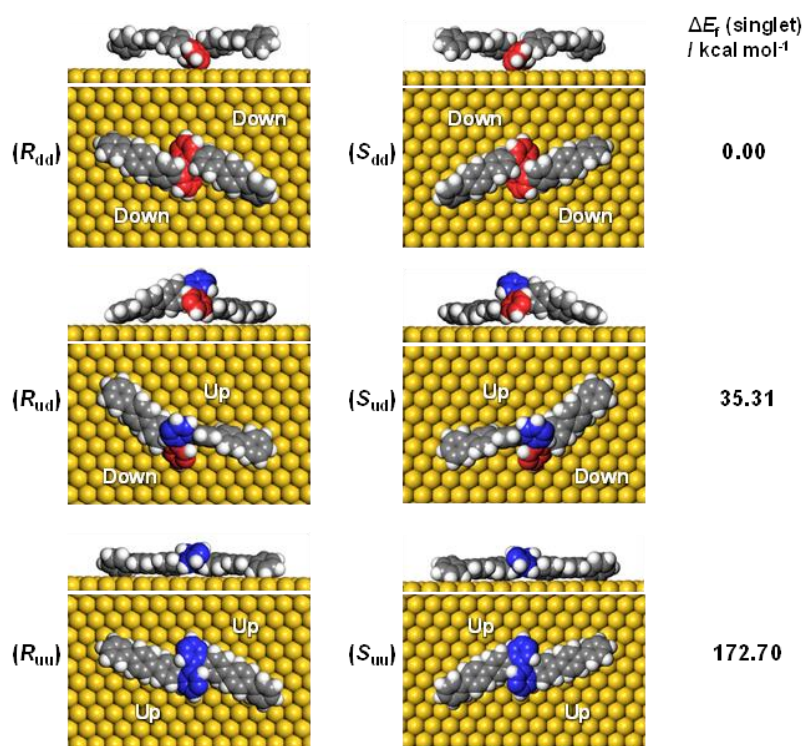
**Figure 3-4.** (a) STM image of sample annealed at 400 °C with overlaid chemical structures, (b) cross-sectional analysis along the dotted line in (a), (c) illustration of theoretical periodic distances with and without metal-organic bonds formation.

Raman spectra of 2Z-CVD-grown samples measured at different temperatures show two significant points (Figure 3-5). Firstly, the sample at 250 °C did not show a detectable Raman signature probably due to the small Raman scattering cross-section for debrominated DBOP precursors of polyphenylene structures.<sup>24</sup> As the temperature was increased from 250 to 400 °C, a peak at  $1594 \text{ cm}^{-1}$  (G band) appeared. This could be due to the p-conjugation effects from intramolecular dehydrogenation and is in line with the STM results. Secondly, when increasing the temperature from 400 to 450 °C, the intensity of the D bands at  $1333 \text{ cm}^{-1}$  and  $1259 \text{ cm}^{-1}$  was remarkably enhanced. A further increase in the temperature to 500 °C showed a similar Raman signature as the 450 °C annealed sample.



**Figure 3-5.** Raman spectra of 2Z-CVD-grown samples from DBOP annealed at different temperatures.

### 3-2-2. Adsorption conformations of the precursor

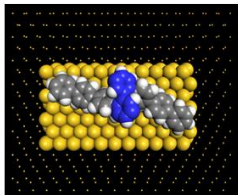
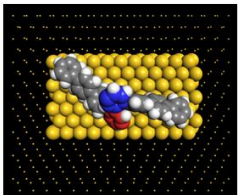
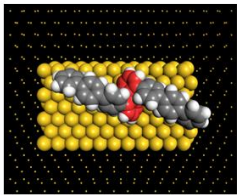
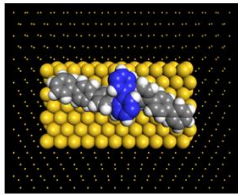
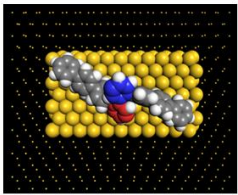
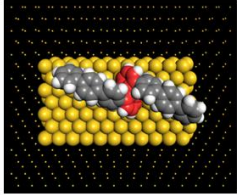


**Figure 3-6.** Optimized conformations of biradical forms of the precursor DBOP on Au(111) with the corresponding formation energies ( $\Delta E_f$ ) in the singlet state by the QM/MM approach. Colors of the benzene indicate the relative heights from the Au(111) surface; red, pointing toward the surface; blue, away from the surface.

In order to unravel the underlying mechanisms of the inhibited polymerization, conformations of the DBOP biradicals on Au(111) were computed by the quantum mechanics/molecular mechanics (QM/MM) approach according to our previous publication.<sup>24</sup> Initial geometries of the DBOP biradicals on Au(111) were generated by the modification of previous results of optimized biradical geometries of 4,5-dibromo-1,1'-4,1''-2'',1''':2''',1''':4''',1''''-sexiphenyl (DBSP) at the QM/MM level.<sup>24</sup> The predicted conformations are parameterized by surface chirality and height asymmetry, as shown in Figure 3-6. Here, surface chirality indicates the right (*R*)- or left (*S*)-handedness of the enantiomers for the molecules on a 2D surface, and height asymmetry indicates the relative height from Au(111) surface of the two radical-carbons in the centered biphenyl core. We considered height-symmetrical conformations (denoted as 'dd' for 'down-down' and 'uu' for 'up-up') which represent the two radical-carbons directed either toward or away from the surface. A height-asymmetrical conformation (denoted as 'ud' for 'up-down') represents two radical-carbons positioned at different heights from the surface. Because the *R* and *S* conformers should show the same energy, we focus only on the *R* conformer in the calculation process. The calculation results (Figure 3-6 and Table 3-1) indicate the height-symmetrical  $R_{dd}$  conformer to have the lowest formation energy in the singlet state. Its formation energy is 35.31 kcal mol<sup>-1</sup> lower than that of the height-asymmetrical  $R_{ud}$  conformer, and 172.70 kcal mol<sup>-1</sup> lower than that of the  $R_{uu}$  conformer. Thereby, the  $R_{dd}$  conformer was considered to be the dominant species as it is stabilized by such a remarkable energy difference. Contrasting greatly with DBOP, the previously reported DBSP showed the most energetically stable conformer to be  $R_{ud}$ .<sup>24</sup> This is because  $R_{ud}$  of the DBSP showed a linear structure of two terphenyl branches, whereas  $R_{dd}$  showed a remarkably distorted 'double-arch' structure of two terphenyl branches. In the present case, the radical–Au(111) interaction and the resulting molecular distortion are presumed to play a key role in the determination of the total energy. The two radical-carbons in the DBOP's  $R_{dd}$  conformer strongly bind to Au(111). The longer branch-length of the quaterphenyl in DBOP might alleviate the torsion in the branches, while strong torsion takes place in the shorter branch of the terphenyl in DBSP. The strong radical–Au(111) interaction of DBOP, with decreased torsion of the branches in  $R_{dd}$ , might be the reason for the lowest formation energy. Thus, the conformation differences between DBOP and DBSP on Au(111) might originate from a balance between the radical–Au(111)

interactions and the molecular torsion.

**Table 3-1.** Formation energy of conformers of the biradical form of DBOP on Au(111) at the optimized geometry calculated by QM/MM approach. Colors of the benzene rings in the space-filling models of the precursor indicate the relative heights from the Au(111) surface; red, pointing toward the surface; blue, away from the surface.

Geometry	$(R_{uu})$	$(R_{ud})$	$(R_{dd})$
$\Delta E_f(\text{singlet})$ (Kcal/mol)	 172.70	 35.31	 0.00
$\Delta E_f(\text{triplet})$ (Kcal/mol)	 172.70	 36.91	 0.62

As outlined above, altering the arm length of the Z-bar-linkage precursor resulted in a completely different reaction pathway compared with that of DBSP.<sup>24</sup> Thus, a precursor biradical adsorption conformation dependent reaction pathway was concluded, and is shown in Scheme 3-1. In the case of DBSP, the precursor biradicals adopt favorable chiral  $R_{ud}$  and  $S_{ud}$  conformations with height asymmetry on Au(111), and form homochiral polymers. Annealing the polymers at higher temperatures leads to stepwise dehydrogenation, and finally, acene-GNRs are formed at 500 °C via complete dehydrogenation. However, DBOP displays a vastly different pathway than DBSP, as the DBOP biradicals favor height-symmetric chiral  $R_{dd}$  and  $S_{dd}$  conformations on Au(111). Neither of these two kinds of conformers (Figure 3-6) can polymerize due to strong radical–Au(111) interactions, which results in steric hindrance (Figure 3-7) during the lifetime of the radicals. Annealing the sample at 400 °C leads to self-assembled arrays of intramolecular-fused debrominated precursors. Further annealing at 450 and 500 °C results in intermolecular connected graphene clusters.



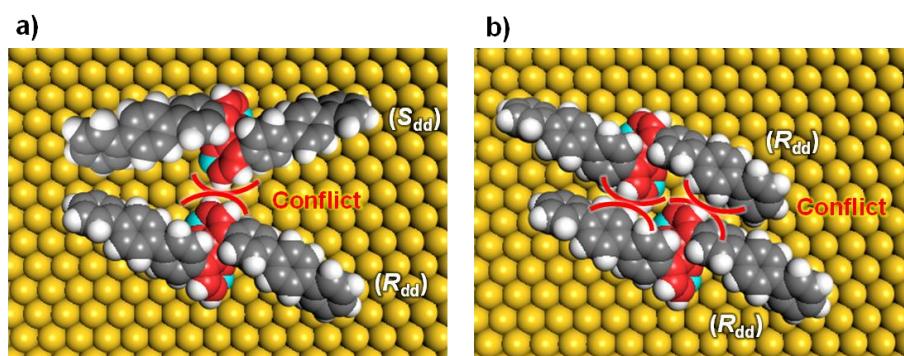
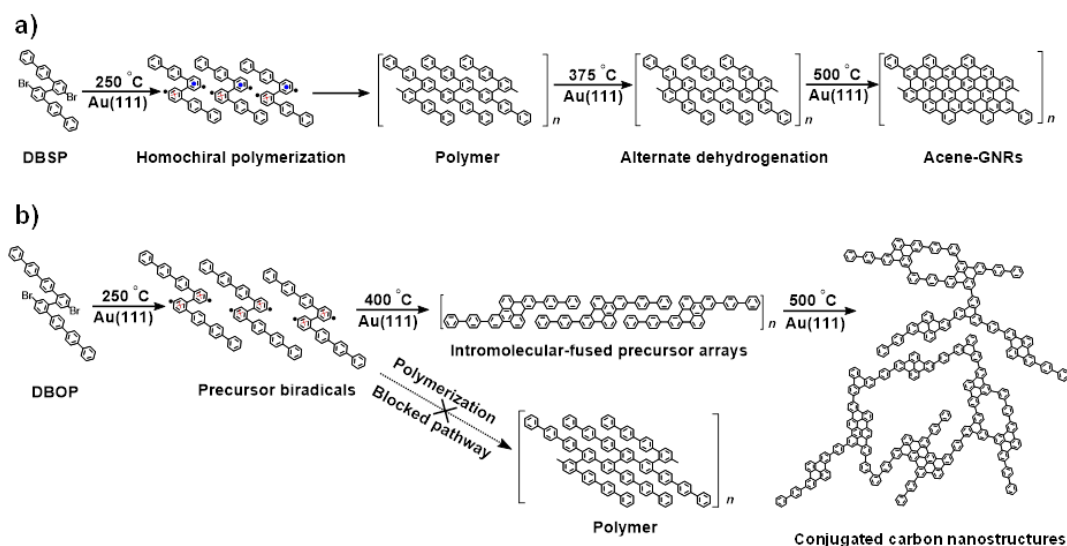


**Figure 3-7.** Top view of the hindrance effect of the bimolecular reactions between heterochiral (a) and homochiral (b) precursors. The red benzene rings of the precursor in the space-filling models point toward the Au(111) surface, the radical-carbon is denoted by a light blue color.



**Scheme 3-1.** Comparison of two different reaction pathways of Z-bar-linkage precursors DBSP (a) and DBOP (b) via 2Z-CVD. Blue dots (red cross) in the chemical structures indicate the benzene rings pointing away (toward) the Au(111) surface. The black dots represent the radicals.

### 3-3. Conclusions

In this study, the products formed on Au(111) from the Z-barlinkage precursor DBOP via 2Z-CVD were examined. The results were compared with an analogue precursor DBSP under similar CVD conditions. The previously reported DBSP showed the formation of homochiral polymers at 250 °C, which converted into densely packed acene-type GNRs at 500 °C through

stepwise dehydrogenation. In great contrast with DBSP, DBOP shows a different reaction pathway. The polymerization of the DBOP biradicals is hindered, subsequently leading to self-assembled arrays of intramolecular-fused debrominated precursors at 400 °C, and forming graphene clusters at 450 and 500 °C. Theoretical calculations revealed that the DBOP biradicals favored the  $R_{dd}$  and  $S_{dd}$  conformations with height symmetry on Au(111). The inhibited polymerization of DBOP biradicals might result from the steric hindrance caused by strong radical–Au(111) interactions. This conformation effect can be especially useful for the rational design of precursors for surface-assisted synthesis of carbon-based materials.

### 3-4. Reference

1. L. Chen, Y. Hernandez, X. Feng, and K. Müllen, *Angew. Chem. Int. Ed.*, **2012**, 51 (31), 7640-7654.
2. M. Ezawa, *Phys. Rev. B*, **2006**, 73 (4), 045432.
3. Y.-W. Son, M. L. Cohen, and S. G. Louie, *Phys. Rev. Lett.*, **2006**, 97 (21), 216803.
4. H. Huang, D. Wei, J. Sun, S. L. Wong, Y. P. Feng, A. C. Neto, and A. T. S. Wee, *Sci. Rep.*, **2012**, 2, 983.
5. D. Prezzi, D. Varsano, A. Ruini, A. Marini, and E. Molinari, *Phys. Rev. B*, **2008**, 77 (4), 041404.
6. S. Okada, *Phys. Rev. B*, **2008**, 77 (4), 041408.
7. T. Wassmann, A. P. Seitsonen, A. M. Saitta, M. Lazzeri, and F. Mauri, *Phys. Rev. Lett.*, **2008**, 101 (9), 096402.
8. P. Wagner, C. P. Ewels, J.-J. Adjizian, L. Magaud, P. Pochet, S. Roche, A. Lopez-Bezanilla, V. V. Ivanovskaya, A. Yaya, and M. Rayson, *J. Phys. Chem. C*, **2013**, 117 (50), 26790-26796.
9. G. D. Nguyen, H.-Z. Tsai, A. A. Omrani, T. Marangoni, M. Wu, D. J. Rizzo, G. F. Rodgers, R. R. Cloke, R. A. Durr, and Y. Sakai, *Nat. Nanotechnol.*, **2017**, 12 (11), 1077-1082.
10. E. Carbonell-Sanromà, J. Hieulle, M. Vilas-Varela, P. Brandimarte, M. Iraola, A. Barragán, J. Li, M. Abadia, M. Corso, D. Sánchez-Portal, D. Peñã, and J. I. Pascual, *ACS Nano*, **2017**, 11 (7), 7355-7361.
11. C. Bronner, S. Stremlau, M. Gille, F. Brauße, A. Haase, S. Hecht, and P. Tegeder, *Angew. Chem. Int. Ed.*, **2013**, 52 (16), 4422-4425.

12. R. R. Cloke, T. Marangoni, G. D. Nguyen, T. Joshi, D. J. Rizzo, C. Bronner, T. Cao, S. G. Louie, M. F. Crommie, and F. R. Fischer, *J. Am. Chem. Soc.*, **2015**, 137 (28), 8872-8875.
13. S. Kawai, S. Saito, S. Osumi, S. Yamaguchi, A. S. Foster, P. Spijker, and E. Meyer, *Nat. Commun.*, **2015**, 6, 1-6.
14. J. Cai, C. A. Pignedoli, L. Talirz, P. Ruffieux, H. Söde, L. Liang, V. Meunier, R. Berger, R. Li, and X. Feng, *Nat. Nanotechnol.*, **2014**, 9 (11), 896-900.
15. G. D. Nguyen, F. M. Toma, T. Cao, Z. Pedramrazi, C. Chen, D. J. Rizzo, T. Joshi, C. Bronner, Y.-C. Chen, and M. Favaro, *J. Phys. Chem. C*, **2016**, 120 (5), 2684-2687.
16. Z. Chen, H. I. Wang, J. Teyssandier, K. S. Mali, T. Dumslaff, I. Ivanov, W. Zhang, P. Ruffieux, R. Fasel, and H. J. Räder, *J. Am. Chem. Soc.*, **2017**, 139 (10), 3635-3638.
17. J. P. Llinas, A. Fairbrother, G. B. Barin, W. Shi, K. Lee, S. Wu, B. Y. Choi, R. Braganza, J. Lear, and N. Kau, *Nat. Commun.*, **2017**, 8 (1), 633.
18. T. J. Sisto, Y. Zhong, B. Zhang, M. T. Trinh, K. Miyata, X. Zhong, X.-Y. Zhu, M. L. Steigerwald, F. Ng, and C. Nuckolls, *J. Am. Chem. Soc.*, **2017**, 139 (16), 5648-5651.
19. Z. Chen, W. Zhang, C.-A. Palma, A. Lodi Rizzini, B. Liu, A. Abbas, N. Richter, L. Martini, X.-Y. Wang, and N. Cavani, *J. Am. Chem. Soc.*, **2016**, 138 (47), 15488-15496.
20. L. Talirz, P. Ruffieux, and R. Fasel, *Adv. Mater.*, **2016**, 28 (29), 6222-6231.
21. Y. Segawa, H. Ito, and K. Itami, *Nat. Rev. Mater.*, **2016**, 1, 15002.
22. H. Sakaguchi, Y. Kawagoe, Y. Hirano, T. Iruka, M. Yano, and T. Nakae, *Adv. Mater.*, **2014**, 26 (24), 4134-4138.
23. T. Kojima, Y. Bao, C. Zhang, S. Liu, H. Xu, T. Nakae, K. P. Loh, and H. Sakaguchi, *Langmuir*, **2017**, 33 (40), 10439-10445.
24. H. Sakaguchi, S. Song, T. Kojima, and T. Nakae, *Nat. Chem.*, **2017**, 9 (1), 57-63.
25. S. Song, G. Huang, T. Kojima, T. Nakae, H. Uno, and H. Sakaguchi, *Chem. Lett.*, **2017**, 46 (10), 1525-1527.
26. S. Song, T. Kojima, T. Nakae, and H. Sakaguchi, *Chem. Commun.*, **2017**, 53 (52), 7034-7036.
27. J. Cai, P. Ruffieux, R. Jaafar, M. Bieri, T. Braun, S. Blankenburg, M. Muoth, A. P. Seitsonen, M. Saleh, and X. Feng, *Nature*, **2010**, 466 (7305), 470-473.
28. P. Han, K. Akagi, F. Federici Canova, H. Mutoh, S. Shiraki, K. Iwaya, P. S. Weiss, N. Asao, and T. Hitosugi, *ACS Nano*, **2014**, 8 (9), 9181-9187.



29. P. Han, K. Akagi, F. Federici Canova, R. Shimizu, H. Oguchi, S. Shiraki, P. S. Weiss, N. Asao, and T. Hitosugi, *ACS Nano*, **2015**, 9 (12), 12035-12044.
30. D. G. de Oteyza, A. García-Lekue, M. Vilas-Varela, N. s. Merino-Díez, E. Carbonell-Sanromà, M. Corso, G. Vasseur, C. Rogero, E. Guitián, and J. I. Pascual, *ACS Nano*, **2016**, 10 (9), 9000-9008.
31. P. H. Jacobse, A. van den Hoogenband, M. E. Moret, R. J. Klein Gebbink, and I. Swart, *Angew. Chem. Int. Ed.*, **2016**, 55 (42), 13052-13055.
32. F. Schulz, P. H. Jacobse, F. F. Canova, J. van der Lit, D. Z. Gao, A. van den Hoogenband, P. Han, R. J. Klein Gebbink, M.-E. Moret, and P. M. Joensuu, *J. Phys. Chem. C*, **2017**, 121 (5), 2896-2904.
33. K. A. Simonov, N. A. Vinogradov, A. S. Vinogradov, A. V. Generalov, E. M. Zagrebina, G. I. Svirskiy, A. A. Cafolla, T. Carpy, J. P. Cunniffe, and T. Taketsugu, *ACS Nano*, **2015**, 9 (9), 8997-9011.
34. J. I. Urgel, H. Hayashi, M. Di Giovannantonio, C. A. Pignedoli, S. Mishra, O. Deniz, M. Yamashita, T. Dienel, P. Ruffieux, and H. Yamada, *J. Am. Chem. Soc.*, **2017**, 139 (34), 11658-11661.
35. Q. Sun, C. Zhang, H. Kong, Q. Tan, and W. Xu, *Chem. Commun.*, **2014**, 50 (80), 11825-11828.
36. C. Zhang, Q. Sun, H. Chen, Q. Tan, and W. Xu, *Chem. Commun.*, **2015**, 51 (3), 495-498.

## Chapter 4

### Bottom-up on-surface synthesis of two-dimensional graphene nanoribbon networks and their thermoelectric properties

#### 4-1. Introduction

The organic polymer with the backbone of extended conjugated  $\pi$ -bond exhibit semiconducting behaviour and can be used as an active material in many optoelectronic devices, but not successfully replacing the traditional inorganic materials.<sup>1,2</sup> This is due to the fact that the conjugated polymers are 1D chains in which the ordered domains are not connected by a complete inter penetrating network of bridging chains, so the efficiency of charge carrier transport is hampered as they hop between chains and across disordered chain fragments.<sup>3</sup> Thus, extending conjugated  $\pi$ -bond from 1D to 2D offers a reasonable solution to increase carrier mobility as already demonstrated by the extremely high carrier mobility of graphene. However, its potential application in electronics/optoelectronics is limited due to the absence of band-gap. Hence, it is assumed that the development of 2D material with precise band gap can successfully overcome limitation of graphene. To this end, efforts are under way to synthesize 2D conjugated polymers with well-defined band gaps while maintaining the features of graphene. Even though there are many theoretical reports on the properties of 2D conjugated polymers,<sup>4,5</sup> experimental design, synthesis and characterization of such a fully  $\pi$ -conjugated materials are very scarce.<sup>6</sup> Due to the insolubility of rigid and planar 2D conjugated polymers, the classical solution polymerization and characterization techniques are not likely to be suitable. The other option is to design of properly functionalized monomers that can react in two independent directions without any steric hindrance, and identifying a suitable template to guide the formation of a continuous 2D network. Initially, topological polymerization of self-assembled molecular networks of diacetylene monomers on graphite leads to 1D polymers.<sup>7</sup> Here, the 1D polydiacetylene lines are held together laterally by non-conjugated linkages. Particularly, we report the electro-oxidative epitaxial 1D polymerization of thiophene units on iodine-covered gold surfaces.<sup>8</sup> Grill et al. have successfully synthesized 2D conjugated networks of poly(tetrakisphenyleneporphyrin) on the surface of gold crystal.<sup>9</sup> However, fully  $\pi$ -conjugated 2D structures attract much attention, since they can provide conducting carbon-based nanostructures with holey structures highly suitable for various electronic

applications. Utilization of large fully  $\pi$ -conjugated building blocks such as GNRs, which are 1D carbon-based nanowires, is becoming a promising approach to produce extended 2D pconjugated systems via surface assisted lateral fusion of GNR chains.<sup>10,11</sup> On-surface bottom-up approaches using chemically designed precursors are regarded as a promising method to produce GNRs with defined edges and widths.<sup>12</sup> Further, lateral fusion of parallelly aligned GNR led to generation of 2D graphene nanoribbon networks (GNNs).<sup>10,11</sup> However, it is difficult to efficiently create such sophisticated GNR-linkage structures, since their formation is based on a stochastic surface reaction that requires close proximity between the precursors on the surface.

Thermoelectric (TE) technology can efficiently transform small quantities of low-temperature and dispersed waste thermal energies into usable electrical energy in a sustainable manner, expected to play an important role in the world's future energy demands.<sup>13</sup> Additionally, it can able to work in tandem with other technologies, especially in photovoltaics, where a large amount of heat is generated by solar radiation that can be used by TE.<sup>14</sup> Thus, a great deal of efforts have been devoted to develop suitable and efficient thermoelectric materials. The efficiency of TE materials is mainly judged by the dimensionless Figure of merit,  $ZT=S^2\sigma T/\kappa$ , where  $S$  is the Seebeck coefficient,  $\sigma$  is the electrical conductivity,  $T$  is the absolute temperature and  $\kappa = \kappa_{el} + \kappa_{ph}$  is the thermal conductance consisting of electron and phonon contributions.<sup>15</sup> The material with high thermopower ( $S^2\sigma$ ) and a lower thermal conductivity ( $\kappa$ ) is highly suitable for TE applications. Experimental and theoretical studies revealed that the Seebeck coefficient in graphene can reach the values that is comparable with the values obtained for the semiconducting materials by decreasing the carrier density.<sup>16-18</sup> Although graphene-based materials exhibit high carrier mobility and Seebeck coefficient, graphene is not suitable for TE applications owing to its very high thermal conductivity.<sup>19</sup> On the other hand, the utilization of GNRs as a TE material has theoretically been investigated and found that GNRs are superior than the graphene itself in terms of drastically reduced thermal conductivity.<sup>20</sup> Earlier studies on GNRs revealed that the  $S^2\sigma$  value of semiconducting armchair GNRs is higher than the graphene, due to the presence of the band gap in GNRs.<sup>21</sup> When compared to the armchair, the maximum achievable  $ZT$  of pristine GNRs is lower, due to the higher thermal conductance in pristine conformation. To reduce the thermal conductivity and to improve the  $ZT$  value further, there have been many theoretical investigations carried out with different analytical strategies on the GNRs: Antidot lattices,<sup>22</sup> edge disorders,<sup>23</sup>

edge passivation,<sup>24</sup> mechanical strain,<sup>25</sup> nanopore GNRs,<sup>26</sup> etc. Particularly, Chang et al. proposed a strategy of introducing periodic arrays of nanopores<sup>27</sup> on the GNRs, and found that the maximum achievable ZT is 2 at room temperature when the device length was 1.2 mm.<sup>28</sup> Hossain et al. have predicted that the GNRs with pores show higher ZT value than the GNRs without pores, when the dimension was same in both the cases.<sup>29</sup> Cao et al. have theoretically shown that the GNRs with 2D features enhances the ZT value considerably.<sup>30</sup> The above mentioned strategies and the ZT values of GNRs are only based on theoretical evaluations and there is no report regarding the experimental validation.

In this report, we have successfully demonstrated on-surface fabrication of a cove-type 2D GNNs with holes, which can be generated by interchain reactions between self-assembled GNRs building blocks on the surface of Au(111) in 2Z-CVD at elevated temperatures as graphically represented in Figure 4-1. The GNRs was also synthesized by the same 2Z-CVD method at lower temperatures using the precursors shown in Figure 4-2. Further, it can be applied to the TE devices and found that ultra-low thermal conductivity of  $0.11 \text{ W m}^{-1} \text{ K}^{-1}$ , which is one of the lowest value among the carbon-based materials as well as inorganic semiconductors.

## **4-2. Results and discussion**

### **4-2-1. Fabrication of 1D GNRs and 2D GNNs**

The precursors used for the synthesis of 2D GNN are shown in Figure 4-2. On-surface GNRs synthesis was performed by 2Z-CVD under a rotary pump induced vacuum with an Ar flow. The Au(111) substrate was placed in zone 2 of a dual-furnace quartz tube and the precursor was sublimated onto the substrate by passing through zone 1 as shown in Figure 4-3. Independent temperature control of these two separate zones afforded GNRs in high yield without the use of UHV conditions. The advantages of 2Z-CVD include the ability to produce “concentrated radicals” on the metal surface, leading to the formation of high-density, parallelly aligned polymer chains resulting in self-assembled GNRs.

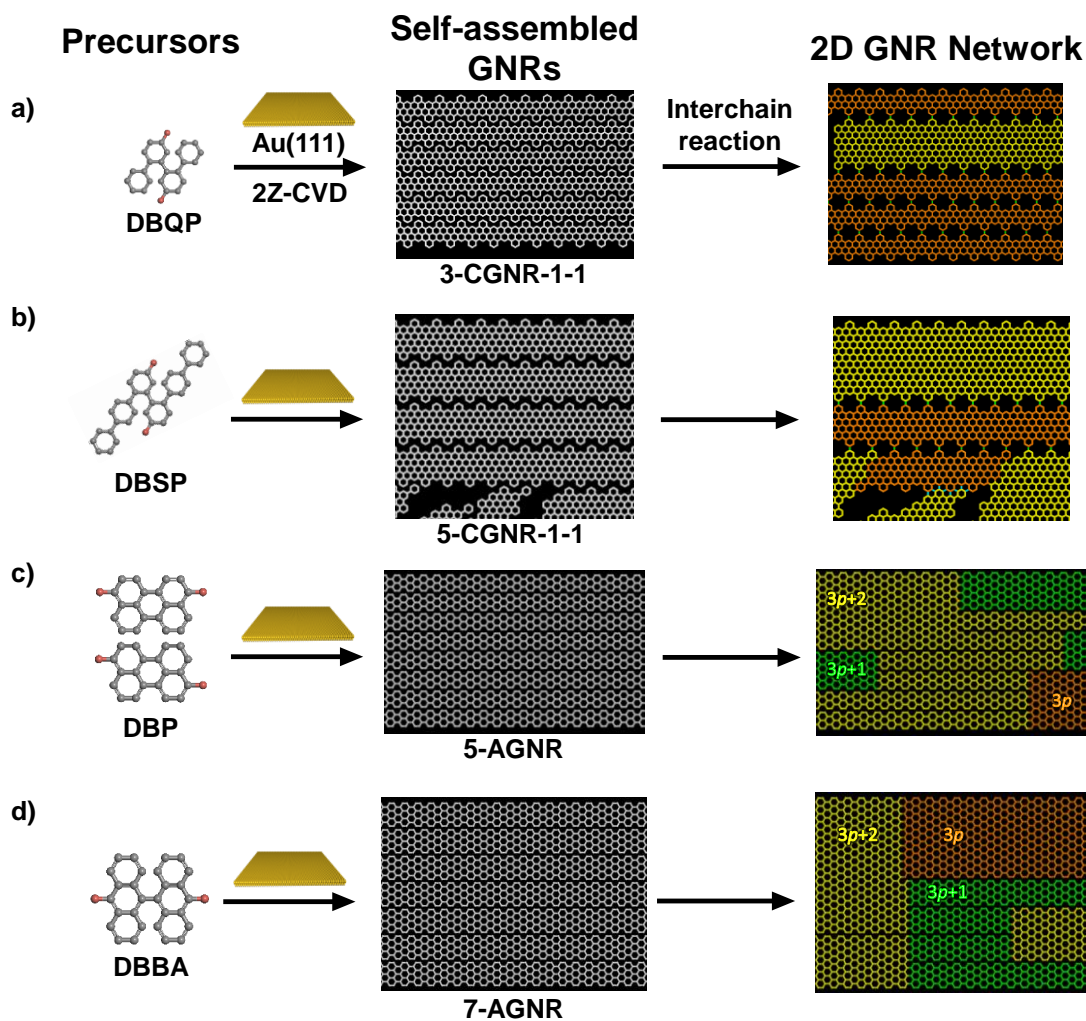


**Figure 4-1.** a-d) Proposed schematic representation of the fabrication process of a 2D graphene nanoribbon network (GNN) produced from 3-CGNR-1-1s, 5-CGNR-1-1s, 5-AGNRs, and 7-AGNRs, respectively. GNNs are formed by interchain reactions between 1D self-assembled graphene nanoribbons (GNRs), which are produced by two-zone chemical vapor deposition (2Z-CVD) of the precursor. In the right panels of (c) and (d), categories ( $3p$ ,  $3p+1$ , and  $3p+2$ , where  $p$  denotes an integer) of the AGNR width in the GNR components are indicated.

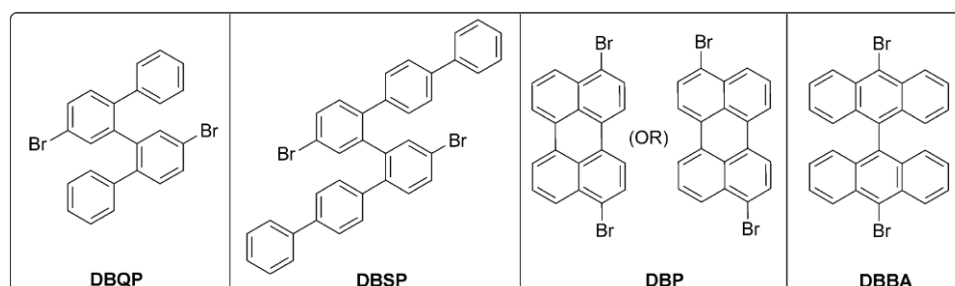


**Figure 4-2.** Structure of precursors DBQP, DBSP, DBP and DBBA.

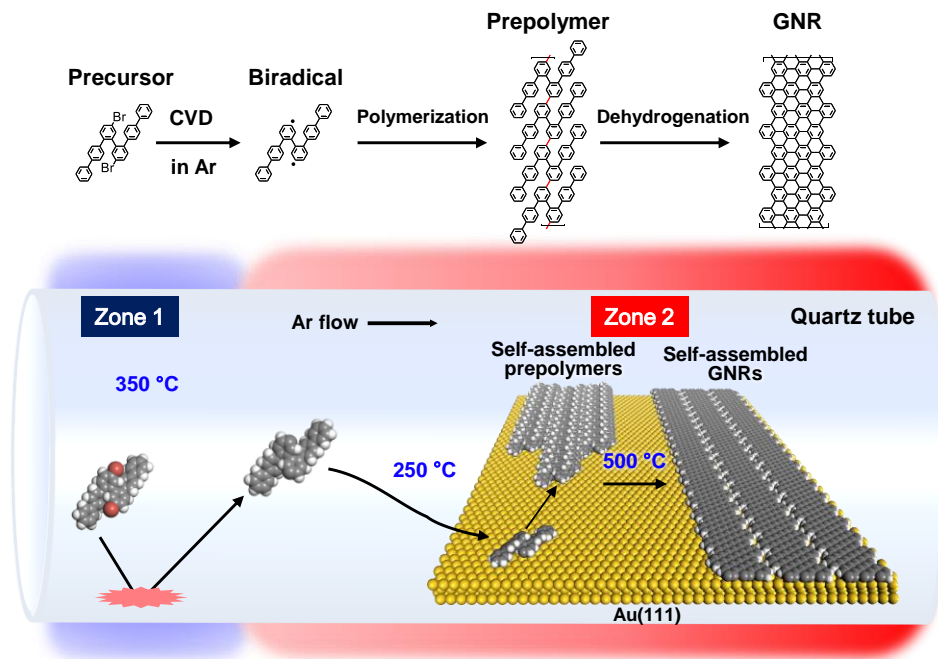


**Figure 4-3.** Schematic representation of the growth of self-assembled GNRs from the precursor DBSP by 2Z-CVD.

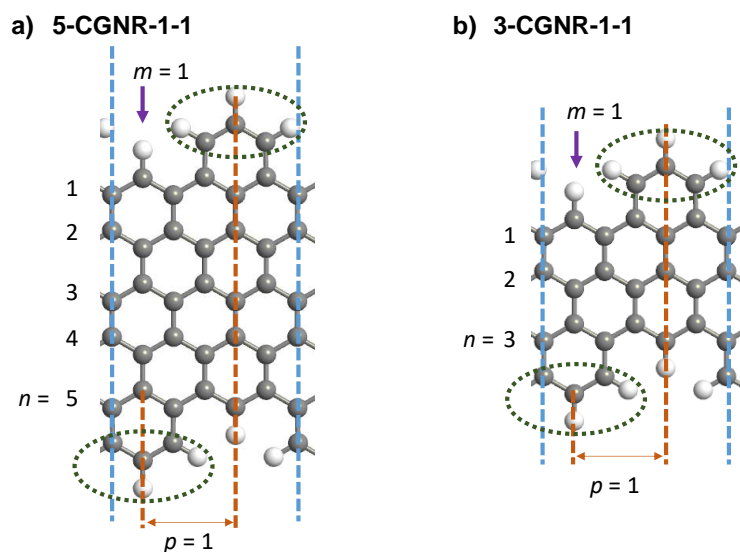


**Figure 4-4.** Nomenclature of cove-edged GNR as  $n$ -CGNR- $m$ - $p$ , following ref 31.<sup>31</sup> a) 5-CGNR-1-1 and b) 3-CGNR-1-1. The blue dashed lines represent the periodicity of the ribbons. Integers,  $n$ ,  $m$ , and  $p$  denote the width of the ribbon, the number of hydrogen atoms along the edge, excluding the hydrogen atoms in the additional phenyl rings on two sides of the ribbon which are indicated by green dashed circles, and the relative position of the two additional phenyl rings, respectively.

The material grown by 2Z-CVD at 250 °C on Au(111) using 40 µg of precursor DBSP was subsequently annealed at 500 °C in zone 2 and examined by scanning tunneling microscopy (STM) at room temperature under Ar atmosphere. Densely packed self-assembly of 5-CGNR-1-1s (Figure 4-4) is observed in the STM images (Figure 4-5a). Remarkably, upon elevating the annealing temperature up to 600 °C, the STM images show fully interconnected 2D network structure confirms the efficient transformation GNR chains into 2D GNNs (Figure 4-5b). Further analysis of the STM images revealed three kinds of interconnection modes (Figure 4-6, Table 4-1), namely a fusion reaction of parallelly aligned chains to form wider GNRs (Figure 4-6 f),<sup>32,33</sup> orthogonally aligned chains to form terminal edge junctions (Figure 4-6g),<sup>34,35</sup> and C–C bond interchain coupling reactions lead to entirely new ladder type 2D-GNNs (Figure 4-6h). Due to this interchain coupling between the cove-edged 3- and 5-CGNR-1-1s, periodic holes are generated across the 2D-GNNs (Figure 4-4).

The ladder structure was clearly seen in the 2D-GNNs generated by 3-CGNR-1-1s, which synthesized using the precursor DBQP, as shown in Figure 4-7 and Figure 4-8. The structural analysis of the ladder-GNRs shown in the STM images was confirmed to match the model (Figure 4-7). The ladder type 2D-GNNs formation mechanism involving the interchain-coupling of shifting chains is depicted in Figure 4-7g. Fusion reactions between GNRs produced by UHV deposition have been reported to occur stochastically where GNR chains are in close proximity to each other due to the nonparallel alignment of the chains.<sup>32,33</sup> Our densely packed, parallelly aligned self-assembled GNRs are able to realize a remarkably high yield of interchain reactions. In addition, the armchair-edged (5-AGNR and 7-AGNR) GNRs were synthesized using the precursor of isomeric mixture of DBP and DBBA, respectively. Upon elevating the annealing temperature to 600 °C, they are also produced 2D-GNNs through the high-yield interchain reactions (Figure 4-9 and Figures 4-5d–i for 5-AGNR and 7-AGNR, respectively). The width of the fused 7-AGNRs in the GNN was found to be as wide as 7.34 nm, corresponding to the fusion of eight parallel GNR chains (Figure 4-5g–i). The observed widths are the widest reported so far for bottom-up fabricated GNRs.<sup>32</sup>



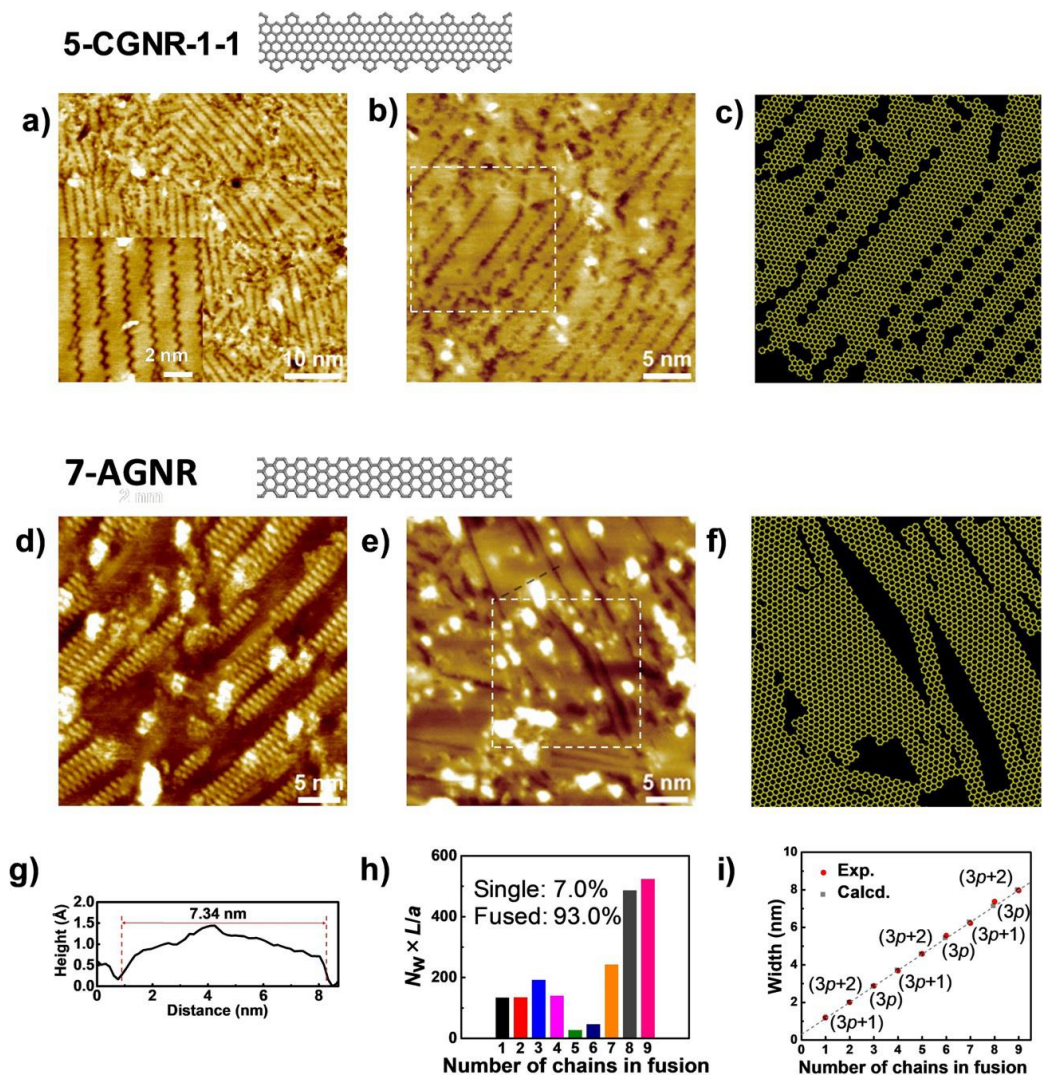


**Figure 4-5.** a,b,d,e) STM images of 5-CGNR-1-1 (a) and 7-AGNR (d). The samples were produced by 2Z-CVD at 500 °C before (a and d) and after (b and e) annealing at 600 °C. The inset in (a) shows a magnified STM image. c,f) Proposed chemical structures of the GNR corresponding to the white dotted area in (b and e, respectively). g) Cross-sectional analysis of the black dashed line in (e). h) Histogram of the number of chains in fused 7-AGNRs in the STM image (e), with the percentage of single and fused chains shown. The ordinate shows a two-dimensional analogue of the weight-average molecular weight,  $N_w \times L/a$ , where  $N_w$  refers to the counted number of chains in fusion having length  $L$  (nm) and  $a$  corresponds to the monomer-unit length. i) Experimental and calculated widths of fused 7-AGNRs as a function of the number of chains. The number of carbons in the width of the GNR is categorized into  $3p$ ,  $3p+1$ , and  $3p+2$ , where  $p$  denotes an integer. The three types of categories are indicated in parentheses at each point.



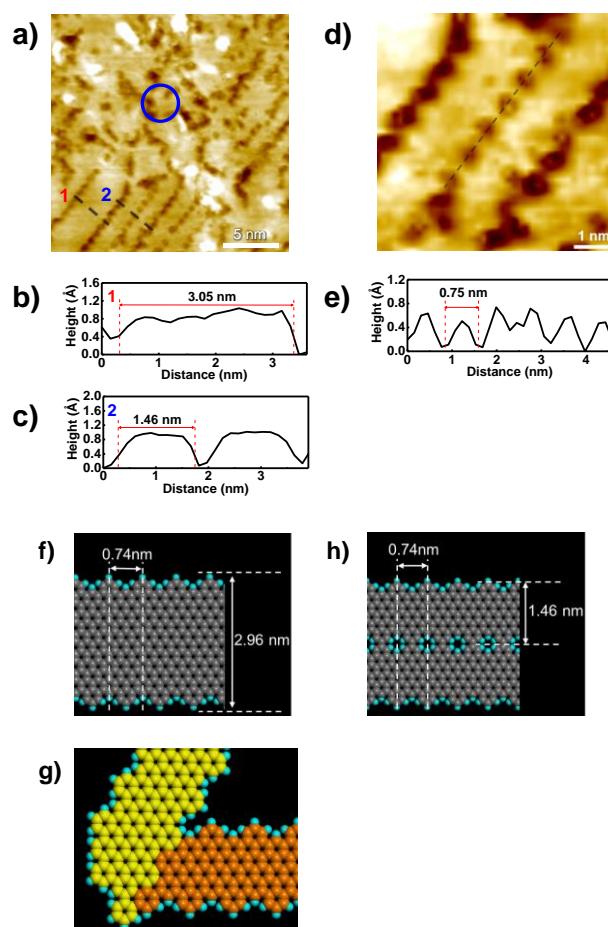


**Figure 4-6.** a) STM image of GNN produced from 5-CGNR-1-1s by annealing at 600 °C. b,c) Cross-sectional analysis of the lines in (a). d) Magnified STM image of ladder-GNR. e) Cross-sectional analysis of line in (d). f,g,h) Models of parallelly fused, orthogonally fused, and ladder-type GNRs. The model of the orthogonally fused GNR (g) was inferred from the STM image (a) from the location marked by a blue circle.

The electronic structure of armchair-edged GNRs has been theoretically predicted to depend on the number of carbons across the width of the GNR ( $N$ ), categorized into  $N = 3p$ ,  $3p+1$ , and  $3p+2$ , where  $p$  denotes an integer.<sup>36</sup> According to first-principle theory using a tight-binding approximation, armchair-edged GNRs with a width of  $3p+2$  are predicted to have metallic-like characteristics, whereas those with widths of  $3p$  and  $3p+1$  have semiconducting characteristics.<sup>36</sup> The band gaps of 2D-GNNs at defined points in the STM images were measured by scanning tunneling spectroscopy (Figure 4-10), and based on a rough estimation, the band gaps of fused

GNRs were observed to decrease compared with their single chain counterparts.<sup>37,38</sup>

**Table 4-1.** Interchain reaction modes of GNRs.

	5-CGNR-1-1	5-AGNR	7-AGNR
<b>Parallel fusion</b>			
<b>Orthogonal fusion</b>			
<b>Ladder</b>			
		Unstable four-membered rings	Unstable four-membered rings

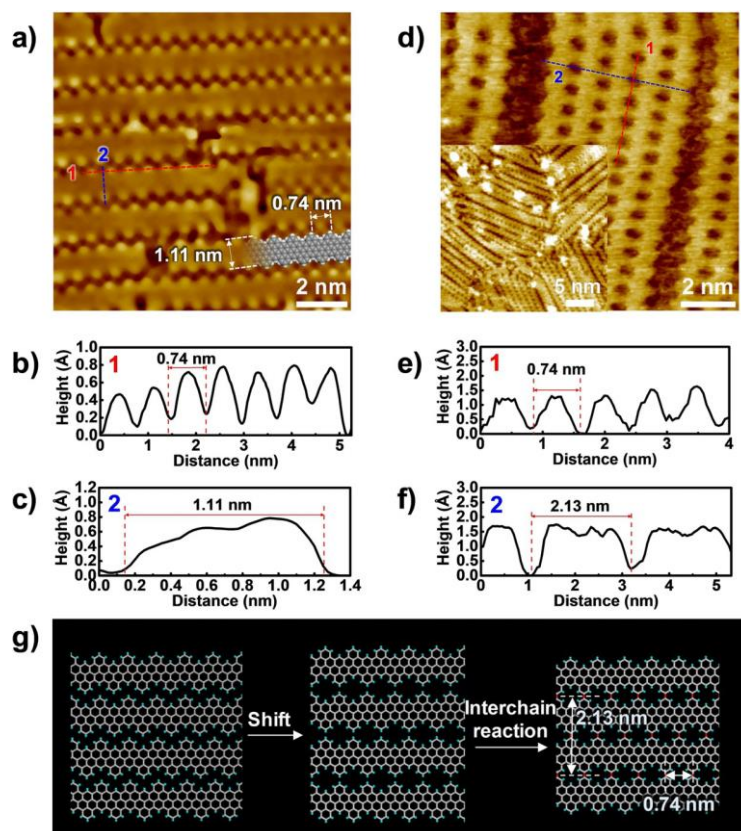


**Figure 4-7.** a,d) STM images of 3-CGNR-1-1 produced by 2Z-CVD at 500 °C before (a) and after (d) annealing at 600 °C. Inset of (d) shows a larger area of 35×35 nm<sup>2</sup>. b,c) Cross-sectional analysis of the dotted lines in (a). e,f) Cross-sectional analysis of the dotted lines in (d). g) Schematic representation of the ladder-GNR formation mechanism.

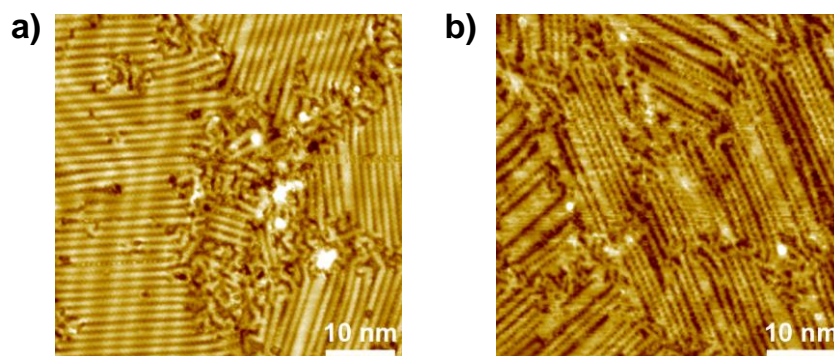


**Figure 4-8.** Large-scale STM images ( $50 \times 50 \text{ nm}^2$ ) of 3-CGNR-1-1 before (a) and after (b) annealing from  $500 \text{ }^\circ\text{C}$  to  $600 \text{ }^\circ\text{C}$ .

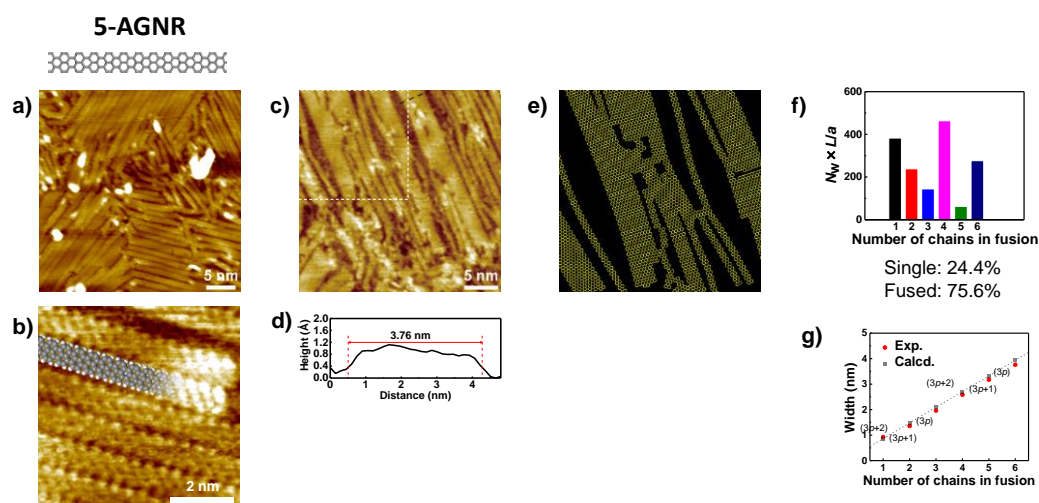


**Figure 4-9.** a) STM image of 5-AGNR produced by 2Z-CVD at  $500 \text{ }^\circ\text{C}$ . b) A magnified STM image of 5-AGNR with an overlaid structural model. c) STM image of GNNs fabricated from 5-AGNR by annealing at  $600 \text{ }^\circ\text{C}$ . d) Cross-sectional analysis of the black dashed line in (c). e) Proposed chemical structures of GNNs corresponding to the white dashed area in (c). f) Histogram of the number of chains in fused-GNRs in the STM image (c), with the areal percentage of single and fused chains shown. The ordinate shows a two-dimensional analogue of the weight-average molecular weight,  $N_w \times L/a$ , where  $N_w$  refers to the counted number of chains in fusion having length  $L$  (nm) and  $a$  corresponds to the monomer-unit length. g) Experimental and calculated widths of fused-GNRs as a function of the number of chains. The number of carbons in the width of the GNR is categorized into  $3p$ ,  $3p+1$ , and  $3p+2$ , where  $p$  denotes an integer. The three types of categories are indicated in parentheses at each point.

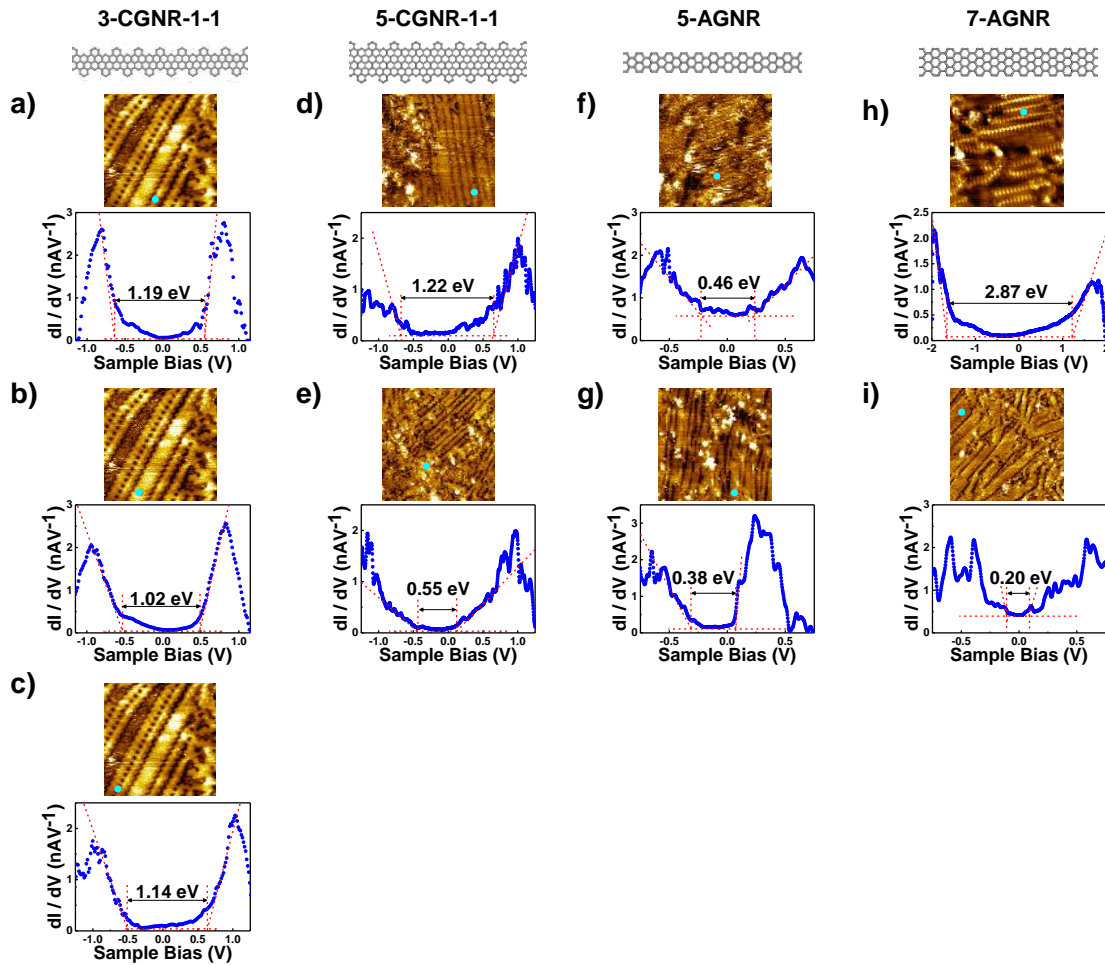


**Figure 4-10.** a,d,f,h)  $dI/dV$  curves of 3-CGNR-1-1, 5-CGNR-1-1, 5-AGNR, and 7-AGNR, respectively. b,e,g,i)  $dI/dV$  curves of parallelly fused GNRs produced from 3-CGNR-1-1, 5-CGNR-1-1, 5-AGNR, and 7-AGNR, respectively. c)  $dI/dV$  curve of ladder-GNRs produced from 3-CGNR-1-1. The experimental bandgaps are shown in the figures. The STM images show the position of the STS measurements marked by a light blue dot.

#### 4-2-2. Thermoelectric properties of fabricated 1D GNR and 2D GNN

The annealing-temperature dependence of the in-plane electrical conductivity ( $\sigma$ ) of five-layer GNR films were investigated, as shown in Figure 4-11. For this purpose, GNRs grown on Au(111) were transferred onto a quartz substrate using a previously reported gold-etching solution process (Figure 4-12).<sup>34,39</sup>

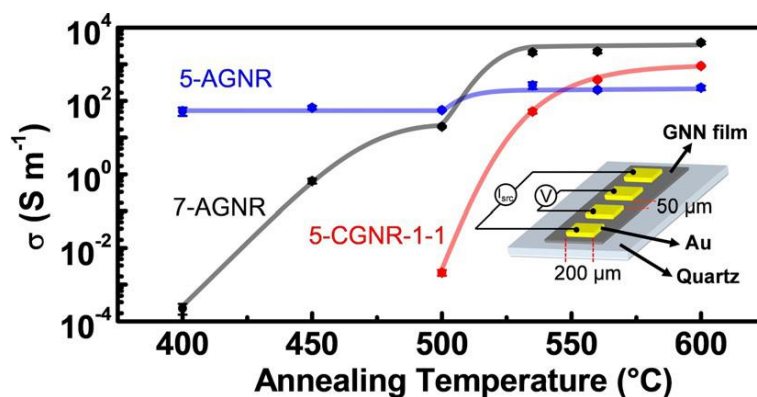


**Figure 4-11.** In-plane electrical conductivity ( $\sigma$ ) as a function of annealing temperature of five-layer GNR films. The samples were prepared by transferring five layers of GNR films from Au(111) onto a hydrophobic quartz substrate using a gold-etching solution process.

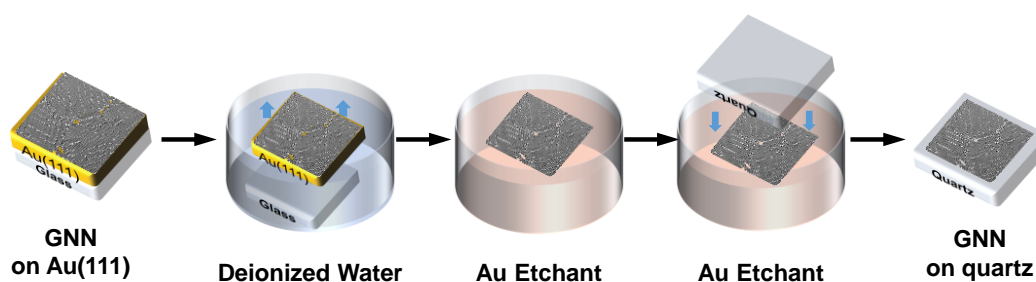


**Figure 4-12.** Schematic representation of the transfer of GNN fabricated on Au(111) onto a quartz substrate.

5-CGNR-1-1, 5-AGNR, and 7-AGNR have generated at the temperature of 500, 350, and 400 °C, respectively. The electrical conductivity of 5-AGNR, which is predicted to be metallic-like, was  $50 \text{ S m}^{-1}$ , whereas those of 7-AGNR and 5-CGNR-1-1 are semiconducting, were  $10^{-4}$  and  $10^{-3} \text{ S m}^{-1}$ , respectively (Figure 4-11). The electrical conductivities of these 1D GNRs are in good agreement with the theoretically predicted tendencies.<sup>36</sup> Electrical conductivity of 5-CGNR-1-1 and 7-AGNR were significantly enhanced by five to seven orders of magnitude, respectively, reaching 900 and 3900  $\text{S m}^{-1}$ , upon elevating the annealing to 600 °C (Figure 4-11). And metallic-like 5-AGNRs also showed a fourfold enhancement, reaching  $230 \text{ S m}^{-1}$  (Figure 4-11). This kind of electrical conductivity enhancement upon raising the annealing temperature clearly reveals that there is an extension in the carrier path, which can be achieved by the transformation of 1D GNRs to 2D GNNs structure through the fusion and interconnections.



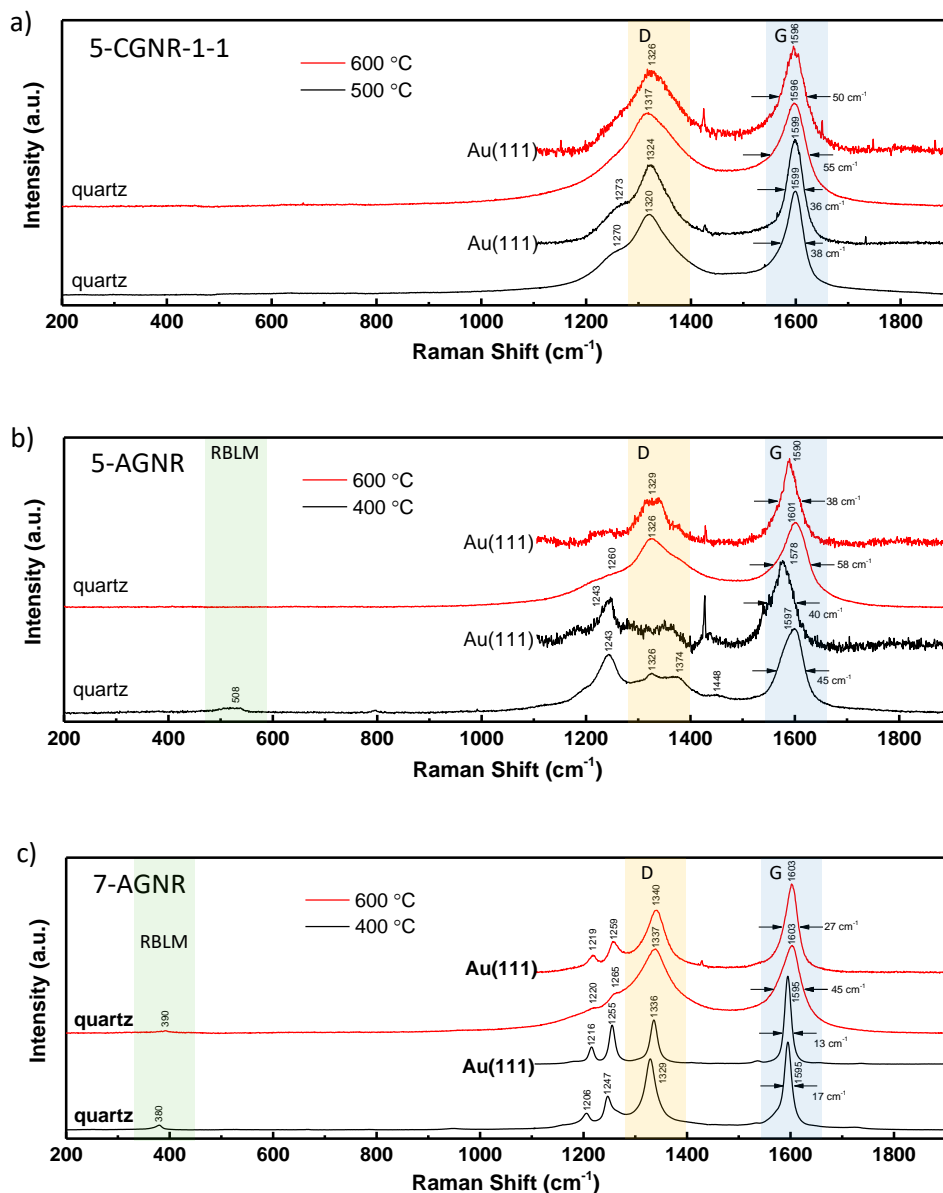


**Figure 4-13.** Raman spectra of GNNs as synthesized on Au(111) and as transferred onto quartz (five layers) and UHV annealed. a-c) Annealing temperature dependence on Raman spectra of 5-CGNR-1-1, 5-AGNR, and 7-AGNR, respectively. The position of each peak and the full width at half maximum of the G band peaks are shown as calculated from a Lorentzian curve fit. The peaks are assigned to G, D, and radial breathing-like mode (RBLM).

The Raman spectra of the GNNs also support the occurrence of such transitions, as spectral changes showing a broadening of G and D peaks and weakening of single chain RBLM peak were observed following the annealing (Figure 4-13). The macrogap-scale field-effect-transistor properties of 2D-GNNs were also measured (Figure 4-14) and found that GNNs showed higher

mobilities and lower on/off ratios compared with those of GNRs.

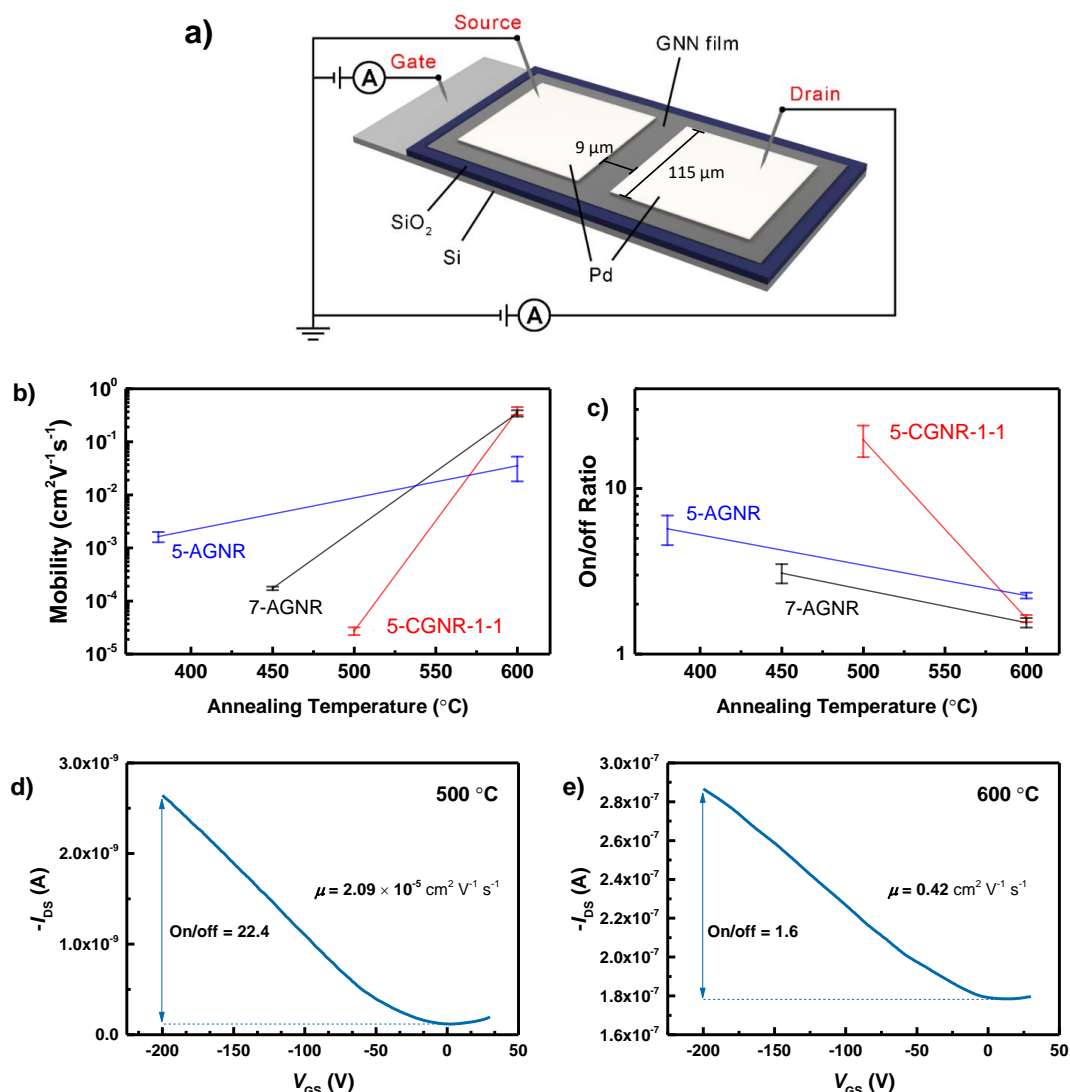


**Figure 4-14.** Annealing temperature dependence on the macrogap-scale FET properties of a GNR monolayer film. a) Schematic layout of the FET device. b,c) The annealing temperature dependence on mobility and on/off ratio of each GNR. d,e) Transport characteristics of 5-CGNR-1-1 films at different annealing temperatures. The drain-source voltage was set to -5 V and -10 mV for (d) and (e), respectively.

To improve the TE properties of GNRs system, different strategies have theoretically been employed; mainly by reducing the thermal conductance while maintaining high thermopower values. One of the best ways to reduce the thermal conductivity of GNRs is by introducing the nanopores in them.<sup>26,28,29,40</sup> The GNR with optimal value of different pore dimensions shows the ZT value 6 times higher than the GNR without pores. Importantly, chevron-type nitrogenated

holey (NH) 2D GNRs shows the ZT value up to 1.5 due to the combination of lower phonon thermal conductance and slightly increased the Seebeck coefficient.<sup>30</sup> To this extend, we are trying to validate these predictions by experimentally; Here we analyze the TE properties of cove-type holey 2D GNNs experimentally using the model theory for of GNR nanostructures.<sup>41</sup> The cross-plane thermal conductivity of the GNNs was investigated using the  $2\omega$  method based on a thermo-reflectance measurement (Figure 4-15).<sup>41</sup>

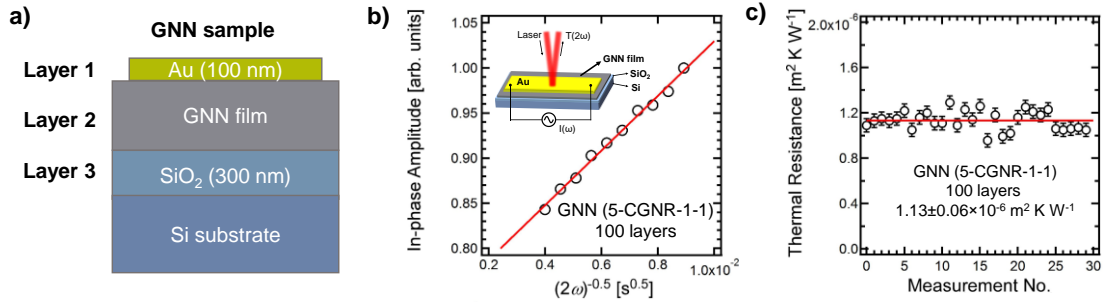


**Figure 4-15.** Cross-plane thermal resistance measurement of 89 nm-thick GNN film produced from 5-CGNN-1-1s by the  $2\omega$  method. a) Schematic illustration of the three-layered model of the GNN sample. b) Thermo-reflectance (TR) signal obtained by a single measurement. In-phase amplitude of TR signal is plotted versus each  $(2\omega)^{-0.5}$  (black open circle) with a linear fit (red line). c) Thermal resistances between Au film and Si substrate, which were measured 30 times. Averaged thermal resistance (red line) was evaluated to be  $R = 1.13 \pm 0.06 \times 10^{-6} \text{ [m}^2 \text{ K W}^{-1}\text{]}$ .

To investigate the 2D-GNNs formed by 5-CGNN-1-1 films with different thicknesses of up to 89 nm (Figure 4-16) were prepared by repetitive deposition onto a silicon substrate. A plot of the thermal resistance of each sample measured by the  $2\omega$  method is shown in Figure 4-17a. The slope of the thermal resistance plot reveals the thermal conductivity in the cross-plane to be  $0.11 \text{ W m}^{-1} \text{ K}^{-1}$ . This value belongs to one of the lowest thermal conductivities reported so far in carbon-based materials as well as inorganic semiconductors (Figure 4-17b, Table 4-2).<sup>31</sup> Because the thermal conductivity was measured in the cross-plane direction, the electrical conductance of 2D-GNNs was also examined in the cross-plane direction and found to be  $188 \text{ S m}^{-1}$  (Figure 4-17b and Figure 4-18). Scanning electron microscopy images showed that the GNN film consists of small flakes (Figure 4-17a, inset; Figure 4-17c) and AFM images also revealed similar flake structures (Figure 4-17d). Such a disordered structure can be thought to further enhance the



reduction of thermal conductivity of the GNN.

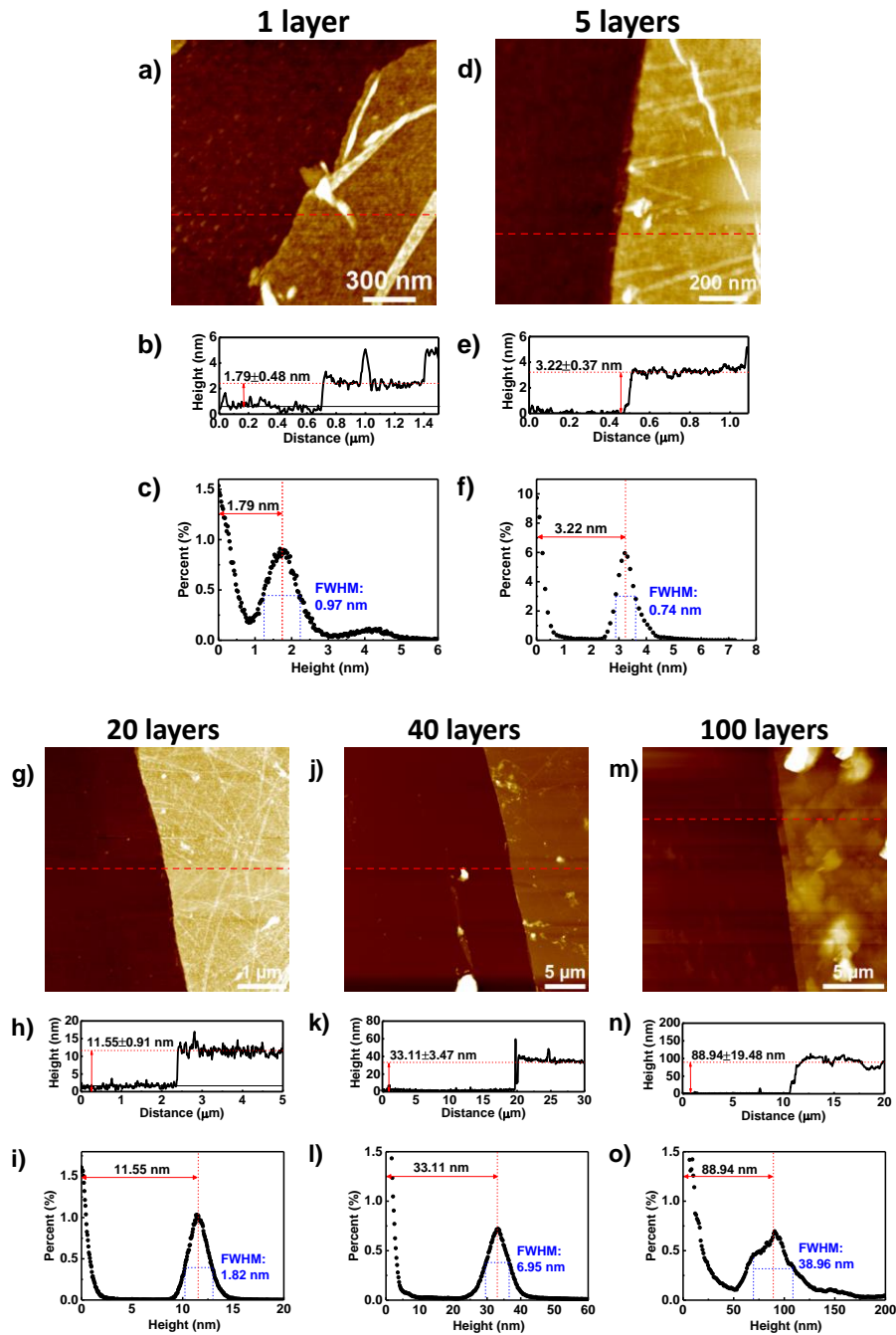


**Figure 4-16.** AFM-height analysis of GNN films from 5-CGNR-1-1s with various thicknesses. a,d,g,j,m) AFM images of GNNs from 5-CGNR-1-1 on  $\text{SiO}_2/\text{Si}$  substrate with a deposition of 1, 5, 20, 40, and 100 layers, respectively. b,e,h,k,n) Height profiles from the AFM images (a), (d), (g), (j) and (m), respectively. c,f,i,l,o) Height histograms from the AFM images (a), (d), (g), (j) and (m), respectively. These data were used for the GNN thickness for the electrical and thermal conductivity measurements.

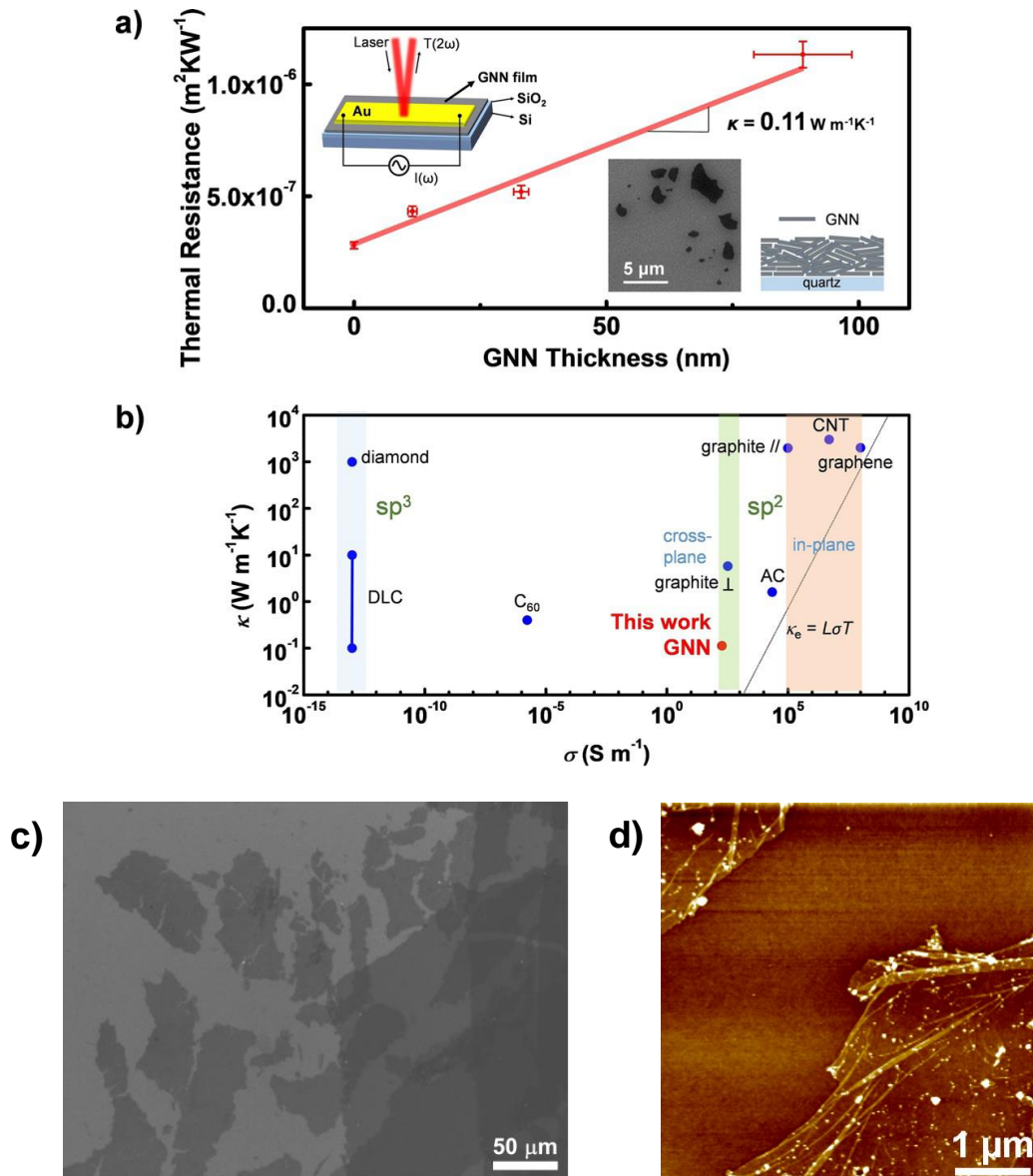


**Figure 4-17.** a) Cross-plane thermal conductivity of the GNN based on 5-CGNR-1-1s measured by the thermo-reflectance  $2\omega$  method. The bottom right insets show a scanning electron microscope image of a low-density GNN monolayer and the proposed disordered film structure. b) Thermal conductivity ( $\kappa$ ) of carbon allotropes as a function of electric conductivity ( $\sigma$ ). The dotted line indicates the carrier-induced thermal conductivity ( $\kappa_e$ ) derived from the Wiedeman-Flanz law ( $\kappa_e = L\sigma T$ ), where  $L$  is the Lorenz factor of  $2.4 \times 10^{-8} \text{ J}^2 \text{ K}^{-2} \text{ C}^{-2}$  for free electrons and  $T$  is the absolute temperature of 300 K. c) Scanning electron microscope (SEM) image of the edge of a five-layered GNN film from 5-CGNR-1-1s transferred onto a SiO<sub>2</sub>/Si substrate. d) Atomic force microscope (AFM) image of the edge of a monolayered GNN film produced from 5-CGNR-1-1s transferred onto a SiO<sub>2</sub>/Si substrate.

**Table 4-2.** Thermal conductivities of carbon-based materials as a function of electrical conductivity. These data were plotted in Figure 4-17b.

Compound	Electrical conductivity $\sigma$ (S m <sup>-1</sup> )	Thermal conductivity $\kappa$ (W m <sup>-1</sup> K <sup>-1</sup> )
<b>This work</b>		
<b>Graphene Nanoribbon Network (5-CGNR-1-1)</b>	900 (in plane) 188 (cross plane)	0.11
Amorphous carbon (AC)	$2.5 \times 10^4$ [Ref. 42] <sup>42</sup>	1.59 [Ref. 43] <sup>43</sup>
Graphite (cross plane)	330 [Ref. 43] <sup>43</sup>	5.73 [Ref. 43] <sup>43</sup>
[60]Fullerene C <sub>60</sub>	$1.7 \times 10^{-6}$ [Ref. 44] <sup>44</sup>	0.4 [Ref. 45] <sup>45</sup>
Graphite (in plane)	$1 \times 10^6$ [Ref. 43] <sup>43</sup>	1960 [Ref. 43] <sup>43</sup>
Graphene	$5 \times 10^6$ [Ref. 43] <sup>43</sup>	2000 [Ref. 35] <sup>31</sup>
Carbon nanotube	$1 \times 10^{-13}$ [Ref. 43] <sup>43</sup>	3000–3500 [Ref. 35] <sup>31</sup>
Diamond	$1 \times 10^{-13}$ [Ref. 43] <sup>43</sup>	2000 [Ref. 35] <sup>31</sup>
Diamond-like carbon	$1 \times 10^{-13}$	0.1-10 [Ref. 35] <sup>31</sup>

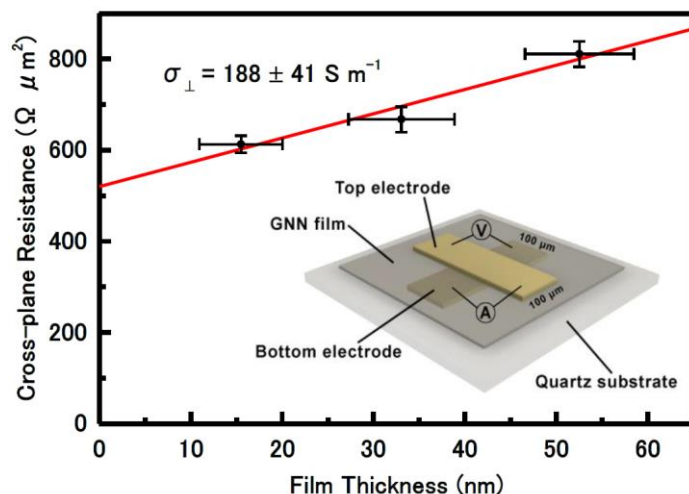


**Figure 4-18.** Cross-plane resistance ( $R_{CP}$ ) of GNNs produced from 5-CGNR-1-1 annealed at 600 °C as a function of the GNN film thickness. The resistance ( $R$ ) has been normalized to include the area ( $A$ ) of the electrode ( $R_{CP} = R \times A$ ) so that the inverse of the slope of the linear fit (red line) determines the cross-plane conductivity. The intercept represents the contact resistance between the octadecanethiol-treated electrodes and the GNN film. The inset shows the device configuration.

### 4-3. Conclusions

In this study, we have successfully fabricated cove- and armchair-type 2D-GNNs on the surface of Au(111) through the thermally induced interchain reactions of densely packed self-assembled GNRs (5-CGNR-1-1 and 7-AGNR), using the new concept of transforming 1D chains into a 2D network. The 5-CGNR-1-1 and 7-AGNR on Au(111) were produced by 2Z-CVD using the precursor of DBQP and DBSP, respectively. The STM images clearly confirm the generation of 2D-GNNs on the surface of Au(111). The structure of 2D-GNNs consist of hybridized junctions of GNRs with various widths, showing both metallic-like and semiconducting characteristics. Particularly, around fourfold increase in the electrical conductivity of 2D-GNNs when compared to the corresponding GNRs, also confirms the formation of a 2D network structure. The thermal conductivity of 2D-GNNs generated from 5-CGNR-1-1 shows a value of  $0.11 \text{ W m}^{-1} \text{ K}^{-1}$ , which is one of the lowest values among carbon-based materials as well as inorganic semiconductor materials, while maintaining the electrical conductivity of  $188 \text{ S m}^{-1}$ .

These findings will open new perspectives in the field of research on the utilization of GNRs for TE applications.

#### 4-4. References

1. G. J. Hedley, A. Ruseckas, and I. D. Samuel, *Chem. Rev.*, **2017**, 117 (2), 796-837.
2. K. A. Mazzio and C. K. Luscombe, *Chem. Soc. Rev.*, **2014**, 44 (1), 78-90.
3. D. F. Perepichka and F. Rosei, *Science*, **2009**, 323 (5911), 216-217.
4. P. Payamyar, B. T. King, H. C. Öttinger, and A. D. Schlüter, *Chem. Commun.*, **2016**, 52 (1), 18-34.
5. A. D. Schlüter, P. Payamyar, and H. C. Öttinger, *Macromol. Rapid Commun.*, **2016**, 37 (20), 1638-1650.
6. J. Mahmood, E. K. Lee, M. Jung, D. Shin, I.-Y. Jeon, S.-M. Jung, H.-J. Choi, J.-M. Seo, S.-Y. Bae, and S.-D. Sohn, *Nat. Commun.*, **2015**, 6, 6486.
7. A. Miura, S. De Feyter, M. M. Abdel-Mottaleb, A. Gesquiere, P. C. Grim, G. Moessner, M. Sieffert, M. Klapper, K. Müllen, and F. C. De Schryver, *Langmuir*, **2003**, 19 (16), 6474-6482.
8. H. Sakaguchi, H. Matsumura, and H. Gong, *Nat. Mater.*, **2004**, 3 (8), 551-557.
9. L. Grill, M. Dyer, L. Lafferentz, M. Persson, M. V. Peters, and S. Hecht, *Nat. Nanotechnol.*, **2007**, 2 (11), 687-691.
10. C. Moreno, M. Vilas-Varela, B. Kretz, A. Garcia-Lekue, M. V. Costache, M. Paradinas, M. Panighel, G. Ceballos, S. O. Valenzuela, and D. Peñã, *Science*, **2018**, 360 (6385), 199-203.
11. A. Basagni, F. Sedona, C. A. Pignedoli, M. Cattelan, L. Nicolas, M. Casarin, and M. Sambì, *J. Am. Chem. Soc.*, **2015**, 137 (5), 1802-1808.
12. J. Cai, P. Ruffieux, R. Jaafar, M. Bieri, T. Braun, S. Blankenburg, M. Muoth, A. P. Seitsonen, M. Saleh, and X. Feng, *Nature*, **2010**, 466 (7305), 470-473.
13. X. Zheng, C. Liu, Y. Yan, and Q. Wang, *Renew. Sust. Energ. Rev.*, **2014**, 32, 486-503.
14. J. Karni, *Nat. Mater.*, **2011**, 10 (7), 481.
15. G. S. Nolas, J. Sharp, and J. Goldsmid, *Thermoelectrics: basic principles and new materials developments*. Vol. 45. 2013, Springer Science & Business Media.
16. Y. M. Zuev, W. Chang, and P. Kim, *Phys. Rev. Lett.*, **2009**, 102 (9), 096807.

17. J. G. Checkelsky and N. P. Ong, *Phys. Rev. B*, **2009**, 80 (8), 081413.
18. P. Wei, W. Bao, Y. Pu, C. N. Lau, and J. Shi, *Phys. Rev. Lett.*, **2009**, 102 (16), 166808.
19. Y. Chen, T. Jayasekera, A. Calzolari, K. Kim, and M. B. Nardelli, *J. Phys.: Condens. Matter*, **2010**, 22 (37), 372202.
20. M.-H. Bae, Z. Li, Z. Aksamija, P. N. Martin, F. Xiong, Z.-Y. Ong, I. Knezevic, and E. Pop, *Nat. Commun.*, **2013**, 4 (1), 1-7.
21. Y. Ouyang and J. Guo, *Appl. Phys. Lett.*, **2009**, 94 (26), 263107.
22. T. Gunst, T. Markussen, A.-P. Jauho, and M. Brandbyge, *Phys. Rev. B*, **2011**, 84 (15), 155449.
23. H. Sevinçli and G. Cuniberti, *Phys. Rev. B*, **2010**, 81 (11), 113401.
24. J. Hu, S. Schiffli, A. Vallabhaneni, X. Ruan, and Y. P. Chen, *Appl. Phys. Lett.*, **2010**, 97 (13), 133107.
25. N. Wei, L. Xu, H.-Q. Wang, and J.-C. Zheng, *Nanotechnology*, **2011**, 22 (10), 105705.
26. J. Haskins, A. Kınacı, C. Sevik, H. Sevinçli, G. Cuniberti, and T. Çağın, *ACS Nano*, **2011**, 5 (5), 3779-3787.
27. M. Xing, B. Chen, J. Feng, W. Xu, Y. Bai, Y. Zhou, C. Dong, H. Zhong, J. Zhang, and Y. Yin, *Chem*, **2019**, 5 (8), 2195-2214.
28. P.-H. Chang and B. K. Nikolić, *Phys. Rev. B*, **2012**, 86 (4), 041406.
29. M. S. Hossain, F. Al-Dirini, F. M. Hossain, and E. Skafidas, *Sci. Rep.*, **2015**, 5, 11297.
30. W. Cao, H. Xiao, T. Ouyang, and J. Zhong, *J. Appl. Phys.*, **2017**, 122 (17), 174302.
31. A. A. Balandin, *Nat. Mater.*, **2011**, 10 (8), 569-581.
32. H. Huang, D. Wei, J. Sun, S. L. Wong, Y. P. Feng, A. C. Neto, and A. T. S. Wee, *Sci. Rep.*, **2012**, 2, 983.
33. S. Kawai, S. Saito, S. Osumi, S. Yamaguchi, A. S. Foster, P. Spijker, and E. Meyer, *Nat. Commun.*, **2015**, 6, 1-6.
34. P. Han, K. Akagi, F. Federici Canova, R. Shimizu, H. Oguchi, S. Shiraki, P. S. Weiss, N. Asao, and T. Hitosugi, *ACS Nano*, **2015**, 9 (12), 12035-12044.
35. T. Dienel, S. Kawai, H. Söde, X. Feng, K. Müllen, P. Ruffieux, R. Fasel, and O. Gröning, *Nano Lett.*, **2015**, 15 (8), 5185-5190.
36. Y.-W. Son, M. L. Cohen, and S. G. Louie, *Phys. Rev. Lett.*, **2006**, 97 (21), 216803.
37. A. Kimouche, M. M. Ervasti, R. Drost, S. Halonen, A. Harju, P. M. Joensuu, J. Sainio, and P.

- Liljeroth, *Nat. Commun.*, **2015**, 6, 10177.
38. P. Ruffieux, J. Cai, N. C. Plumb, L. Patthey, D. Prezzi, A. Ferretti, E. Molinari, X. Feng, K. Müllen, and C. A. Pignedoli, *ACS Nano*, **2012**, 6 (8), 6930-6935.
39. H. Sakaguchi, S. Song, T. Kojima, and T. Nakae, *Nat. Chem.*, **2017**, 9 (1), 57-63.
40. P.-H. Chang, M. S. Bahramy, N. Nagaosa, and B. K. Nikolic, *Nano Lett.*, **2014**, 14 (7), 3779-3784.
41. Y. Nakamura, M. Isogawa, T. Ueda, S. Yamasaka, H. Matsui, J. Kikkawa, S. Ikeuchi, T. Oyake, T. Hori, and J. Shiomi, *Nano Energy*, **2015**, 12, 845-851.
42. D. G. Fink, H. W. Beaty, and H. W. Beaty, Standard handbook for electrical engineers. Vol. 10. 1987, McGraw-Hill New York.
43. W. M. Haynes, D. R. Lide, and T. Bruno, CRC handbook of chemistry and physics: a ready-reference book of chemical and physical data, 96th ed., CRC press: Cleveland, Ohio, 2015-2016.
44. C. Wen and J. Li, *Appl. Phys. Lett.*, **1992**, 61, 2162.
45. R. Yu, N. Tea, M. Salamon, D. Lorents, and R. Malhotra, *Phys. Rev. Lett.*, **1992**, 68 (13), 2050.

## Chapter 5

### General Conclusion

Graphene, the one-atom-thick two-dimensional (2D) carbon material, has attracted tremendous interest in both academia and industry due to its outstanding electrical, mechanical, and thermal properties. For electronic applications, the challenging task is to make it as a semiconductor. The bottom-up synthesis of semiconducting one-dimensional (1D) nanometer-wide graphene strips, namely, graphene nanoribbons (GNRs), has attracted much attention owing to its promising electronic, optical, and magnetic properties. GNRs as a representative class of graphene-based materials show attractive semiconducting property. In the last decade, although theoretical predictions showed many intriguing properties of GNRs, for example, band gaps, most efforts were made to the fabrication, mechanisms and electronic structures of GNRs. The applications were rarely investigated. Recently, using GNRs as building blocks to fabricate 2D nanoporous graphene (NPG) was reported. This endows NPG with both semiconducting and nanosieving functionalities. However, the potential applications of this kind of materials remain elusive. Based on the above context, it inspired me to fabricate the 2D graphene-based materials using GNRs as building blocks and characterize their thermal and electrical properties for the application in the energy section.

In this study, the fabrications of 2D GNR networks (GNNs) via two-zone chemical vapour deposition (2Z-CVD) were investigated. The 2Z-CVD setup enables the preparation of densely packed self-assembled GNRs which are the building blocks for 2D GNNs and could be connected by inter-chain dehydrogenation. Various precursors were applied to check the versatility of this protocol and consequently led to different types of 2D GNNs. The as-prepared 2D GNNs films can be transferred to insulating substrates for the characterization of thermal and electrical property. The results of this study were concluded as following:

In chapter 2, the necessary materials and methods in this study were described.

In chapter 3, the products of two-zone chemical vapor deposition on Au(111) from a Z-bar-linkage precursor with quaterphenyl-branches were investigated by scanning tunneling microscopy, Raman spectroscopy, and theoretical calculations. Annealing at 400 °C produced



linear arrays of intramolecular dehydrogenated precursors, and temperatures over 450 °C led to intermolecular dehydrogenation and to the formation of graphene clusters. This reaction pathway contrasts remarkably with the previous results reported for a Z-bar-linkage precursor with terphenyl branches, where homochiral polymerization proceeded and allowed the formation of acene-type graphene nanoribbons. The reason might originate from the conformation of the biradical form of the quaterphenyl-branched precursor, produced by debromination on Au(111) during 250 °C annealing. The quaterphenyl-branched precursor might favor a symmetric conformation with both the radicals pointing toward the Au(111) surface, whereas our previous results showed that the terphenyl-branched precursor might favor asymmetric (chiral) conformations, with one radical pointing toward and the other one away from the Au(111) surface. Steric hindrance of the symmetric conformations of the quaterphenyl-branched precursor is presumed to prohibit polymerization due to the strong affinity of the biradical to Au(111). Such symmetric precursor conformations lead to fused debrominated precursors via intramolecular dehydrogenation, and finally result in the conversion to graphene clusters via on-surface intermolecular fusion.

In chapter 4, by 2Z-CVD, 2D GNNs with different structures were successfully fabricated. Briefly, the fabrication of cove-type GNNs via the interconnection of 1D self-assembled GNRs on the surface of Au(111). The cove-type 2D GNNs were fabricated from the GNR, 5-CGNR-1-1, synthesized using the precursor of DBSP. Annealing of high density self-assembled GNRs on the surface of Au(111) through 2Z-CVD successfully generated a 2D interconnected structure with high yield via the fusion and ladder coupling reactions of GNR chains. In order to validate the lateral fusion reaction, we have also synthesized the GNR, 7-AGNR, using the precursor of DBBA. The GNNs, which consist of hybridized metallic-like and semiconducting GNRs, are a new class of carbon-based materials. Further, we applied the GNNs from 5-CGNR-1-1 for thermoelectric (TE) applications and found a very low cross-plane thermal conductivity of  $0.11 \text{ W m}^{-1} \text{ K}^{-1}$ , which is one of the lowest value among the carbon-based materials as well as inorganic semiconductors, while maintaining the cross-plane electrical conductivity of  $188 \text{ S m}^{-1}$ .

Fully  $\pi$ -conjugated 2D carbon nanostructures attract much attention, since they can provide conducting carbon-based nanostructures with holey structures highly suitable for various electronic applications. This study presented the examples for fabricating fully  $\pi$ -conjugated 2D

structures using GNRs as building blocks. The next step is to produce more well-organised structures in large domain, which is necessary to practically apply in integrated devices. This strategy might be realized by selective bond activation or seeking new building blocks. Afterwards, various novel functional fully  $\pi$ -conjugated 2D carbon-based nanostructures would be expected to be prepared via 2Z-CVD system, which could be applied to applications in energy section.

## List of publications

1. On-surface synthesis of graphene clusters from a Z-bar-linkage precursor with quaterphenyl branches

**Zhen Xu**, Takahiro Kojima, Wanyu Wang, Kabya Kaushik, Alex Saliniemi, Takahiro Nakae, and Hiroshi Sakaguchi

*Materials Chemistry Frontiers*, 2018, 2, 775-779.

(Chapter 3)

2. Bio-inspired Surface Catalysis to Produce Graphene Nanoribbons

Takahiro Kojima, **Zhen Xu**, Hiroshi Sakaguchi

*Journal of Synthetic Organic Chemistry Japan*, 2019, 77(6): 576-583.

3. Bottom-Up on Surface Synthesis of Two-Dimensional Graphene Nanoribbon Networks and Their Thermoelectric Applications

Takahiro Kojima, Takahiro Nakae, **Zhen Xu**, Saravanan Chinnusamy, Kentaro Watanabe, Yoshiaki Nakamura, and Hiroshi Sakaguchi

*Chemistry-An Asian Journal*, 2019, 14(23): 4400-4407.

(Chapter 4)

## Other publications

1. Effects of anions on the underpotential deposition behavior of Cu on polycrystalline Pt

Jiao Liu, **Zhen Xu**, Benfeng Zhu, Xiaoqing Du, Yumeng Yang, Chenxi Yi, and Zhao Zhang

*RSC Advances*, 2018, 8(34): 19103-19115.

2. Ligand-regulated ORR Activity of Au Nanoparticles in Alkaline Medium: the Importance of Surface Coverage of Ligands

Linfang Lu, Shihui Zou, Yuheng Zhou, Juanjuan Liu, Renhong Li, **Zhen Xu**, Liping Xiao, and Jie Fan

*Catalysis Science & Technology*, 2018, 8(3): 746-754.

## List of presentations

1. On-surface synthesis of acene-type graphene nanoribbons by two-zone chemical vapor deposition

**Zhen Xu**, Takahiro Kojima, Takahiro Nakae, Hiroshi Sakaguchi

The 4th Open Symposium on  $\pi$ -System Figuration, **2017.10.19-20**, Tokyo, Japan.

2. On-surface synthesis of nano graphene from a Z-bar-linkage precursor with quaterphenyl branches

Takahiro Kojima, **Zhen Xu**, Hiroshi Sakaguchi

The 29th Symposium on Physical Organic Chemistry, **2018.09.06-08**, Tokyo, Japan.

3. Biomimetic surface reaction toward graphene nanoribbons

Takahiro Kojima, **Zhen Xu**, Hiroshi Sakaguchi

International Congress on Pure & Applied Chemistry Langkawi (ICPAC Langkawi),

**2018.10.30-11.02**, Langkawi, Malaysia.

4. Preparation of interchain-linked 2D Graphene Nanoribbons with Dibenzo[g,p]chrysene by Two-Zone Chemical Vapor Deposition

Pei Zong, **Zhen Xu**, Kabya Kaushik, Shunpei Nobusue, Takahiro Kojima, Hiroshi Sakaguchi

The 99th Annual Meeting of CSJ, **2019.03.16-19**, Kobe, Japan.

5. On-surface Synthesis of Graphene Clusters from a Quaterphenyl-branched Z-bar-linkage Precursor

**Zhen Xu**, Pei Zong, Kabya Kaushik, Takahiro Kojima, Shunpei Nobusue, Hiroshi Sakaguchi

The 99th Annual Meeting of CSJ, **2019.03.16-19**, Kobe, Japan.

6. Graphene Clusters from a Quaterphenyl-branched Z-bar-linkage Precursor via Two-zone Chemical Vapor Deposition

**Zhen Xu**, Shunpei Nobusue, Takahiro Kojima, Hiroshi Sakaguchi

The 7th International Symposium on  $\pi$ -System Figuration, **2019.03.29-30**, Osaka, Japan.

## **Acknowledgement**

To begin with, I deeply appreciate my supervisor Prof. Hiroshi Sakaguchi. He gave me the chance to study and do research in Kyoto University, and the fully support in the research conditions and equipments. Meanwhile, I learned a lot from Prof. Hiroshi Sakaguchi. Firstly, he has profound knowledge in many research fields including physics, chemistry and biology, and pursues the most advanced research in the world. Due to the interdiscipline research, I learned a lot of knowledge in other disciplines other than chemistry. Secondly, he taught me how to start a meaningful research. New concepts and novel ideas should be built before starting a new project. Thirdly, He taught me that researchers should be very strictful when doing scientific work and careful of new results and phenomena. The most important thing is that I developed my logical thinking and consideration when analysing the scientific results. I should consider mechanisms based on the experimental results rather than personal emotions. This period of four years will be a great fortune in my future.

Thanks to Prof. Kazunari Matsuda and Prof. Toshiyuki Nohira for reviewing this thesis.

Special thanks to the Assistant Prof. Takahiro Kojima, Takahiro Nakae and Shunpei Nobusue. Prof. Kojima Takahiro helped me a lot in both research and life. He helped me to get used to the Japanese life and overcome some difficulties. In the meantime, Prof. Kojima Takahiro taught me many things in research, including 2Z-CVD, STM as well as organic synthesis. He always explained my questions patiently whenever I was confusing. Additionally, he always treated students as friends and made me feel very comfortable. Here, I would like to express my heartiest thanks to him.

Also, I would like to give special thanks to my senior Shaotang Song and the laboratory member Saliniemi Alex Oscar. When I first came to this lab, I only know a little bit about organic synthesis. Shaotang Song taught me how to do organic synthesis from scratch and I learned a lot of experience from him. Then, I could do the following research more smoothly. From that moment, I found a new interested direction of research. The laboratory member Saliniemi Alex Oscar

taught me the basis and operation of FET measurements. He prepared the electrochemical testing apparatus and software for us, which helped me a lot during my research.

Moreover, I would like to thank the current and past laboratory members: Guanbo Huang, Kazuki Nakaya, Yota Takihana, Wanyu Wang, Huan Yang, Kabya Kaushik, Pei Zong, Yuki Hyakuda, Shuang Li, Wenfu Wu, Takatsugu Onishi, Patel Karan, Zahin Farhan, Paul Kavin, Lejian Su and Rossoli Kianoosh. Their spiritual and experimental help made me stonger to overcome the difficulties. Thanks to our lab secretary Miss Yuko Itoh for managing the documents and procedures about university affairs and life in Japan.

Thanks to China Scholarship Council (CSC) for the financial support.

Thanks to Prof. Zhao Zhang, Accociate Prof. Yunchun Li, Xueying Wang (my junior high school teacher) and my friend Peng Xu for their strong support in the applying CSC scholarship.

Last but not the least, I would like to thank my parents and other family members, for their continuous support and understanding during my PhD study.